ARTIFACT REDUCTION IN FUNCTIONAL MAGNETIC RESONANCE IMAGING

by

Brian Wowk

A Thesis

Submitted to the Faculty of Graduate Studies

in Partial Fulfillment of the Requirements for the Degree of

DOCTOR OF PHILOSOPHY

Department of Physics

University of Manitoba

Winnipeg, Canada

THE UNIVERSITY OF MANITOBA

FACULTY OF GRADUATE STUDIES

*****

COPYRIGHT PERMISSION PAGE

ARTIFACT REDUCTION IN FUNCTIONAL MAGNETIC RESONANCE IMAGING

by

BRIAN WONK

A Thesis/Practicum submitted to the Faculty of Graduate Studies of The University of Manitoba in partial fulfillment of the requirements of the degree

DOCTOR of PHILOSOPHY

ABSTRACT

Functional magnetic resonance imaging (fMRI) is a relatively new non-invasive technique for monitoring brain activity with great spatial and temporal precision. Blood-oxygen-level-dependent (BOLD) fMRI operates by detecting localized changes in magnetic field homogeneity that accompany changes in blood oxygenation. However, fMRI studies are prone to artifacts caused by blood flow, variations in NMR signal phase, and patient motion.

A new method of MR imaging called partial presaturation (PSAT) was developed that allows fMRI studies to be performed with reduced sensitivity to blood flow. The method is more effective than previous techniques for eliminating blood flow effects.

New techniques called k-space phase correction and k-space orthogonalization were developed to remove artifacts caused by unwanted phase variations and intra-image motion during fMRI studies. The methods are easily implemented in post-processing of fMRI data. A simple Fourier-domain image registration algorithm was also developed to correct for inter-image motion.

The combination of these techniques significantly improves the sensitivity and specificity of human fMRI experiments.

ACKNOWLEDGMENTS

First and foremost, thanks to my wife and daughter (Deb and Camille) for their patience and support during my graduate studies.

Thanks also to my supervisor, John Saunders, and my sponsors, the University of Manitoba, the Manitoba Health Research Council, the Heart and Stroke Foundation of Canada, and the National Research Council of Canada for the opportunity to do this research.

Finally, I thank my colleagues at NRC: Mike McIntyre, Gord Scarth, Ray Somorjai, Murray Alexander, Lizann Bolinger, Lawrence Ryner, Jie Shen, Arleigh Trainor, Norm Davison, Walter Roberson, Rudy Sebastian, and all those IBD staff members who helped me during various times of need.

TABLE OF CONTENTS

LIST OF FIGURES

Chapter 1

INTRODUCTION

1.1 FUNCTIONAL MAGNETIC RESONANCE IMAGING (fMRI)

1.1.1 INTRODUCTION

For more than a century it has been known that blood flow within the brain increases with metabolic demand (1). These localized changes in blood flow and blood volume form the basis of a variety of methods for imaging brain function using exogenous tracers added to blood. These methods include SPECT (2) (using ^{133}Xe tracer), PET (3) ($H_2{}^{15}O$ tracer), and MRI (4) (gadolinium-DTPA tracer). Recently MRI techniques for measuring local blood flow (perfusion) (5-7) and blood volume (8) without exogenous contrast agents have also become available.

Another approach to detecting brain activation with MRI is based on imaging changes in blood oxygenation. A change in the magnetic susceptibility of blood with oxygenation was first noted by Linus Pauling *et al* in 1936 (9). A deoxyhemoglobin molecule contains four paramagnetic Fe^{++} ions. When combined with four oxygen molecules, the resultant oxyhemoglobin molecule has no net paramagnetism, and is slightly diamagnetic (9-11). As a result, the volume magnetic susceptibility of whole blood varies by $\Delta\chi \approx 1 \times 10^{-6}$ (SI units) between the fully oxygenated and deoxygenated states (11-13). There is also a contrary susceptibility variation associated with dissolved paramagnetic O_2, but it is an order of magnitude smaller (11).

The variation of blood magnetic susceptibility with oxygenation is the basis of BOLD (blood oxygen-level dependent) contrast in MRI. A 10% reduction in blood oxygenation will result in approximately a 0.1 x 10^{-6} shift in volume susceptibility, and a ~0.1 ppm shift in the main magnetic field B0, hence Larmor frequency, of water protons in or near blood vessels. The resulting B0 inhomogeneity causes a dephasing of NMR signal that is apparent as a darkening on T2*-weighted gradient echo (GE) images. T2-weighted spin echo (SE) images also show somewhat smaller darkening near deoxygenated vessels due to non-refocussable dephasing of mobile protons moving through the field inhomogeneities. This BOLD darkening of T2 and especially T2*-weighted images near blood vessels was first noted by Ogawa (14-16) and Turner (17). Ogawa suggested that the BOLD effect might be used to image brain activity by observing blood oxygenation decreases in areas of increased oxygen consumption.

The first successful BOLD fMRI experiments were demonstrated in 1992 (5,18-21). Whereas early experiments focused on large, robust activations of the visual cortex during photic stimulation, later studies successfully detected brain activations during motor and even subtle cognitive tasks (22-30). A simple BOLD fMRI experiment is shown in Fig. 1.1

Paradoxically, the activations observed during BOLD fMRI experiments were not the signal decreases predicted by Ogawa. Rather, T2* image intensity, hence blood oxygenation, was found to increase in active brain areas. This is now known to be due to

an over-adjustment of blood flow that occurs when a brain area becomes active (31,32,33). Even though local oxygen consumption increases by only 5% with activation, local blood flow typically increases by 50% or more (5). As a result, venous blood oxygenation downstream from the activation site increases from a resting value of about 60% to an active value of 70%. This increase in oxygenation in venules and veins draining active brain areas is the basis of BOLD fMRI.

Typical gradient echo times (TE) found to maximize contrast-to-noise ratio in BOLD fMRI range from TE = 60 ms for 1.5T to TE = 30 ms for 4 Tesla systems. At these echo times, image intensity changes accompanying activation in cortical matter range up to 5% on conventional 1.5T clinical scanners, and 10% or more on high field 3T and 4T systems. These signal changes can be theoretically modeled by considering cortical matter as a sparse collection of randomly oriented cylinders (venules) that undergo oxygenation and susceptibility changes as described above (34-36). Activation-related signal changes as large as 30% or more are sometimes observed in BOLD fMRI. Changes of this magnitude tend to occur with small pixel sizes (<2mm), and are associated with susceptibility changes in large draining veins (37-40).

1.1.2 fMRI IMAGING METHODS

BOLD fMRI was first demonstrated (5) with T2*-weighted EPI (41), and EPI remains the imaging method of choice for most fMRI studies. In EPI (Echo-Planar

Imaging), a single RF pulse excites the slice of interest, and field gradients are rapidly alternated to Fourier encode a complete image in less than 100 ms. This short acquisition time makes EPI images immune to intra-image motion and physiological variations. The speed of EPI also permits multi-slice coverage of the entire brain in only a few seconds. EPI also permits the use of diffusion gradients in specialized studies of fMRI mechanisms (42,43). EPI variants, such as asymmetric spin-echo EPI, permit separate measurement of T2 and T2' components of T2* (44). The disadvantages of EPI are that it requires fast gradients, extreme field homogeneity, and permits only limited spatial resolution.

T2*-weighted FLASH imaging (45) has also been used extensively for fMRI studies. In FLASH imaging, each line of Fourier space is encoded with a separate RF pulse repetition (phase encode step). The time required to acquire an image is equal to the number of phase encode steps times the repetition time (TR). Five to ten seconds is typical. During this time physiological variations related to respiration and heartbeat can occur, which is the principal pitfall of FLASH fMRI. The advantages of FLASH fMRI are that it can be implemented on any scanner, and it permits high spatial resolution. Versions of FLASH have been developed for acquiring multiple slices simultaneously (46,47), although at the price of decreased SNR and increased sensitivity to physiology. Magnetization-prepared FLASH ("turbo FLASH") sequences have also been developed for fMRI (48). In these sequences, a T2*-weighting is imposed on the longitudinal magnetization which is then rapidly read out with short-TR FLASH in less than one second. The resulting images are immune to physiological variations as in EPI, but suffer

from decreased SNR due to the low flip angle and high bandwidth of the rapid FLASH readout.

A FLASH variant known as spiral imaging has also been used for fMRI (49-51). In spiral imaging, Fourier space is encoded in a spiral pattern instead of the rectilinear pattern of conventional FLASH. The advantage of spiral imaging is that Fourier space is covered faster, with fewer RF repetitions, so that image acquisition times are on the order of one second. Also, the center of Fourier space is sampled redundantly so that intra-image physiological variations are diminished by averaging. The principal problem of spiral imaging is the complex gradient programming and image reconstruction software required for implementation.

Instead of T2*-weighted gradient echo imaging, T2-weighted spin echo methods such as spin echo EPI or RARE ("turbo spin echo") can also be used for BOLD fMRI (52). In spin echo imaging, a 180° pulse refocusses signal that is lost due to static dephasing in conventional gradient echo imaging. As a result, fMRI signal change from static extravascular water (especially tissue surrounding large veins) is minimized, and small signal changes originating directly from moving blood in capillary beds is preferentially detected. The method thus sacrifices sensitivity for enhanced specificity. Since functional signal changes with even T2* methods are often barely large enough to be detected, the sensitivity cost of T2 fMRI can usually not be afforded.

fMRI has also been demonstrated with exotic BURST sequences (53-55). In BURST imaging, images are Fourier encoded by a train of extremely rapid low flip-angle RF pulses in the presence of a weak gradient. Reversal of the gradient causes a series of stimulated echoes to appear that can be read out to form an image in as little as 30 ms. BURST imaging is characterized by extreme speed and acoustic silence (minimal gradient play). However the low SNR of the method will likely restrict it to only specialized applications, such as perhaps sleep study.

1.1.3 fMRI IMAGE ANALYSIS

In a typical functional imaging experiment, the brain is subjected to some form of structured activity, either sensory, motor, or cognitive. The simplest activity structures, or "paradigms" are binary: The brain is assumed to be either active or at rest at various times during the experiment. Functional activation maps are constructed by comparing MR images obtained during the presumed active and rest periods.

The simplest form of fMRI analysis is image subtraction (38). The mean of all "rest" images is subtracted from the mean of all "active" images to obtain an activation map. The merit of subtraction maps is that they indicate the actual magnitude of functional signal change in active brain areas. They can therefore be useful for studying basic mechanics of fMRI. The disadvantage of subtraction maps is that they offer no

information on the statistical significance of apparent activations. More sophisticated analysis methods are therefore used for neuroscientific study.

Student's t-test is frequently used in fMRI analysis (25). The t-test assigns a probability to the null-hypothesis that nominal active and rest images originate from the same statistical distribution. Pixels in truly active areas will have a mean intensity during active periods that is different than during rest periods, and the t-test measures the statistical significance of this difference. Setting a significance threshold (such as $p<0.01$) then gives an activation map.

Correlation analysis (56) offers a more flexible alternative to the t-test. In correlation analysis, the time course of each pixel over a set of images is cross-correlated with an expected activation response function. Pixels with correlation coefficients in excess of a predetermined threshold (such as >0.5) then comprise the activation map.

Cluster analysis (57) and fuzzy clustering (58) have also been used successfully to detect activations in fMRI datasets. In cluster analysis, pixel time courses are grouped into clusters based on similar time course behavior. The advantage of clustering methods is that they do not require any *a priori* assumptions about activation time courses. They are therefore ideally suited for the detection of novel activation patterns.

Activation maps produced by the aforementioned methods typically exhibit spatial correlations; activated pixels often occur in spatial clusters that define active brain regions. Cluster size thresholding (59,60) (not to be confused with time course cluster analysis described above) is therefore valuable for better defining active areas by discarding isolated false-active pixels due to noise.

1.1.4 fMRI ARTIFACTS

fMRI depends on the detection of small signal changes in MR images of the brain. Signal changes that are unrelated to brain activation may be called "noise." False-positive and false-negative activation detections resulting from noise are "artifacts." This discussion summarizes known causes of noise (hence artifacts) in blood-oxygen-level-dependent (BOLD) fMRI.

While scanner stability (61) is a prerequisite for successful fMRI, in practice biological sources of noise dominate fMRI experiments. Fig. 1.2 shows a comparison of temporal standard deviation images obtained for a water bottle and a living human brain. The water bottle images contain only a low level of electronic noise associated with thermal movement of ions in solution. The brain images, however, exhibit signal variations up to 50% of the mean signal level. Such large instabilities in raw images are not unusual in fMRI experiments, and can easily cause artifactual (false-positive or false-negative) brain activation results. This led to speculation as recently as 1995 (62) that *all*

supposed activations detected by BOLD fMRI experiments were artifactual! While this speculation was rebutted effectively in a counter-point paper (63), image instability and associated artifacts remain a formidable challenge in fMRI.

Sources of noise in fMRI are numerous and diverse. Early on it was recognized that fMRI brain images, particularly grey matter and CSF areas, exhibited greater signal variation than could be accounted for by simple electronic noise (64,65). Temporal noise power spectra analysis of EPI images revealed large noise peaks at cardiac and respiratory frequencies(64,66,67). These pulsatile signal variations may be explained, at least in part, by the slight swelling and contraction of the brain that is known to occur as blood pressure changes with heartbeat and breathing. Cardiac-related brain motion can be as large as 0.5 mm (68,69). Gross motion of the head is also a major cause of fMRI image instability, producing artifacts that can easily be mistaken for brain activation (70).

Flow, particularly flow-related enhancement (71), is another major source of noise and artifacts in fMRI (72-74). Pulsatile flow is a likely contributor to cardiac-frequency instabilities observed in fMRI images (64,66,67). In multi-shot imaging (e.g. FLASH), pulsatile flow also causes images of vessels and ventricles to "ghost" into adjacent areas, corrupting fMRI data in those areas (75).

Flow-related enhancement artifacts are a manifestation of a more general class of artifacts that can be called "slice saturation effects". Under certain imaging conditions,

notably single-slice high repetition rate (short TR) imaging, the magnetization of spins inside the slice being image becomes suppressed. Any "fresh" spins entering the slice during imaging will therefore generate anomalous hyper-intense signal. Flow-related enhancement is a manifestation of this. However bulk out-of-plane motion also causes the entry of fresh hyper-intense spins into the slice, creating yet another type of "slice saturation" artifact (76,77).

While flow causes noise and artifacts, it is also an integral part of the physiology of fMRI. (Increased flow causes increased oxygenation, which is the basis of BOLD fMRI.) It should therefore be noted that flow-related enhancement can sometimes increase the sensitivity of fMRI experiments that would otherwise rely on BOLD effects alone. However, this enhanced sensitivity is at the price of reduced specificity because flow-related enhancement predominately occurs in large blood vessels (78) not capillaries. Flow-sensitive fMRI is therefore preferentially sensitive to vessels feeding and draining active cortex rather than the active cortex itself.

This leads to the infamous "brain vs. vein" issue of fMRI (72). BOLD fMRI detects changes in blood oxygenation associated with brain activation. But activation-related oxygenation changes in capillaries also propagate into draining veins, so that draining veins can also appear "active" in fMRI experiments. This effect is independent of the aforementioned flow effect, and remains a concern even in flow-insensitive fMRI experiments. One solution to this problem is to image at low spatial resolution; high

spatial resolution preferentially sensitizes fMRI experiments to the steep susceptibility gradients near draining veins (39,40). Another solution is to exploit the temporal phase shift (time delay of several seconds) between cortical response and draining vein response to functional stimulus to distinguish the two effects (79). Yet another solution is spin-echo (T2-weighted) fMRI, although the decrease in sensitivity with this method is usually unacceptable.

MR signal phase variations associated with heartbeat and breathing are another important source of image instability in multi-shot MR imaging, especially FLASH imaging (80-90). It's not unusual for this artifact to dominate over all other causes of noise in FLASH fMRI (as it does in Fig. 1.2, for example). These global phase variations were initially attributed to physiology-correlated brain movement (82,84). However it now seems more likely that the phase variations are an indirect effect resulting from movement of organs outside the head, and associated small changes in the main magnetic field of the magnet (81,90).

Finally, once all external sources of noise have been accounted for in fMRI, a deeper issue remains. At some level, the functioning of the brain itself undoubtedly possesses an inherent noise. In contrast to other sources of noise discussed in this work, this "functional noise" or "activation noise" would be caused by oxygenation changes that are unrelated to obvious mental activity. The study of "activation noise" in the resting state of the brain is only in its infancy (91). It remains to be determined to what extent

natural oxygenation fluctuations in the brain may limit the sensitivity of fMRI experiments.

1.2 MATERIALS AND METHODS

1.2.1 MAGNETIC RESONANCE IMAGING

The research described in this dissertation was performed at the Institute for Biodiagnostics (IBD) of the National Research Council of Canada (NRC) in Winnipeg, Manitoba, Canada. MR imaging was performed in a Magnex 3 Tesla magnet with a Bruker Biospec console, Morris Instruments quadrature head coil, and Bruker UXNMR pulse programming environment. Protocols for imaging human volunteers were approved by the Human Ethics Committee of the National Research Council. Informed consent was obtained from each volunteer.

Functional imaging studies were performed using the FLASH ("fast low-angle shot") (45) imaging technique, unless otherwise stated. All slices were imaged with a 25 cm field of view (FOV) and 5 mm slice thickness, unless otherwise stated. Anatomic scout imaging to locate slices for functional study was performed with a T1-weighted inversion-recovery prepared turbo-FLASH sequence (TR/TE =14/7 ms, α=20°, 256 x 256 matrix) in four interleaved steps with an inversion time of 0.9 seconds. BOLD fMRI was performed by acquiring consecutive (no inter-image delay) T2*-weighted FLASH images

(TR/TE = 74/40 ms, 128 x 256 matrix) at various flip angles with a 30 Hz/pixel bandwidth (32.768 ms readout time). Flow compensation was used on the slice selection gradient. The first image of each consecutive set was discarded so that all analyzed images were in NMR equilibrium.

1.2.2 COMPUTING

Computer programs for image reconstruction, artifact correction, image registration and other tasks were written in the IDL computer language (Research Systems, Inc.), and run on a SGI Challenge XL server with an R4400 processor operating at 150 MHz.

1.3 THESIS OVERVIEW

The work described in this dissertation is application-driven. Rather than an in-depth study of a specific phenomenon, it is a collection of problems that were identified and solved (or partly solved) over the course of three years of providing physics support to the functional imaging group at IBD.

Three principal classes of fMRI artifacts are dealt with in this work: Artifacts due to blood flow, artifacts due to intra-image phase fluctuation, and artifacts due to inter-image motion. Chapter 2 discusses the physical origin and nature of these artifacts.

Chapters 3-5 describe specific techniques developed to minimize the artifacts. (These chapters are presented in the sequence that the corrective measures are implemented: Flow control at image acquisition, phase control during image reconstruction, and motion control in image post-processing.) Finally, Chapter 6 discusses the synergy resulting from the combination of these techniques in fMRI studies.

REFERENCES

1. C. S. Roy, C. S. Sherrington, On the regulation of the blood supply of the brain. *J. Physiol (Lond)* **11**, 85-108 (1890).

2. D. J. Wyper, Functional neuroimaging with single photon emission computed tomography (SPECT). *Cerebrovasc-Brain-Metab-Rev.* **5(3)**, 199-217 (1993).

3. C. J. Aine, A conceptual overview and critique of functional neuroimaging techniques in humans: I. MRI/FMRI and PET. *Crit-Rev-Neurobiol.* **9(2-3)**, 229-309 (1995).

4. J. W. Belliveau, D. N. Kennedy Jr., R. C. McKinstry, B. R. Buchbinder, R. M. Weisskoff, M. S. Cohen, J. M. Vevea, T. J. Brady, and B. R. Rosen, Functional mapping of the human visual cortex by magnetic resonance imaging. *Science* **254**, 716-719 (1991).

5. K. K. Kwong, J. W. Belliveau, D. A. Chesler, I. E. Goldberg, R. M. Weisskoff, B. P. Poncelet, D. N. Kennedy, B. E. Hoppel, M. S. Cohen, R. Turner, Dynamic magnetic resonance imaging of human brain activity during primary sensory stimulation. *Proc. Natl. Acad. Sci. (USA)* **89(12)**, 5675-5679 (1992).

6. R. R. Edelman, B. Siewart, D. G. Garby, V. Thangaraj, A. C. Nobre, M. M. Mesulam, and S. Warach, Qualitative mapping of cerebral blood flow and functional localization with echo-planar MR imaging and signal targeting with alternating radio frequency. *Radiology* **192**, 513-520 (1994).

7. S.-G. Kim, Quantification of relative cerebral blood flow change by flow-sensitive alternating inversion recovery (FAIR) technique: Application to functional mapping. *Magn. Reson. Med.* **34**, 293-301 (1995).

8. E. C. Wong, R. B. Buxton, L. R. Frank, A method for dynamic imaging of blood volume, *in* "Proc., ISMRM Annual Meeting, Vancouver, 1997," p. 372.

9. L. Pauling, C. D. Coryell, The magnetic properties and structure of hemoglobin, oxyhemoglobin, and carbonmonoxyhemoglobin. *Proc. Natl. Acad. Sci. (USA)* **22**, 210-216 (1936).

10. J. S. Philo, U. Dreyer, T. M. Schuster, Diamagnetism of human apo-, oxy-, and (carbonmonoxy)-hemoglobin, *Biochemistry* **23**, 865-872 (1984).

11. J. F. Schenck, Review article: Role of magnetic susceptibility in MRI. *Med. Phys.* **23**, 815-850 (1996).

12. K. R. Thulborn, J. C. Waterton, P. M. Mattews, G. K. Radda, Oxygenation dependence of the tranverse relaxation time of water protons in whole blood at high field. *Biochim. Biophys. Acta* **714**, 265-270 (1982).

13. R. M. Weisskoff, S. Kiihne, MRI susceptrometry: Image based measurement of absolute susceptibility of MR contrast agents and human blood. *Magn. Reson. Med.* **24**, 375-383 (1992).

14. S. Ogawa, T.-M. Lee, Magnetic resonance imaging of blood vessels at high field: in vivo and in vitro measurements and image simulation. *Magn. Reson. Med.* **16**, 9-18 (1990).

15. S. Ogawa, T.-M. Lee, A. R. Kay, D. W. Tank, Brain magnetic resonance imaging with contrast dependent on blood oxygenation. *Proc. Natl. Acad. Sci. (USA)* **87**, 9868-9872 (1990).

16. S. Ogawa, T. M. Lee, A. S. Nayak, P. Glynn, Oxygenation-sensitive contrast in magnetic resonance image of rodent brain at high magnetic magnetic fields. *Magn. Reson. Med.* **14**, 68-78 (1990).

17. R. Turner, D. Le Bihan, C. T. Moonen, D. Despres, J. Frank, Echo-planar time course MRI of cat brain oxygenation changes. *Magn. Res. Med.* **22**, 159-166 (1991).

18. S. Ogawa, D. W. Tank, R. Menon, J. M. Ellerman, S.-G. Kim, H. Merkle, K. Ugurbil, Intrinsic signal changes accompanying sensory stimulation: functional brain mapping with magnetic resonance imaging, *Proc. Natl. Acad. Sci. (USA)* **89**, 5951-5955 (1992).

19. P. A. Bandettini, E. C. Wong, R. S. Hinks, R. S. Tikofsky, J. S. Hyde, Time course EPI of human brain function during task activation. *Magn. Reson. Med.* **25**, 390-398 (1992).

20. J. Frahm, H. Bruhn, K. D. Merboldt, W. Hanicke, Dynamic MR imaging of human brain oxygenation during rest and photic stimulation. *J. Magn. Reson. Imaging* **2(5)**, 501-505 (1992).

21. A. M. Blamire, S. Ogawa, K. Ugurbil, D. Rothman, G. McCarthy, J. M. Ellerman, F. Hyder, Z. Rattner, R. G. Shulman, Dynamic mapping of the human visual cortex by high-speed magnetic resonance imaging. *Proc. Natl. Acad. Sci. (USA)* **89**, 11069-11073 (1992).

22. R. Turner, P. Jezzard, H. Wen, K. K. Kwong, D. Le Bihan, T. Zeffiro, R. S. Balaban, Functional mapping of the human visual cortex at 4 and 1.5 Tesla using deoxygenation contrast EPI. *Magn. Reson. Med.* **29**, 277-279 (1993).

23. S.-G. Kim, J. Ashe, A. P. Georgopoulos, H. Merkle, J. M. Ellerman, R. S. Menon, S. Ogawa, K. Ugurbil, Functional imaging of human motor cortex at high magnetic fields. *J. Neurophysiol.* **69**, 297-302 (1993).

24. R. M. Hinke, X. Hu, A. E. Stillman, S.-G. Kim, H. Merkle, R. Salmi, K. Ugurbil, Functional magnetic resonance imaging of Broca's Area during internal speech. *NeuroReport* **4**, 675-678 (1993).

25. R. T. Constable, G. McCarthy, T. Allison, A. W. Anderson, J. G. Gore, Functional brain imaging at 1.5 tesla using conventional gradient-echo MR imaging techniques. *Magn. Reson. Imaging* **11**, 451-459 (1993).

26. W. Schneider, D. C. Noll, J. D. Cohen, Functional topographic mapping of the cortical ribbon in human vision with conventional MRI scanners. *Nature* **365**, 150-153 (1993).

27. S.-G. Kim, J. Ashe, K. Hendrich, J. M. Ellerman, H. Merkle, K. Ugurbil, A. P. Georgopolous, Functional magnetic resonance imaging of motor cortex: hemispheric asymmetry and handedness. *Science* **261**, 615-617 (1993).

28. Y. Cao, V. L. Towle. D. N. Levin, J. M. Balter, Functional mapping of human motor cortical activation by conventional MRI at 1.5 T. *J. Magn. Reson. Imaging* **3**, 869-875 (1993).

29. S. M. Rao, J. R. Binder, P. A. Bandettini, T. A. Hammeke, F. Z. Yetkin, A. Jesmanowicz, L. M. Liks, G. L. Morris, W. M. Mueller, L. D. Estkowski, E. C. Wong, V. M. Haughton, J. S. Hyde, Functional magnetic resonance imaging of complex human movements. *Neurology* **43**, 2311-2318 (1993).

30. G. McCarthy, A. M. Blamire, D. L. Rothman, R. Gruetter, R. Shulman, Echo-planar magnetic resonance imaging studies of frontal cortex activation during word generation in humans. *Proc. Natl. Acad. Sci. (USA)* **90**, 4952-4956 (1993).

31. P. T. Fox, M. E. Raichle, Focal physiological uncoupling of cerebral blood flow and oxidative metabolism during somatosensory stimulation in human subjects. *Proc. Natl. Acad. Sci. (USA)* **83**, 1140-1144 (1986).

32. P. T. Fox, M. E. Raichle, M. A. Mintun, C. Dence, Nonoxidative glucose consumption during focal physiologic neural activity. *Science* **241**, 462-464 (1988).

33. R. B. Buxton, L. R. Frank, A physiological model for the interpretation of functional MR brain activation studies, *in* "Proc., SMRM,12th Annual Meeting, New York, 1993," p. 4.

34. C. R. Fisel, J. L. Ackerman, R. B. Buxton, L. Garrido, J. W. Belliveau, B. R. Rosen, T. J. Brady, MR contrast due to microscopically heterogeneous magnet susceptibility: numerical simulations and applications to cerebral physiology. *Magn. Reson. Med.* **17**, 336-347 (1991).

35. S. Ogawa, R. S. Menon, D. W. Tank, S.-G. Kim, H. Merkle, J. M. Ellermann, K. Ugurbil, Functional brain mapping by blood oxygenation level-dependent contrast magnetic resonance imaging: a comparison of signal characteristics with a biophysical model. *Biophys. J.* **64**, 803-812 (1993).

36. R. P. Kennan, J. Zhong, J. C. Gore, Intravascular susceptibility contrast mechanisms in tissues. *Magn. Reson. Med.* **31**, 9-21 (1994).

37. J. Frahm, K. D. Merboldt, W. Hanicke, Functional MRI of human brain activation at high spatial resolution. *Magn. Reson. Med.* **29**, 139-144 (1993).

38. R. S. Menon, S. Ogawa, D. W. Tank, K. Ugurbil, 4 Tesla gradient recalled echo characteristics of photic stimulation-induced signal changes in the human primary visual cortex. *Magn. Reson. Med.* **30**, 380-386 (1993).

39. S. Lai, A. L. Hopkins, E. M. Haacke, D. Li, B. A. Wasserman, P. Buckley, L. Friedman, H. Meltzer, P. Hedera, R. Friedland, Identification of vascular structures as a major

source of signal contrast in high resolution 2D and 3D functional activation imaging of the motor cortex at 1.5T: preliminary results. *Magn. Reson. Med.* **30**, 387-392 (1993).

40. E. M. Haacke, A. Hopkins, S. Lai, P. Buckley, L. Friedman, H. Meltzer, P. Hedera, R. Friedland, S. Klein, L. Thompson, D. Detterman, J. Tkach, J. S. Lewin, 2D and 3D high resolution gradient echo functional imaging of the brain: venous contributions to signal in motor cortex studies. *NMR in Biomedicine* **7**, 54-62 (1994).

41. P. Mansfield, Multi-planar image formation using NMR spin echoes. *J. Phys. C* **10**, L55-L58 (1977).

42. J. L. Boxerman, P. A. Bandettini, K. K. Kwong, J. R. Baker, T. L. Davis, B. R. Rosen, R. M. Weisskoff, The intravascular contribution to fMRI signal change: Monte Carlo modeling and diffusion-weighted studies in vivo. *Magn. Reson. Med.* **34**, 4-10 (1995).

43. A. W. Song, E. C. Wong, S. G. Tan, J. S. Hyde, Diffusion weighted fMRI at 1.5 T. *Magn. Reson. Med.* **35**, 155-158 (1996).

44. B. E. Hoppel, R. M. Weisskoff, K. R. Thulborn, J. B. Moore, K. K. Kwong, B. R. Rosen, Measurement of regional blood oxygenation and cerebral hemodynamics. *Magn. Reson. Med.* **30**, 715-723 (1993).

45. J. Frahm, A. Haase, D. Matthaei, Rapid NMR imaging of dynamic processes using the FLASH technique, *Magn. Reson. Med.* **3**, 321 (1986).

46. G. Liu, G. Sobering, J. Duyn, C. T. Moonen, A functional MRI technique combining principles of echo-shifting with a train of observations (PRESTO). *Magn. Reson. Med.* **30**, 764-768 (1993).

47. T. Loenneker, F. Hennel, J. Hennig, Multislice interleaved excitation cycles (MUSIC): An efficient gradient-echo technique for functional MRI. *Magn. Reson. Med.* **35**, 870-874 (1996).

48. X. Hu, S.-G. Kim, A new T2*-weighting technique for magnetic resonance imaging, *Magn. Reson. Med.* **30**, 512-517 (1993).

49. G. H. Glover, A. T. Lee, Motion artifacts in fMRI: Comparison of 2DFT with PR and spiral scan methods. *Magn. Reson. Med.* **33**, 624-635 (1995).

50. A. T. Lee, G. H. Glover, C. H. Meyer, Discrimination of large venous vessels in time-course spiral blood-oxygen-level-dependent magnetic-resonance functional neuroimaging. *Magn. Reson. Med.* **33**, 745-754 (1995).

51. Glover-GH; Lemieux-SK; Drangova-M; Pauly-JM, Decomposition of inflow and blood oxygen level-dependent (BOLD) effects with dual-echo spiral gradient-recalled echo (GRE) fMRI. *Magn. Reson. Med* **35**, 299-308 (1996).

52. R. T. Constable, R. P. Kennan, A. Puce, G. McCarthy, J. C. Gore, Functional NMR imaging using fast spin echo at 1.5 T. *Magn. Reson. Med* **31**, 686-690 (1994).

53. J. Hennig, M. Hodapp, Burst imaging. *MAGMA* **1**, 39-48 (1993).

54. E. C. Wong, Magnetic resonance functional neuroimaging using interleaved SUNBURST, *in* "Proc., SMR Annual Meeting, San Francisco, 1994," p. 25.

55. P. M. Jakob, K. O. Lovblad, G. Schlaug, S. Warach, R. R. Edelman, Functional burst imaging, *in* "Proc., ISMRM Annual Meeting, Vancouver, 1997," p. 373.

56. P. A. Bandettini, A. Jesmanowicz, E. C. Wong, J. S. Hyde, Processing strategies for time-course data sets in functional MRI of the human brain. *Magn. Reson. Med.* **30**, 161-173 (1993).

57. X. Ding, J. Tkach, P. Ruggieri, T. Masaryk, Analysis of Time-Course Functional MRI Data With Clustering Method Without Use of Reference Signal, *in* "Proc., SMR Annual Meeting, San Francisco, 1994," p. 630.

58. G. Scarth, M. McIntyre, B. Wowk, R. Somorjai, Detection of Novelty in Functional Images Using Fuzzy Clustering, *in* "Proc., SMR and ESMRMB Annual Meetings, Nice, 1995," p. 238.

59. W. Schneider, D. C. Noll, J. D. Cohen, Functional topographic mapping of the cortical ribbon in human vision with conventional MRI scanners. *Nature* **365**, 150-153 (1993).

60. S.D. Forman, J.D. Cohen, M. Fitzgerald, W. F. Eddy, M. A. Mintun, D. C. Noll, Improved assessment of significant activation in functional magnetic resonance imaging (fMRI): use of a cluster-size threshold. *Magn. Reson. Med.* **33**, 636-647 (1995).

61. R. M. Weisskoff, Simple measurement of scanner stability for functional NMR imaging of activation in the brain. *Magn. Reson. Med.* **36**, 643-645 (1996).

62. J. V. Hajnal, G. M. Bydder, I. R. Young, fMRI: Does correlation imply activation? *NMR in Biomedicine* **8**, 97-100 (1995).

63. R. M. Weisskoff, Functional MRI: Are we all moving towards artifactual conclusions? OR fMRI fact or fancy. *NMR in Biomedicine* **8**, 101-103 (1995).

64. R. M. Weisskoff, J. Baker, J. Belliveau, T. L. Davis, K. K. Kwong, M. S. Cohen, B. R. Rosen, Power spectrum analysis of functionally-weighted MR data: What's in the noise?, *in* "Proc., SMRM, 12th Annual Meeting, New York, 1993," p. 7.

65. P. Jezzard, D. LeBihan, C. Cuenod, L. Pannier, A. Prinster, R. Turner, An investigation of the contribution of physiological noise in human functional MRI studies at 1.5 Tesla and 4 Tesla, *in* "Proc., SMRM, 12th Annual Meeting, New York, 1993," p. 1392.

66. P. A. Bandettini, A. Jesmanowicz, E. C. Wong, J. S. Hyde, Processing strategies for time-course data sets in function MRI of the human brain. *Magn. Reson. Med.* **30**, 161-173 (1993).

67. B. Biswal, E. A. DeYoe, J. S. Hyde, Reduction of physiological fluctuations in fMRI using digital filters. *Magn. Reson. Med.* **35**, 107-113 (1996).

68. D. A. Feinberg, A. S. Mark, Human brain motion and cerebrospinal fluid circulation demonstrated with MR velocity imaging, *Radiology* **163**, 793-799 (1987).

69. B. P. Poncelet, V. J. Wedeen, R. M. Weisskoff, M. S. Cohen, Brain parenchyma motion: Measurement with cine echo-planar imaging. *Radiology* **185**, 645-651 (1992).

70. J. V. Hajnal, R. Myers, A. Oatridge, J. E. Schwieso, I. R. Young, G. M. Bydder, Artifacts due to stimulus correlated motion in functional imaging of the brain. *Magn. Reson. Med.* **31**, 283-291 (1994).

71. J. H. Gao, S. K. Holland, J. C. Gore, Nuclear magnetic resonance signals from flowing nuclei in rapid imaging using gradient echoes. *Med. Phys.* **15**, 809-814 (1988).

72. J. Frahm, K.-D. Merboldt, W. Hanicke, A. Kleinschmidt, H. Boecker, Brain or vein--oxygenation or flow? On signal physiology in functional MRI of human brain activation. *NMR in Biomedicine* **7**, 45-53 (1994).

73. S.-G. Kim, K. Hendrich, X. Hu, H. Merkle, K. Ugurbil, Potential pitfalls of functional MRI using conventional gradient-recalled echo techniques. *NMR in Biomedicine* **7**, 69-74 (1994).

74. J. H. Duyn, C. T. W. Moonen, G. H. van Ypern, R. W. de Boer, P. R. Luyten, Inflow versus deoxyhemoglobin effects in BOLD functional MRI using gradient echoes at 1.5 T. *NMR in Biomedicine* **7**, 83-88 (1994).

75. X. Hu, T. H. Le, T. Parish, P. Erhard, Retrospective estimation and correction of physiological fluctuation in functional MRI. *Magn. Reson. Med.* **34**, 201-212 (1995).

76. K. J. Friston, S. Williams, R. Howard, R. S. J. Frackowiak, R. Turner, Movement-related effects in fMRI time-series. *Magn. Reson. Med.* **35**, 346-355 (1996).

77. C. C. Lee, C. R. Jack, R. C. Grimm, P. J. Rossman, J. P. Felmlee, R. L. Ehman, S. J. Riederer, Real-time adaptive motion correction in functional MRI. *Magn. Reson. Med.* **36**, 436-444 (1996).

78. J. H. Gao, I. Miller, S. Lai, J. Xiong, P. Fox, Quantitative assessement of blood inflow effects in functional MRI signals. *Magn. Reson. Med.* **36**, 314-319 (1996).

79. A. T. Lee, G. H. Glover, C. H. Meyer, Discrimination of large venous vessels in time-course spiral blood-oxygen-level-dependent magnetic resonance functional neuroimaging. *Magn. Reson. Med.* **33**, 745-754 (1995).

80. D. C. Noll, W. Schneider, J. D. Cohen, Artifacts in functional MRI using conventional scanning, *in* "Proc., SMRM, 12th Annual Meeting, New York, 1993," p. 1407.

81. D. C. Noll, W. Schneider, Respiration artifacts in functional brain imaging: Sources of signal variation and compensation strategies, *in* "Proc., SMR, 2nd Annual Meeting, San Francisco, 1994," p. 647.

82. X. Hu, S.-G. Kim, Reduction of physiological noise in functional MRI using navigator echo. *Magn. Reson. Med.* **31**, 495-503 (1994).

83. D. C. Noll, J. O'Brien, Simulation of physiological effects in functional MRI, *in* "Proc., SMR/ESMRMB, Annual Meeting, Nice, 1995," p. 794.

84. G. H. Glover, A. T. Lee, Motion artifacts in fMRI: Comparison of 2DFT with PR and spiral scan methods. *Magn. Reson. Med.* **33**, 624-635 (1995).

85. X. Hu, T. H. Le, T. Parish, P. Erhard, Retrospective estimation and correction of physiological fluctuation in functional MRI. *Magn. Reson. Med.* **34**, 201-212 (1995).

86. T. H. Le, X. Hu, Retrospective estimation and correction of physiological artifacts in fMRI by direct extraction of physiological activity from MR data. *Magn. Reson. Med.* **35**, 290-298 (1996).

87. B. Wowk, M. C. McIntyre, J. K. Saunders, Physiologic artifact correction in fMRI without navigator echoes, *in* "Proc., ISMRM, 4th Annual Meeting, New York, 1996," p. 1822.

88. B. Wowk, M. C. McIntyre, J. K. Saunders, Origin and removal of fMRI physiological noise: a multi-modal approach, *in* "Proc., ISMRM, 5th Annual Meeting, Vancouver, 1997," p. 1690.

89. B. Wowk, M. C. McIntyre, J. K. Saunders, k-Space orthogonalization: A new remedy for fMRI physiological noise, *in* "Proc., ISMRM, 5th Annual Meeting, Vancouver, 1997," p. 351.

90. B. Wowk, M. C. McIntyre, J. K. Saunders, k-space detection and correction of physiological artifacts in fMRI. *Magn. Reson. Med.* **38**, in press (1997).

91. B. Biswal, F. Z. Yetkin, V. M. Haughton, J. S. Hyde, Functional connectivity in the motor cortex of resting human brain using echo-planar MRI, *Magn. Reson. Med.* **34**, 537-541 (1995).

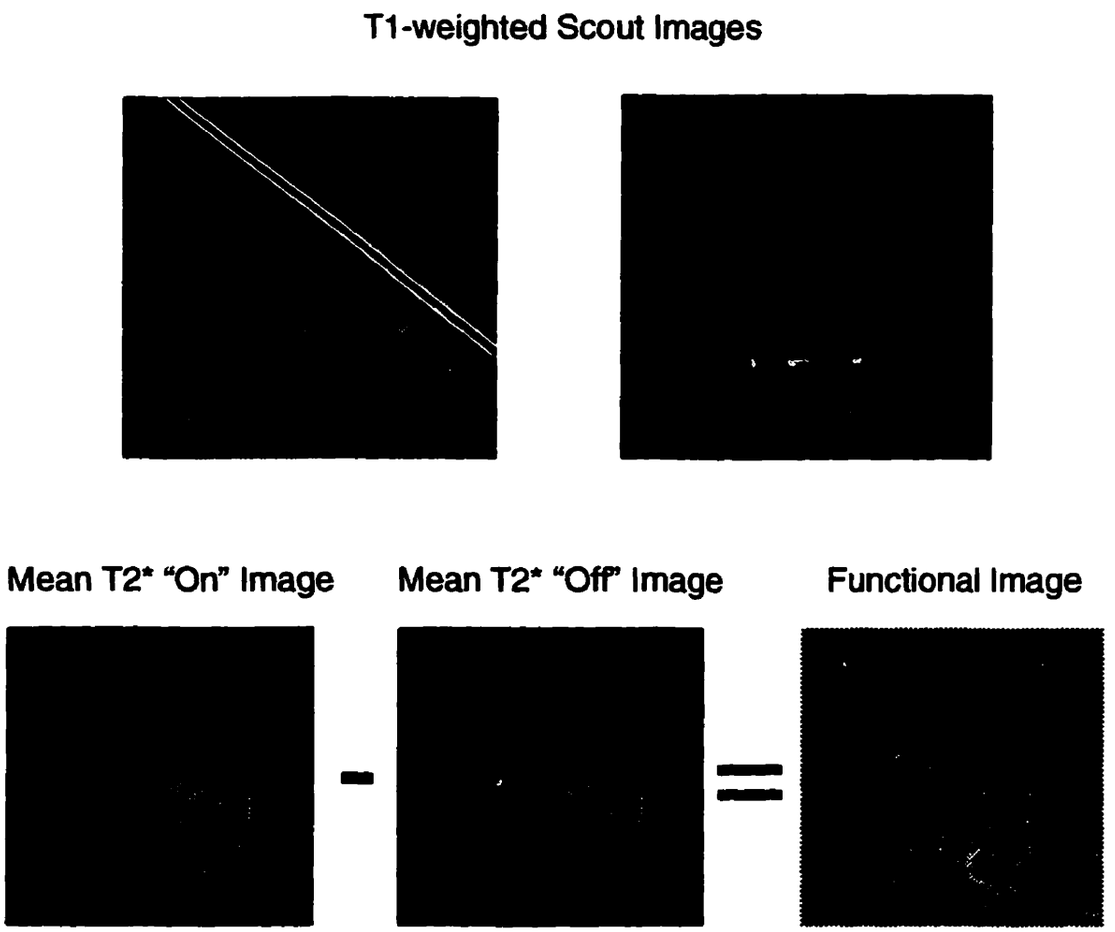

FIG. 1.1 A prototypical BOLD fMRI experiment at 3 Tesla. T1-weighted images locate an oblique slice passing through the calcarine fissure in the visual cortex. T2*-weighted FLASH images are obtained, and the difference between images obtained during visual stimulation (flashing lights) and without visual stimulation gives a functional activation map.

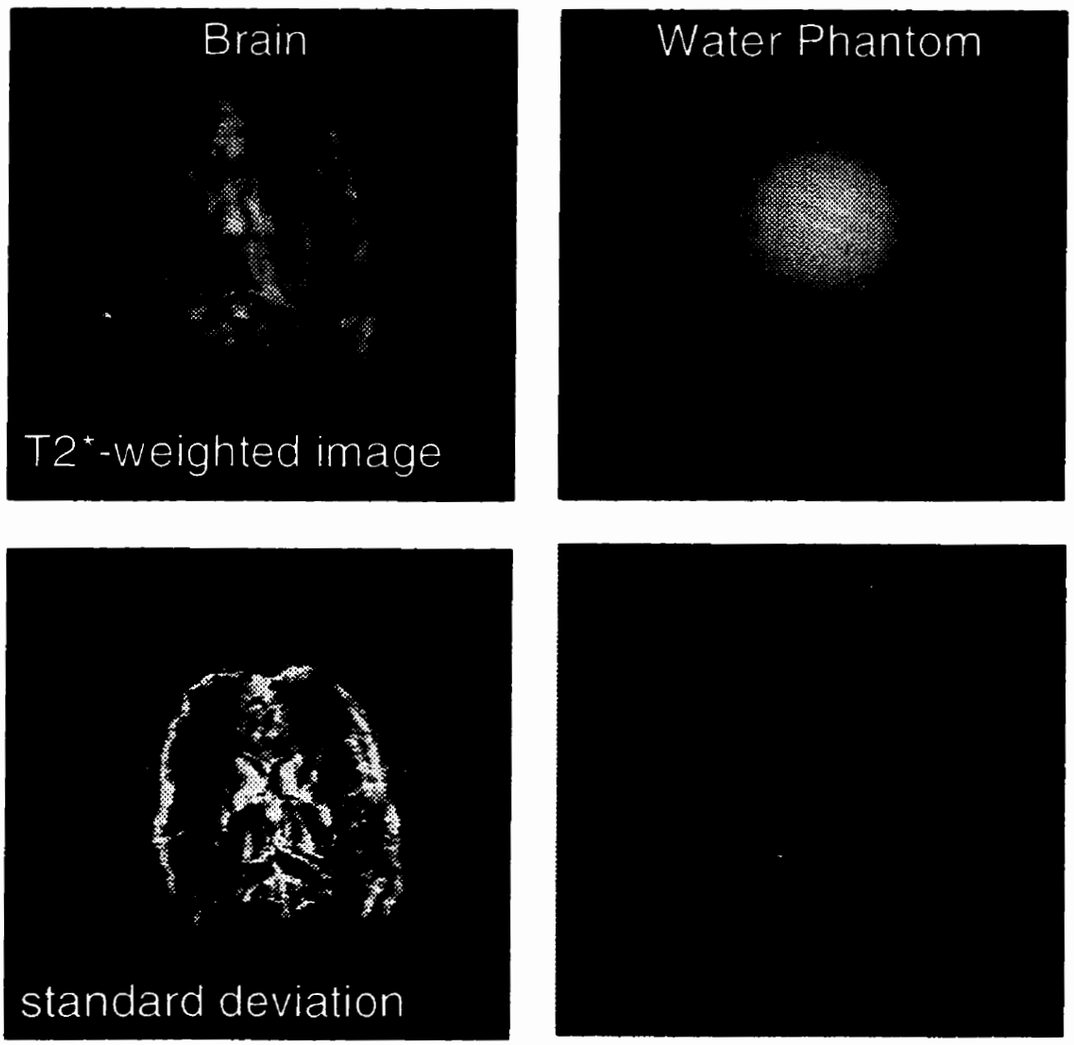

FIG. 1.2 Instability in FLASH MR images of living brain vs. water bottle. Standard deviation images represent the standard deviation of signal in each pixel over a time course of images. Brain images show signal variations up to 100 times greater than the intrinsic noise of the experiment.

Chapter 2

SOURCES OF ARTIFACTS

2.1 INTRODUCTION

This chapter explores the physical origins of three major classes of fMRI artifacts: flow-related artifacts, global phase variation artifacts, and gross motion artifacts. These artifacts comprise the bulk of image instabilities encountered in FLASH fMRI studies.

2.2 FLOW ARTIFACTS

Flow-related artifacts in MRI generally fall into two classes: phase effects, and inflow effects. Phase effects, causing flow-related signal loss, occur because the phase of moving spins is not properly refocused by imaging gradients, especially the slice selection gradient in its simplest form. These phase shifts can be overcome by using gradient waveforms with no first-order moment ("gradient moment nulling") (1,2,3). Gradient moment nulling, or first-order flow compensation, is therefore used for all slice selection gradients in the pulse sequences of this work.

Inflow effect, or flow-related enhancement (4,5), is a phenomenon related to progressive saturation of the magnetization of spins during imaging. Immediately after an RF pulse of flip angle θ, the longitudinal magnetization of spins will be $M_0\cos\theta$, where M_0 is the magnetization at thermal equilibrium before any RF excitation. After a time TR following excitation, the longitudinal magnetization will have regrown to

$$M = M_0(1 - e^{-TR/T_1}) + M_0 \cos\theta e^{-TR/T_1} \qquad [2.1]$$

where T1 is the longitudinal relaxation time. After *n* excitations repeated at intervals time TR apart, the longitudinal magnetization will be (4)

$$M = M_0(1 - e^{-TR/T_1})\left(\frac{1 - \cos^n\theta e^{-nTR/T_1}}{1 - \cos\theta e^{-TR/T_1}}\right) + M_0 \cos^n\theta e^{-nTR/T_1}. \qquad [2.2]$$

This progressive saturation of magnetization with time is shown in Fig. 2.1. In the presence of continued RF pulses, and spoiling of transverse magnetization between pulses, the longitudinal magnetization eventually reaches the equilibrium suppressed value (4)

$$M = M_0\left(\frac{1 - e^{-TR/T_1}}{1 - \cos\theta e^{-TR/T_1}}\right). \qquad [2.3]$$

Flow-related enhancement occurs via the mechanism of Fig. 2.2. During imaging of a slice, magnetization becomes suppressed as per Eq. [2.3]. Spins flowing into the slice from outside therefore appear anomalously bright on MR images. Fig. 2.3 shows in-vivo examples. Blood flowing fast enough to pass through the imaging volume in one TR time or less will appear maximally enhanced, with the enhancement given by the difference between M_0 and Eq. 2.3. The enhancement of slower flowing blood will be a complex function of vessel geometry, flow type (plug vs. laminar), and flow velocity

(4,5). In general, enhancement will increase with flow velocity until the threshold of maximal enhancement is reached.

Flow-related enhancement is a source of noise in fMRI because blood flow velocity varies with the cardiac cycle (pulsatile flow). Fig. 2.4(b) shows noise caused by pulsatile flow in pial vessels along the cortical surface. In multi-shot imaging, such as FLASH, pulsatile flow enhancement also causes ghosting of pulsing vessels and ventricles (6,7) into surrounding areas, as seen in Fig. 2.4.

Ghosting occurs in the presence of pulsatile flow with FLASH imaging because several cardiac cycles occur during the acquisition of a single FLASH image. This produces a periodic modulation of flow enhancement through k-space that can be represented by a Fourier series. Each term of the series creates a convolution with a displaced delta function in image space (Fourier shift theorem), giving rise to a ghost. The displacement of each ghost is proportional to the frequency of the associated Fourier series term, and the brightness is proportional to the amplitude of the associated term. Typically the brightest ghost is closest to the pulsing object, and is associated with the base frequency (cardiac frequency) of the modulation.

Out-of-plane bulk motion, or motion of anatomy in and out of the imaging slice, can cause artifacts similar to flow-related enhancement (8,9). This is illustrated in Fig.

2.4(d), where movement of the vitreous humor of the eye during imaging causes pronounced signal variation.

Apart from the noise and obvious artifacts caused by flow, there are also reasons to question the specificity of functional activations detected when BOLD imaging is also sensitive to changes in flow (10-13). Changes in blood flow associated with activation are known to encompass a wider area than changes in blood oxygenation (14). Also, flow-sensitive fMRI is primarily sensitive to flow changes in larger blood vessels rather than cortical capillary beds (15), making flow-sensitive fMRI results intrinsically non-local.

For all the above reasons, it is desirable to be able to perform BOLD fMRI experiments without flow sensitivity. Methods for doing so will be explored in Chapter 3.

2.3 PHASE VARIATION ARTIFACTS

2.3.1 INTRODUCTION

Fig. 2.5 shows the gradient and signal reception timing of a FLASH imaging sequence. Since the same gradient and RF pulse waveforms are used for each slice excitation, the MR signal phase after each slice excitation before phase encoding should

be invariant. However as Fig. 2.5 shows, this is not the case when imaging a living brain. Global phase variations ranging from 0.1 to 1 radians are observed to occur coincident with respiration, and smaller variations coincident with heartbeat are observed to occur during fMRI studies (16-26). These phase variations have previously been attributed to brain movement (18), brain pulsation (20), or movement of organs in the chest (17).

Physiological phase variations are not important to single-shot EPI imaging since a constant phase offset has no effect on the reconstruction of a final magnitude image. However for multi-shot imaging techniques such as FLASH, interleaved-EPI, and 3D EPI, these intra-image phase variations can be a major cause of image artifacts. When viewing FLASH images in a cine sequence, the problem manifests as rolling waves of distortion, or apparent movement when no actual physical movement took place. The problem typically worsens with increasing TE and field strength.

In this Chapter the nature of physiological phase variations seen in fMRI is explored. It is concluded that the variations are predominantly caused indirectly by movement of organs in the chest, and not by brain motion as previously claimed.

2.3.2 PHASE VARIATION MAPPING

To better understand physiological phase variations, it is possible to construct a "phase variation map" of how the phase of k-space (and navigator signal) as shown in

Fig. 2.5 changes from image-to-image. It is assumed that physiology causes a time-varying perturbation of the phase of each k-space point from a "true" phase, and that this true phase can be obtained by averaging the phase of each k-space point over a large number of images. The averaging process is not straightforward because the phase is only known modulo 2π, resulting in discontinuities through much of k-space. Instead of phase unwrapping, a simple averaging method based on phase differences was implemented. The mean phase of a k-space point is computed by

$$\overline{\Phi} = \Phi_1 + \frac{1}{N}\sum_{i=1}^{N}(\Phi_i - \Phi_1), \qquad [2.4]$$

where N is the total number of images, Φ_i is the phase of the point in image i, and Φ_1 is the phase of the point in a reference image (arbitrarily chosen to be the first image). The "phase variation" of the k-space point in image i is then defined by

$$\Delta\Phi_i = \Phi_i - \overline{\Phi}. \qquad [2.5]$$

The result of each phase subtraction is checked; 2π is subtracted if the difference $>\pi$ radians, and 2π is added if the difference $<-\pi$ radians. This check corrects any errors resulting from subtractions near phase discontinuities.

Fig. 2.6 shows k-space phase variation maps (including navigator signal) computed by Eqs. [2.4] and [2.5] for six consecutive images from a set of 24. A slow variation at the frequency of respiration dominates. Note that the amplitude of the phase variation increases with time after slice excitation, being larger in k-space than it is in the navigator signal.

The mean amplitude of the phase variation in k-space for each phase encode step can be computed by

$$\Delta\Phi_i(s) = \frac{\int_{k-space} \Delta\Phi_i(t',s) M_i(t',s) dt'}{\int_{k-space} M_i(t',s) dt'}, \qquad [2.6]$$

where $M_i(t,s)$ is the signal magnitude, t is time after slice excitation, s is phase encode number, and the integral is performed over time within the k-space readout window (horizontal axis of Figs. 2.5 and 2.6). These phase variations are plotted for the six images of Fig. 2.6 in Fig. 2.7. The phase variation of the navigator is computed analogously (averaging over time within each navigator acquisition), and also plotted in Fig. 2.7. The phase variation in k-space is approximately twice as large as the navigator variation, which is also the ratio of their respective echo-times (TE) after slice excitation.

Phase variations measured for each phase encode step through k-space over 19 images of another volunteer are shown in Fig. 2.8. The variation amplitude of Fig. 2.8 is

more typical of what is usually seen in functional studies of the neocortex at 3T. Interestingly, the variation can be decomposed by digital filtering into distinct respiratory and cardiac components. Low frequency (respiratory) components are obtained by convolving the raw variation with a σ=0.75s gaussian. High frequency (cardiac) components become evident after subtracting the respiratory component. Significantly, the cyclic patterns are virtually invariant in the presence of phase encoding through k-space. This supports previous observations (18,20) that the phase variations are global across the (transverse) imaging slice

2.3.3 PHASE VARIATION ARTIFACTS

Fig. 2.9 shows the image instabilities caused by physiological phase variations over 19 consecutive images at three different slice positions. Instabilities are greatest near feature edges. This is because rolling phase variation in k-space is a phase modulation similar to that caused by motion (Fourier shift theorem). Therefore physiological phase variation often looks like motion in a time series of MR images, even if the subject was absolutely still during imaging. The severity of the artifact is also observed to increase for progressively inferior slice positions.

2.3.4 FIELD VARIATION MAPPING

The amplitude of physiological phase variations is observed to increase approximately linearly with time after slice excitation. This time evolution indicates that the variation is not merely a phase offset introduced during slice excitation and refocusing (as motion would cause), but rather an actual change in the resonant frequency of the MR signal. This change in Larmor frequency

$$\omega = \gamma B0 \qquad (\gamma = 42.5 \text{ MHz/T for protons}) \qquad [2.7]$$

indicates that the strength of B0, the main magnetic field, is changing in concert with respiration and heartbeat. Furthermore, the amount of field variation appears to depend on slice position.

These results suggest that it would be very interesting to map the variation of B0 within an image as a function of respiration. Changes in the phase of the MR signal can be used to detect changes in resonant frequency, hence field strength. However even with only 64 phase encode steps, the 5 seconds required to acquire a conventional FLASH image (TR = 74 ms) is too long to capture images at fixed points in the respiratory cycle. Instead, the reordered phase encode scheme of Fig. 2.10 was employed.

In reordered phase encode imaging, instead of acquiring 100 consecutive FLASH images, a single FLASH image with 64 phase encode steps is acquired over an 8 minute time period with each phase encode step repeated 100 times. Each block of 100 phase

encode repetitions is sufficiently long (7.4 seconds) to cover a complete respiratory cycle. It is therefore possible to retrospectively choose a phase encode sample from each group of 100 that corresponds to a particular point in the respiratory cycle (respiration having been recorded by a navigator echo). Images corresponding to instantaneous snapshots of particular points in the respiratory cycle can then be reconstructed. Subtracting phase images corresponding to the top and bottom of the respiratory cycle gives a map of the phase variation, hence B0 field variation, associated with respiration (Fig. 2.11).

Fig. 2.12 shows the respiratory field variations recorded in sagittal and coronal planes by the reordered phase encode method. The variation is mostly featureless (global), showing a slow increase in the inferior direction. There are also some discrete areas of large field change, possibly associated with susceptibility changes in large blood vessels.

2.3.5 SOURCE OF VARIATIONS

Noll *et al* (17) concluded that physiological phase variations observed during fMRI were caused by movement of organs in the chest. The volume magnetic susceptibility of tissue is about -9.0×10^{-6} (SI units) compared to 0.36×10^{-6} for air (27). The presence of a person in a magnet therefore introduces a small perturbation in the main magnetic field, B0. If any tissue/air interfaces are moving, such as the heart/lung interface or diaphram/lung interface, a time-varying disturbance in B0 will occur. Noll *et*

al supported chest organ movement as the cause of physiological B0 variations by showing that respiration-related phase variations could even be detected in phantoms placed outside the head, with variations being strongest when the phantom was positioned near the neck above the shoulders.

Studies in this work add further support to the Noll interpretation. For example, the RMS phase variations detected while imaging the slices of Fig. 2.9 were 0.196, 0.261, 0.340 radian for z=+25 mm, 0 mm, and -25 mm respectively (negative position closest to the chest). These variations, when plotted as a function of cube root distance from a point 30 cm below the top slice, form a straight line (Fig. 2.13). This is consistent with a dipolar (or spherically symmetric) B0 perturbation located within the chest.

2.3.6 FIELD PERTURBATION CALCULATIONS

Experimental evidence is consistent with the hypothesis that phase variations observed during fMRI are caused by movement of organs within the chest. In this section the expected perturbations in the main magnetic field B0 due to movement of the heart and lungs will be calculated from first principles.

Consider the simplified model of the body in Fig 2.14. The heart and blood within it are modeled as a sphere of 4 cm radius. During systole the heart is assumed to contract to a radius of 3.6 cm, giving a normal cardiac stroke volume of 70 ml (28). The

heart resides inside the chest cavity which is assumed to have a density equal to lung tissue, which is about 1/4 as dense as water (29). The abdomen is modeled as a sphere of 15 cm radius. Since normal quiet breathing is accomplished almost entirely by the diaphram (28), respiration is modeled as a 0.7 cm displacement of the abdomen toward and then away from the chest, giving a tidal respiration volume of 500 ml (28).

The heart and abdomen are modeled as spheres because the magnetic field disturbance produced by a sphere is easy to calculate. If the susceptibility difference between the sphere and the surrounding medium is $\Delta\chi$, and $\Delta\chi$ is small, the perturbation outside the sphere along the axis of the magnetic field will be given by (27)

$$\frac{\Delta B0}{B0} = \frac{2\Delta\chi}{3}\left(\frac{r_0}{r}\right)^3 \qquad [2.8]$$

where r_0 is the radius of is the sphere, r is the distance of the measurement point from the center, B0 is the applied magnetic field, and $\Delta B0$ is the measured field perturbation.

The SI volume magnetic susceptibility of tissue varies between χ=-7.0 x 10^{-6} and -11 x 10^{-6} (27), but is typically close to that of water at -9.0 x 10^{-6}. If we take χ=-9 x 10^{-6} for the heart and abdomen, and χ= -2 x 10^{-6} for the chest cavity, then $\Delta\chi$= 7 x 10^{-6}. The main field perturbation in the brain, 45 cm away from the center of the abdomen, due to respiration is therefore expected to be

$$\frac{2\Delta\chi}{3}\left(\left(\frac{15\text{cm}}{45\text{cm} - 0.7\text{cm}}\right)^3 - \left(\frac{15\text{cm}}{45\text{cm}}\right)^3\right) = 0.009 \text{ ppm.} \qquad [2.9]$$

This is in rough agreement with the 0.013 ppm peak-to-peak field change responsible for the 0.4 radian variations seen in the typical fMRI study of Fig. 2.8. The field perturbation due to the heart beating 25 cm away from the brain is expected to be

$$\frac{2\Delta\chi}{3}\left(\left(\frac{4\text{cm}}{25\text{cm}}\right)^3 - \left(\frac{3.6\text{cm}}{25\text{cm}}\right)^3\right) = 0.006 \text{ ppm,} \qquad [2.10]$$

or about half the respiratory variation. This is also consistent with observations. Thus the phase shifts observed in the brain during fMRI are of the same magnitude that is theoretically expected due to natural movement of the heart and lungs.

2.4 MOTION ARTIFACTS

Gross motion during imaging is an obvious and important source of artifacts in fMRI (30). fMRI depends on detecting small image-to-image signal changes in specific anatomical areas. If the anatomy contained within a voxel changes over time due to motion, localization of activation becomes uncertain. More seriously, if a voxel is on or near the edge of a high contrast feature, artifactual signal change will be introduced. Fig.

2.15 shows artifactual signal changes near feature edges resulting from motion during a functional study.

A typical fMRI experiment lasts at least several minutes, and even with head restraints, small motions are inevitable. Small motions cannot be disregarded. The signal change, ΔI, associated with a motion Δx will be given approximately by

$$\Delta I \approx \frac{dI}{dx}\Delta x \qquad \text{Eq. [2.11]}$$

where dI/dx is the image intensity gradient in the area (31). Where the gradient is steep, such as at a sharp edge, as little as a 1/8 pixel displacement can produce a signal change on the order of 10% (32). This is a change larger than is seen with most functional activations.

Clearly management of the motion problem is critical for successful fMRI. This subject is discussed further in Chapter 5.

2.5 SUMMARY

Three major classes of artifacts are found to affect FLASH fMRI experiments. These artifacts are flow-related enhancement, physiological phase variation, and gross motion.

Flow-related enhancement occurs because the magnetization of protons within an imaging slice becomes suppressed by repeated RF pulses during imaging. Fresh protons flowing in from outside the slice appear enhanced by comparison, with enhancement depending on flow velocity. Pulsatile changes in flow velocity cause ghosting in FLASH experiments, and increased noise on vessel-rich cortical surfaces. Flow-related enhancement also reduces specificity of fMRI studies because flow changes are generally less specific to active brain areas than changes in oxygenation.

Movement of the heart and lungs causes small variations (~0.01 ppm) in the strength of the main magnetic field, B0, within the head during imaging. With T2*-weighted imaging, the variations are sufficient to cause large variations in MR signal phase in k-space. These phase variations cause image instability during FLASH fMRI studies.

Motion of the head causes artifactual signal changes during the acquisition of serial MR images. Artifacts are most serious near feature edges.

REFERENCES

1. E. M. Haacke, G. W. Lenz, Improving MR image quality in the presence of motion by using rephasing gradients. *AJR* **148**, 1251 (1987).

2. A. D. Elster, Motion artifact suppression technique (MAST) for cranial MR imaging: superiority over cardiac gating for reducing phase-shift artifacts. *Am. J. Neuroradiol.* **9**, 671 (1988).

3. R. L. Ehman, J. P. Felmlee, Flow artifact reduction in MRI: a review of the roles of gradient moment nulling and spatial presaturation. *Magn. Reson. Med.* **14**, 293 (1990).

4. J.-H. Gao, S. K. Holland, J. C. Gore, NMR signal from flowing nuclei in rapid imaging using gradient echoes. *Med. Phys.* **15**, 819-821 (1988).

5. J.-H. Gao, J. C. Gore, NMR signal from flowing nuclei in rapid gradient echo sequences with refocussing. *Phys. Med. Biol.* **39**, 2305-2318 (1994).

6. W. H. Perman, P. R. Moran, R. A. Moran, M. A. Berstein, Artifacts from pulsatile flow in MRI, *J. Comp. Assist. Tomogr.* **10**, 473 (1986).

7. X. Hu, T. H. Le, T. Parish, P. Erhard, Retrospective estimation and correction of physiological fluctuation in functional MRI. *Magn. Reson. Med.* **34**, 201-212 (1995).

8. K. J. Friston, S. Williams, R. Howard, R. S. J. Frackowiak, R. Turner, Movement-related effects in fMRI time-series. *Magn. Reson. Med.* **35**, 346-355 (1996).

9. C. C. Lee, C. R. Jack, R. C. Grimm, P. J. Rossman, J. P. Felmlee, R. L. Ehman, S. J. Riederer, Real-time adaptive motion correction in functional MRI. *Magn. Reson. Med.* **36**, 436-444 (1996).

10. J. Frahm, K.-D. Merboldt, W. Hanicke, A. Kleinschmidt, H. Boecker, Brain or vein--oxygenation or flow? On signal physiology in functional MRI of human brain activation. *NMR in Biomedicine* **7**, 45-53 (1994).

11. S.-G. Kim, K. Hendrich, X. Hu, H. Merkle, K. Ugurbil, Potential pitfalls of functional MRI using conventional gradient-recalled echo techniques. *NMR in Biomedicine* **7**, 69-74 (1994).

12. J. H. Duyn, C. T. W. Moonen, G. H. van Ypern, R. W. de Boer, P. R. Luyten, Inflow versus deoxyhemoglobin effects in BOLD functional MRI using gradient echoes at 1.5 T. *NMR in Biomedicine* **7**, 83-88 (1994).

13. A. Righini, C. Pierpaoli, A. S. Barnett, E. Waks, J. R. Alger, Blue blood or black blood: R1 effects in gradient-echo echo-planar functional neuroimaging, *Mag. Res. Imag.* **13**, 369-378 (1995).

14. R. D. Frostig, E. E. Lieke, D. Y. Ts'O, A. Grinvald, Cortical functional architecture and local coupling between neuronal activity and the microcirculation revealed by in vivo high-resolution optical imaging of intrinsic signals. *Proc. Natl. Acad. Sci. USA* **87**, 6082-6086 (1990).

15. J. H. Gao, I. Miller, S. Lai, J. Xiong, P. Fox, Quantitative assessement of blood inflow effects in functional MRI signals. *Magn. Reson. Med.* **36**, 314-319 (1996).

16. D. C. Noll, W. Schneider, J. D. Cohen, Artifacts in functional MRI using conventional scanning, *in* "Proc., SMRM, 12th Annual Meeting, New York, 1993," p. 1407.

17. D. C. Noll, W. Schneider, Respiration artifacts in functional brain imaging: Sources of signal variation and compensation strategies, *in* "Proc., SMR, 2nd Annual Meeting, San Francisco, 1994," p. 647.

18. X. Hu, S.-G. Kim, Reduction of physiological noise in functional MRI using navigator echo. *Magn. Reson. Med.* **31**, 495-503 (1994).

19. D. C. Noll, J. O'Brien, Simulation of physiological effects in functional MRI, *in* "Proc., SMR/ESMRMB, Annual Meeting, Nice, 1995," p. 794.

20. G. H. Glover, A. T. Lee, Motion artifacts in fMRI: Comparison of 2DFT with PR and spiral scan methods. *Magn. Reson. Med.* **33**, 624-635 (1995).

21. X. Hu, T. H. Le, T. Parish, P. Erhard, Retrospective estimation and correction of physiological fluctuation in functional MRI. *Magn. Reson. Med.* **34**, 201-212 (1995).

22. T. H. Le, X. Hu, Retrospective estimation and correction of physiological artifacts in fMRI by direct extraction of physiological activity from MR data. *Magn. Reson. Med.* **35**, 290-298 (1996).

23. B. Wowk, M. C. McIntyre, J. K. Saunders, Physiologic artifact correction in fMRI without navigator echoes, *in* "Proc., ISMRM, 4th Annual Meeting, New York, 1996," p. 1822.

24. B. Wowk, M. C. McIntyre, J. K. Saunders, Origin and removal of fMRI physiological noise: a multi-modal approach, *in* "Proc., ISMRM, 5th Annual Meeting, Vancouver, 1997," p. 1690.

25. B. Wowk, M. C. McIntyre, J. K. Saunders, k-Space orthogonalization: A new remedy for fMRI physiological noise, *in* "Proc., ISMRM, 5th Annual Meeting, Vancouver, 1997," p. 351.

26. B. Wowk, M. C. McIntyre, J. K. Saunders, k-space detection and correction of physiological artifacts in fMRI. *Magn. Reson. Med.* **38**, in press (1997).

27. J. F. Schenck, Review article: Role of magnetic susceptibility in MRI. *Med. Phys.* **23**, 815-850 (1996).

28. A. C. Guyton, *in* "Textbook of Medical Physiology" Saunders, Philadelphia, 1986.

29. W. Huda, R. Slone, *in* "Review of Radiologic Physics" Williams and Wilkins, Media, PA, 1995.

30. J. V. Hajnal, R. Myers, A. Oatridge, J. E. Schwieso, I. R. Young, G. M. Bydder, Artifacts due to stimulus correlated motion in functional imaging of the brain. *Magn. Reson. Med.* **31**, 283-291 (1994).

31. J. V. Hajnal, Functional neuroimaging artifacts, in "Encylopedia of Nuclear Magnetic Resonance" (D. M. Grant, R. K. Harris, Eds.) p. 2144-2153, John Wiley & Sons (1996).

32. J. J. Sychra, D. G. Pavel, Y. Chen, A. Jani, The accuracy of SPECT brain activation images: Propagation of registration errors. *Med. Phys.* **21**, 1927-1932 (1994).

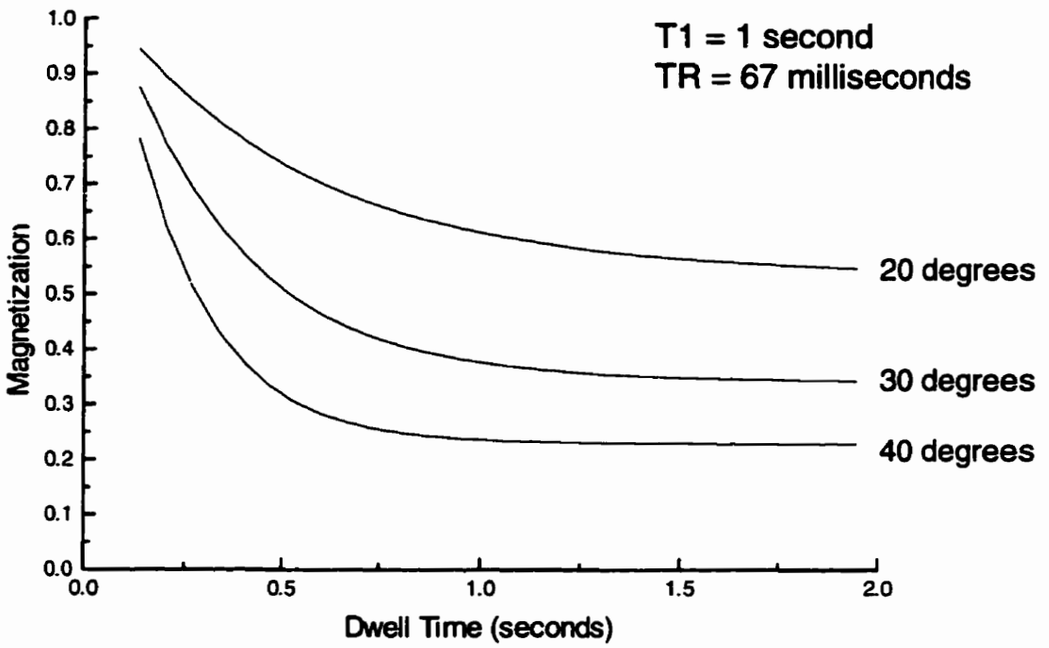

FIG. 2.1 Suppression of longitudinal magnetization at various RF flip angles as a function of dwell time (exposure time) within an excited volume. Spins within an imaging slice rapidly equilibrate to a new, suppressed level of magnetization during imaging.

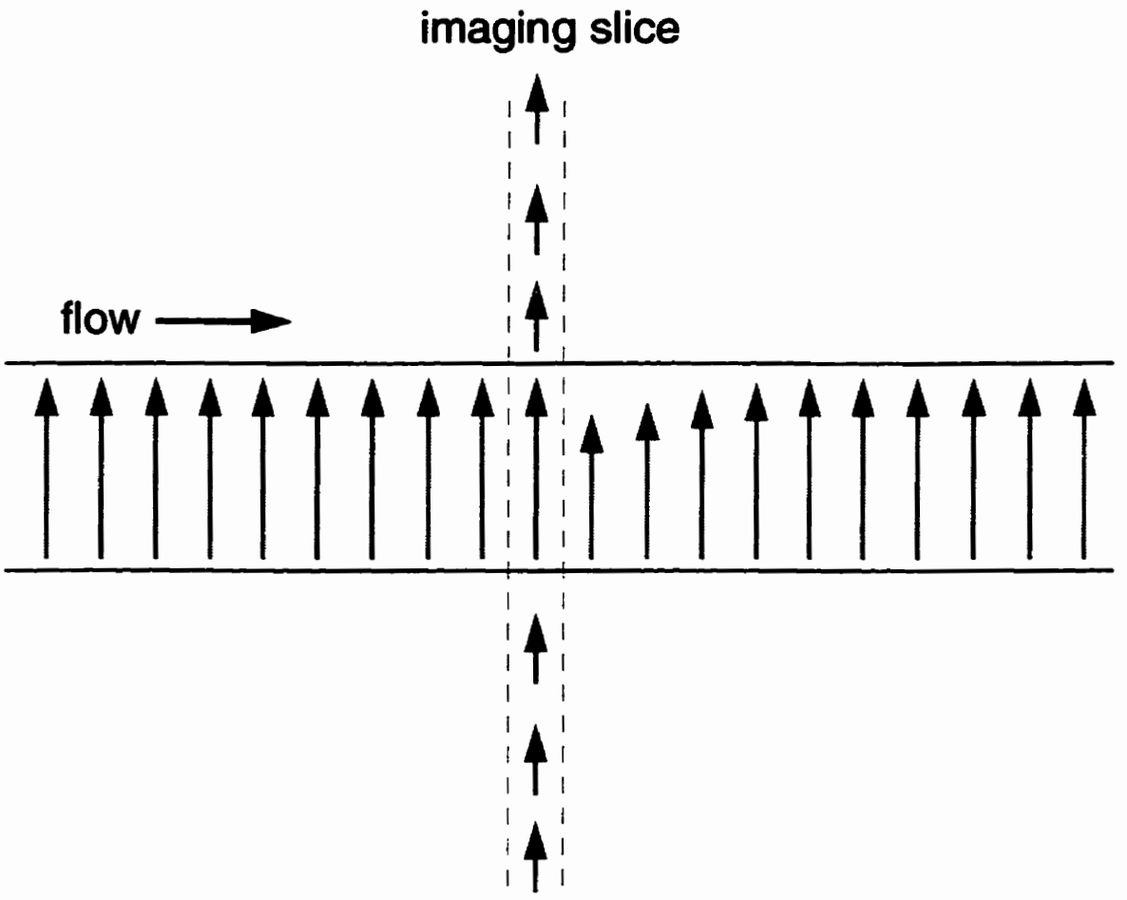

FIG. 2.2 Mechanism of inflow enhancement. The longitudinal magnetization of spins inside the slice being imaged becomes suppressed by repetitive RF pulses. Fresh spins flowing in from outside the slice therefore have a greater magnetization and stronger signal.

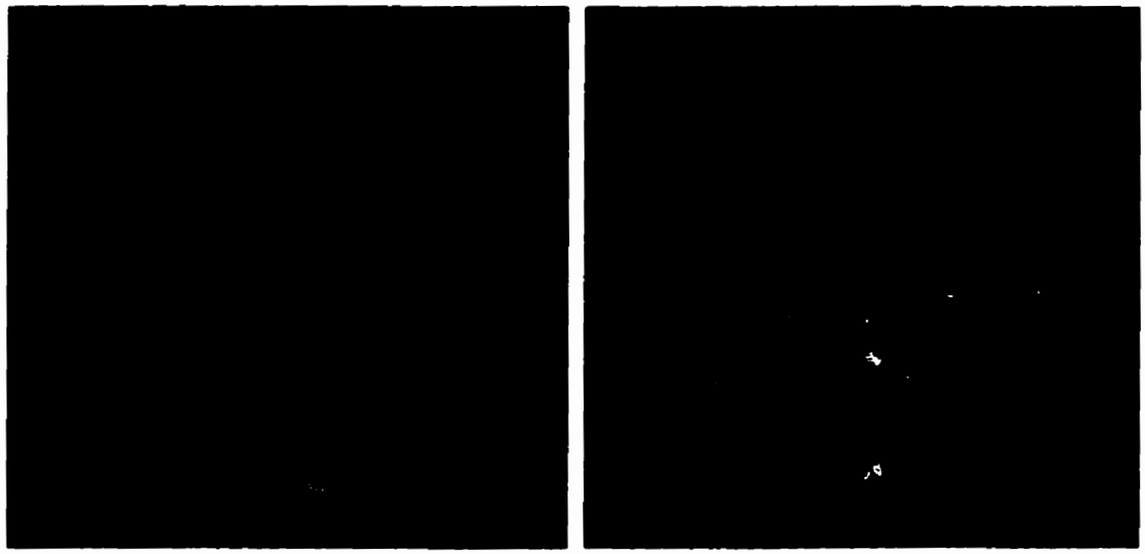

FIG. 2.3 Examples of inflow enhancement. Transverse FLASH images (TR/TE = 67/12 ms, $\alpha = 30°$) obtained at two different slice positions show enhanced intensity of blood in vessels flowing through the slice.

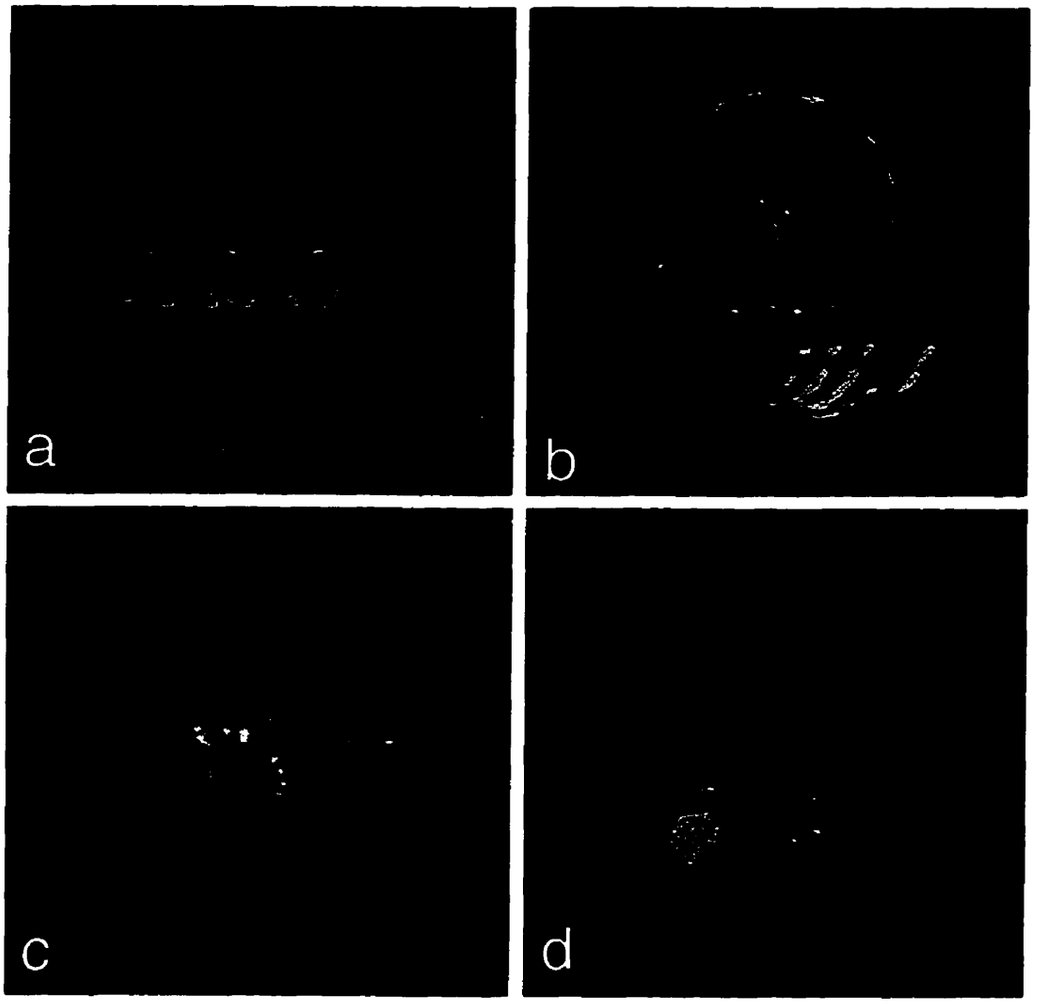

FIG. 2.4 Diverse manifestations of flow-related artifacts. Inflow enhancement and pulsatile ghosting are apparent on time course standard deviation maps due to (a) arterial blood flow, (b) venous blood flow, (c) CSF flow, (d) saccadic movement of the eye. Acquisition parameters were (TR/TE = 74/40 ms, $\alpha = 30°$) for (a,b,d) and (TR/TE = 87/60 ms, $\alpha = 30°$) for (c).

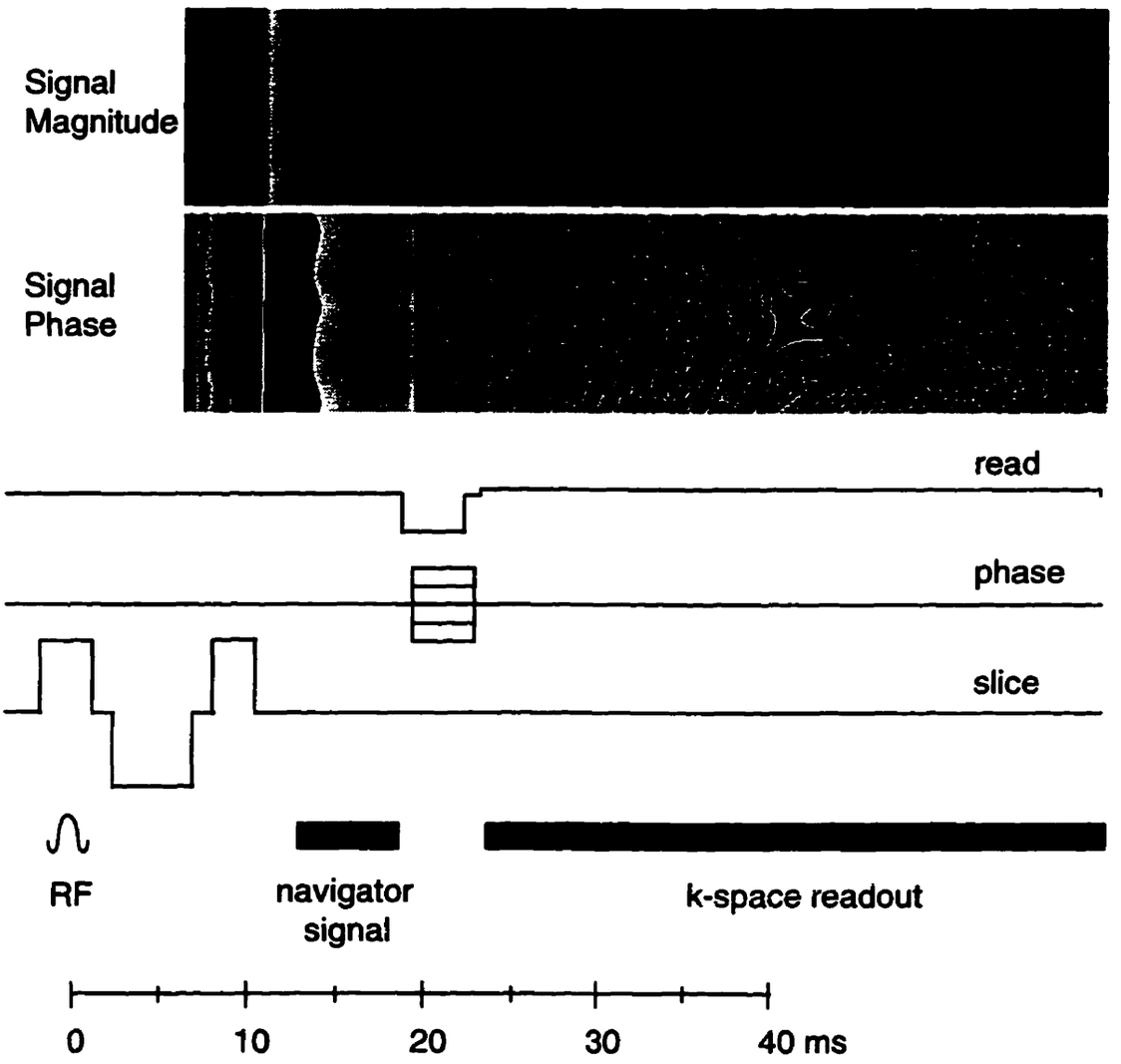

FIG. 2.5 Schematic representation of a single phase encode step in a FLASH imaging sequence. This pattern is repeated with different (stepped) values of the phase encode gradient to readout successive lines of k-space (Fourier space) until data sufficient to reconstruct an image is acquired. The images shown are the magnitude and phase of the signal acquired during successive phase encode steps. In this implementation, the receiver is turned on earlier to allow the acquisition of a "navigator" signal after slice excitation. The phase of the navigator changes between phase encode steps (vertical direction) at a frequency that is characteristic of respiration during the 9 second image acquisition.

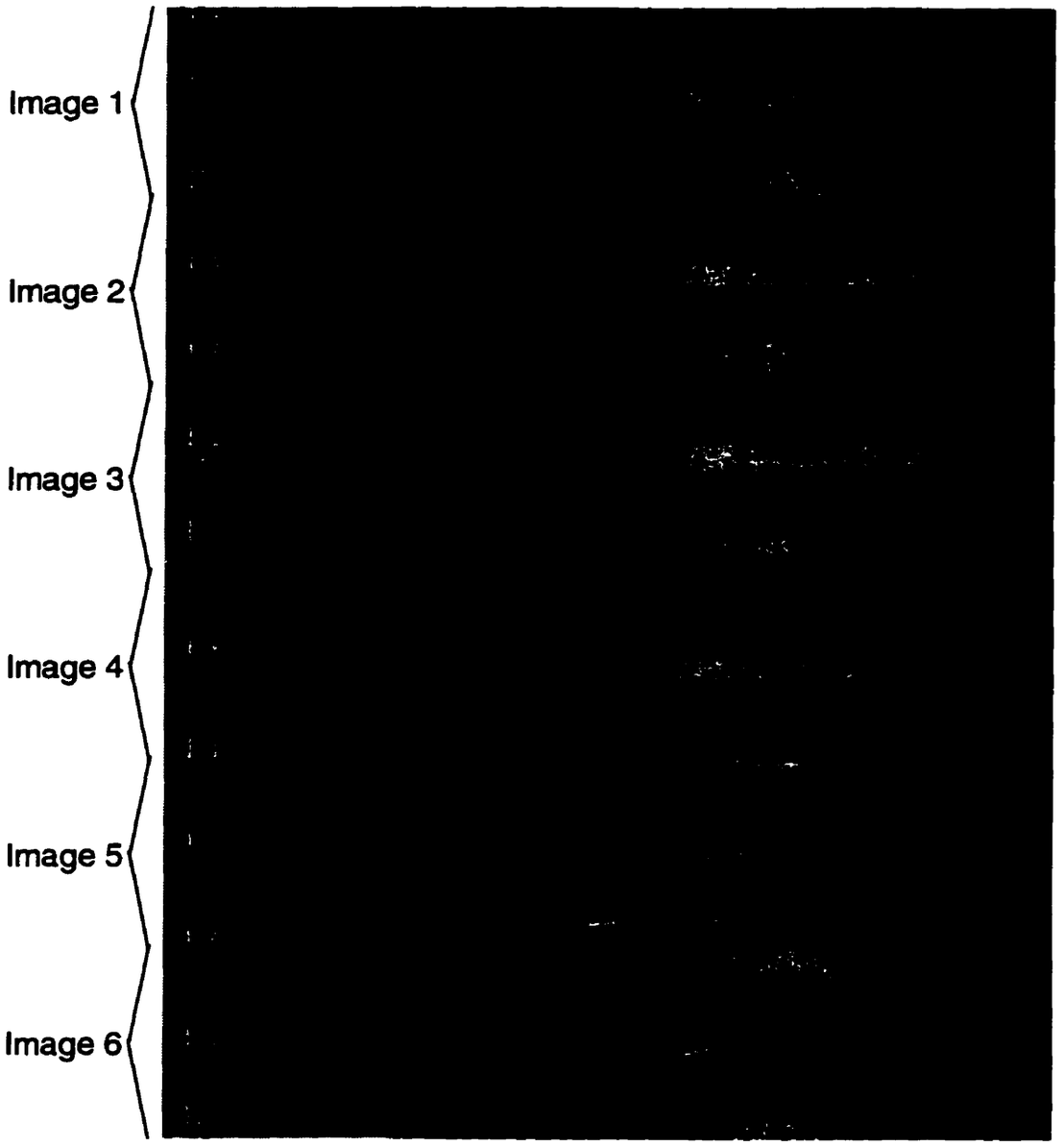

Fig. 2.6 Signal phase variation during acquisition of consecutive images with the FLASH sequence of Fig. 2.5. Areas of low SNR (signal magnitude <1% maximum) are set to black. The phase variation appears global (not obviously affected by phase encoding) and increases with time after slice excitation.

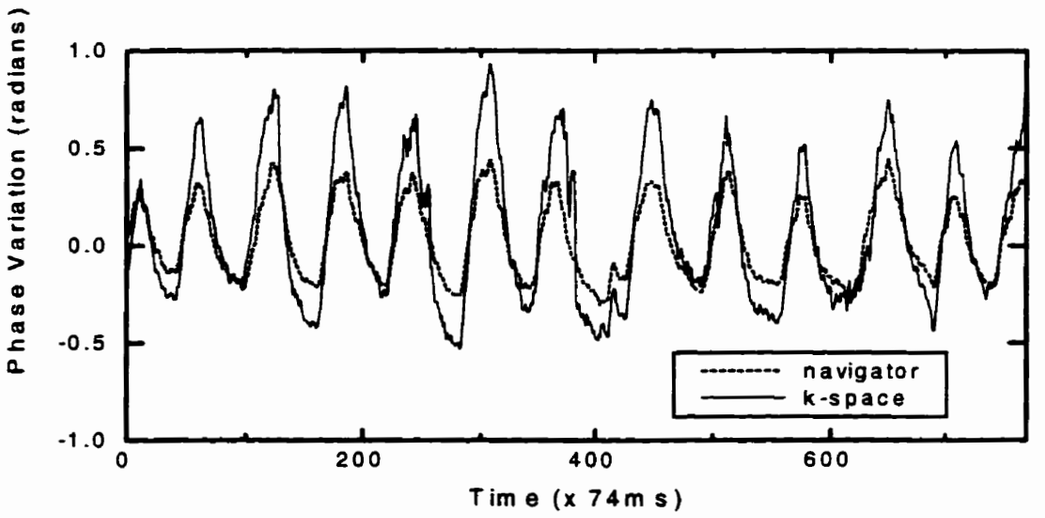

Fig. 2.7 Phase variations during the acquisition of the six images of Fig. 2.6. The k-space plot is mean phase variation over k-space for each phase encode step given by Eq. [2.6]. The variation in k-space is larger than the navigator variation because time-after-slice-excitation (TE) is longer in k-space.

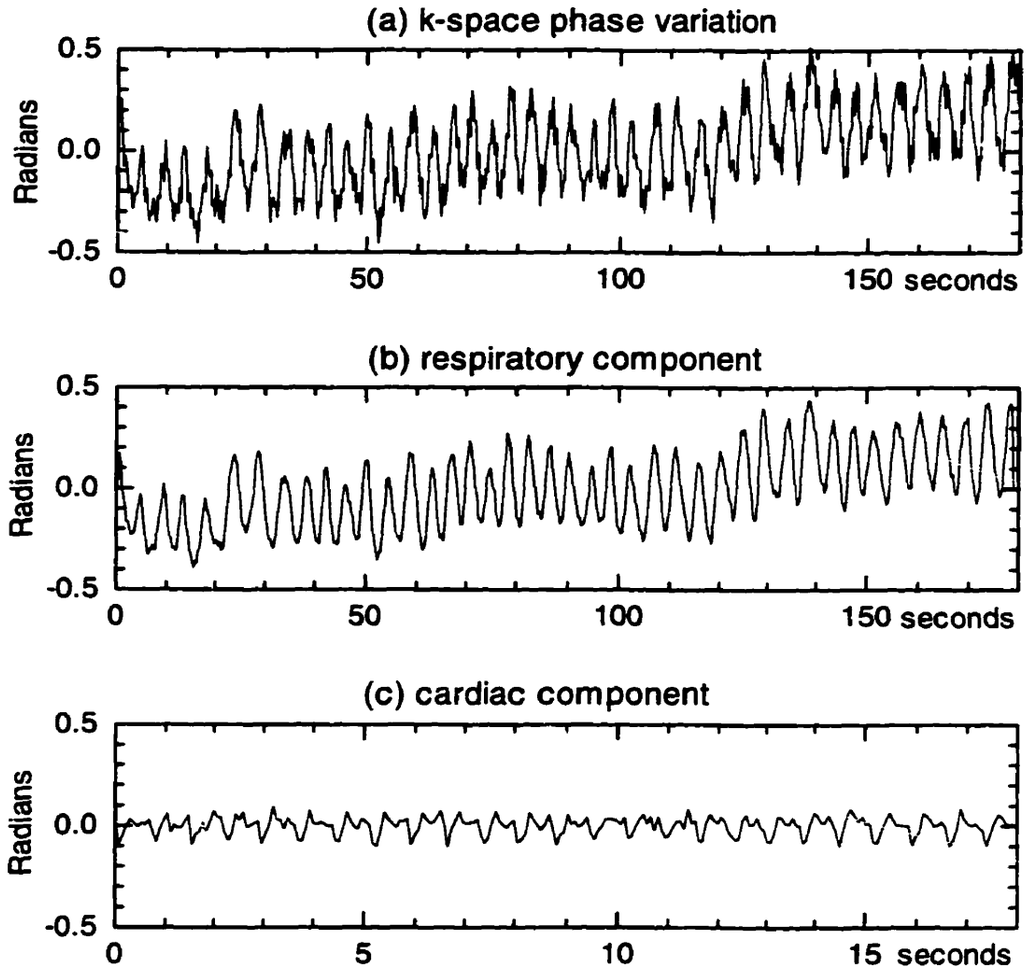

Fig. 2.8 Phase variations during the acquisition of 19 consecutive FLASH images. The apparently noisy plot (a) can be decomposed by low-pass filtering into a respiratory component (b) and a cardiac component (c) (obtained by subtracting (b) from (a)). The time axis of (c) has been magnified to better display the cardiac effects.

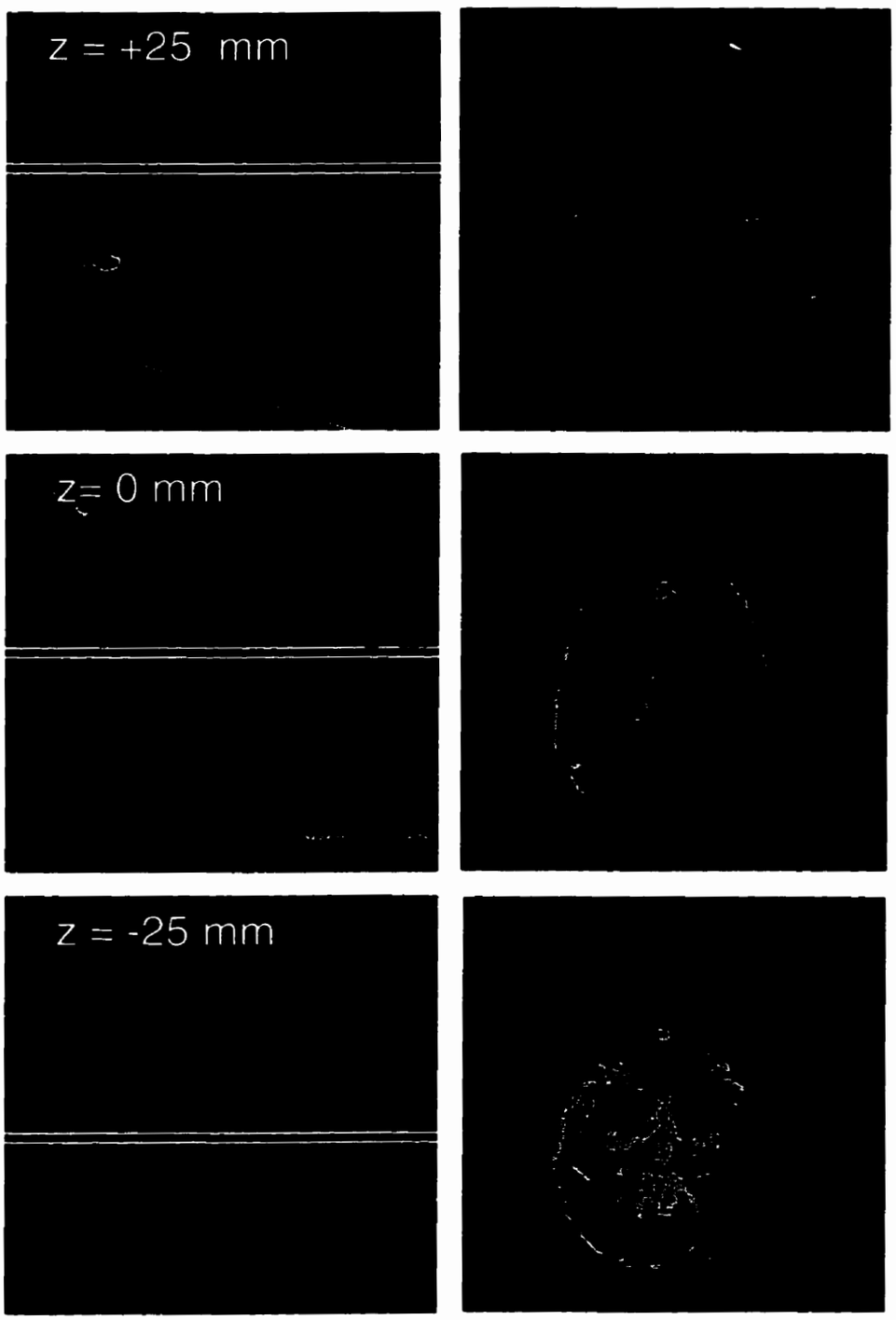

FIG. 2.9 Image noise vs. slice position. Standard deviation maps of consecutive FLASH images (TR/TE = 74/40 ms, $\alpha = 10°$) obtained at three different slice locations. Noise is worst for inferior slices.

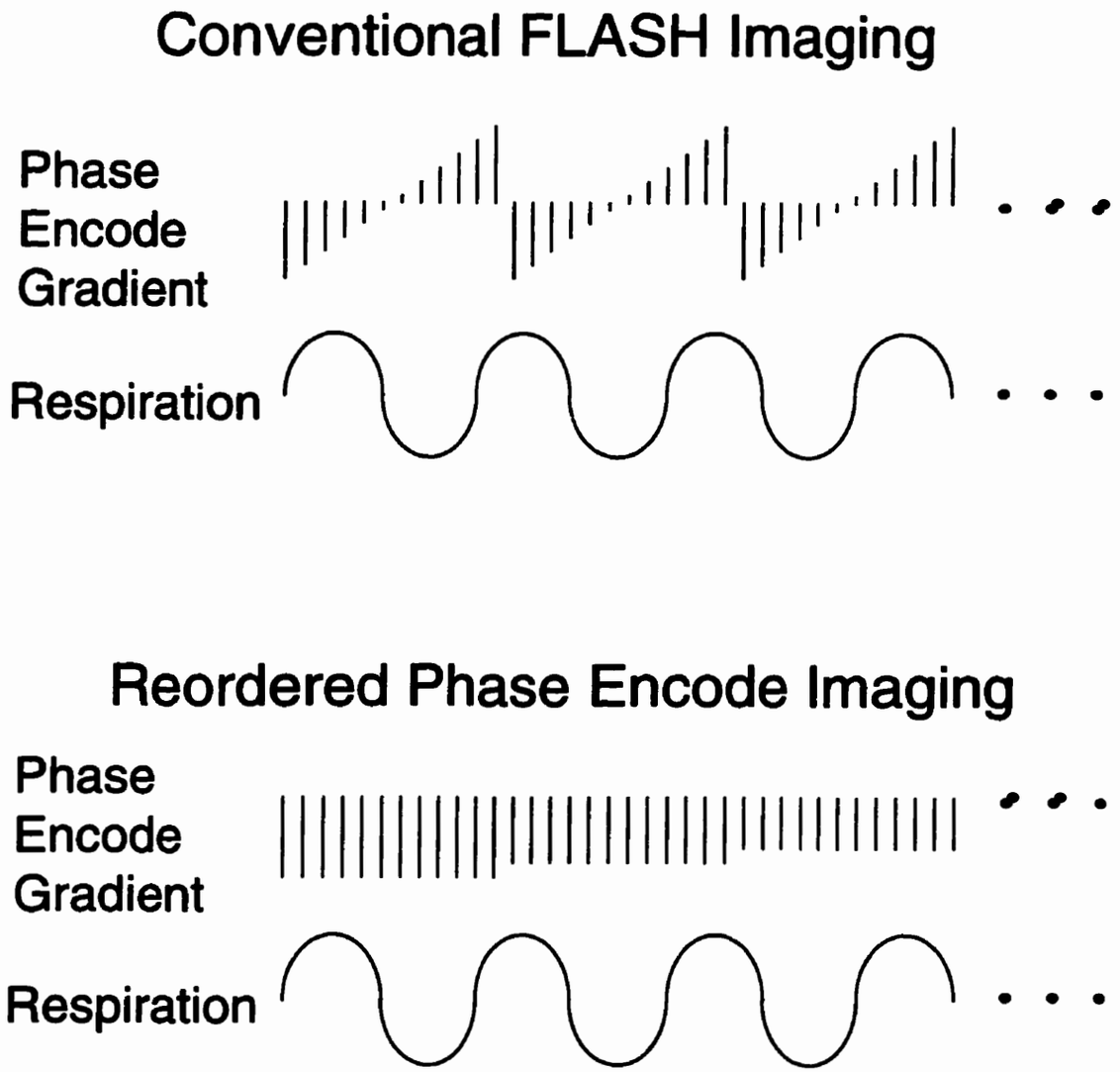

FIG. 2.10 In reordered phase encode imaging, each phase encode step is repeated 100 times so that samples of each step are available at all points in the respiratory cycle. Appropriate samples of each phase encode step can then be used retrospectively to reconstruct images corresponding to any point in the respiratory cycle.

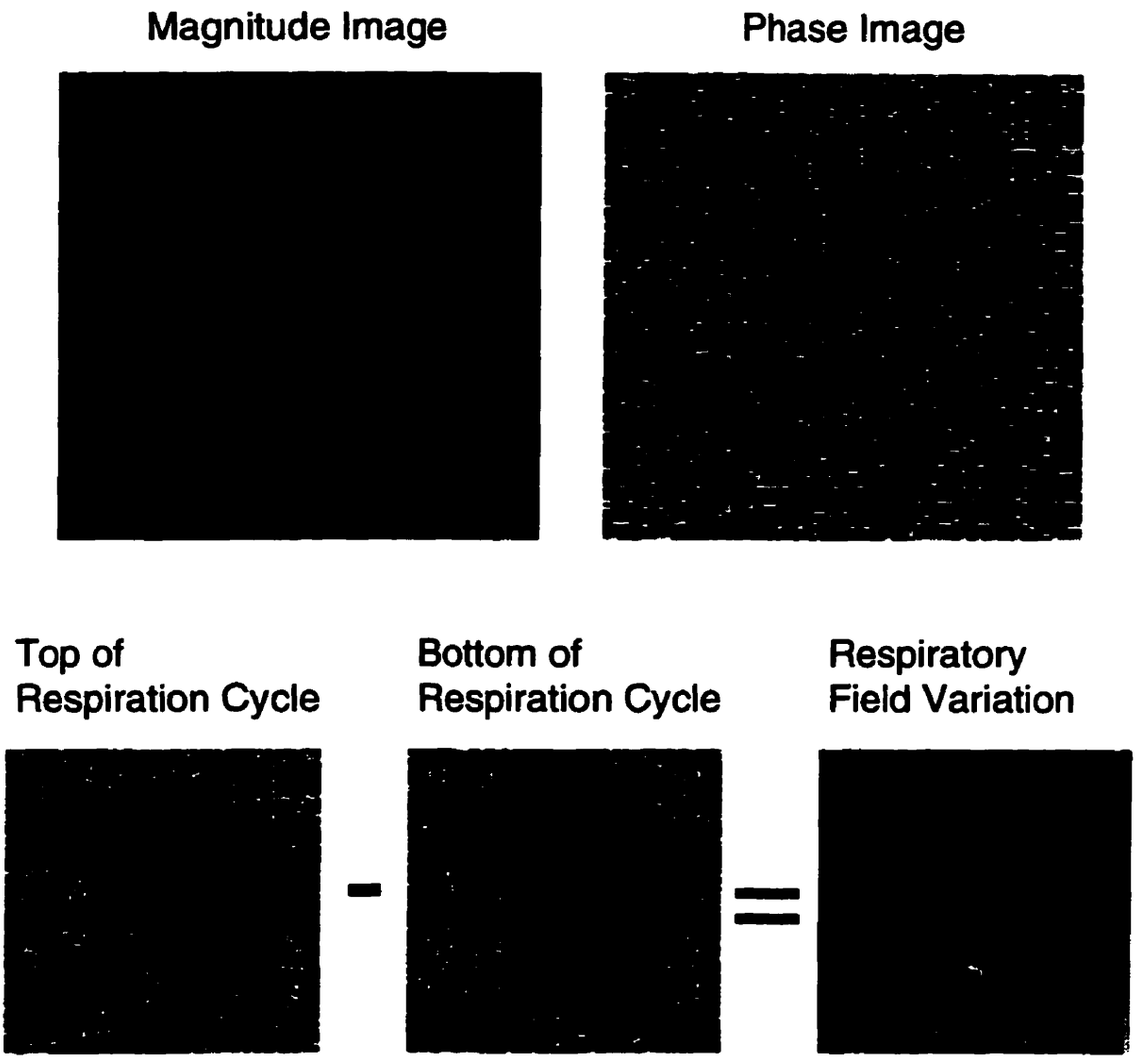

FIG. 2.11 The phase part of MR images (usually discarded) contains information about the resonant frequency, hence field strength, at each point of an image. By acquiring T2*-weighted images with the reordered phase encode method (Fig. 2.10), phase images can be reconstructed corresponding to the top and bottom of the respiratory cycle. The difference between the phase images shows the B0 field variation that occurs with respiration.

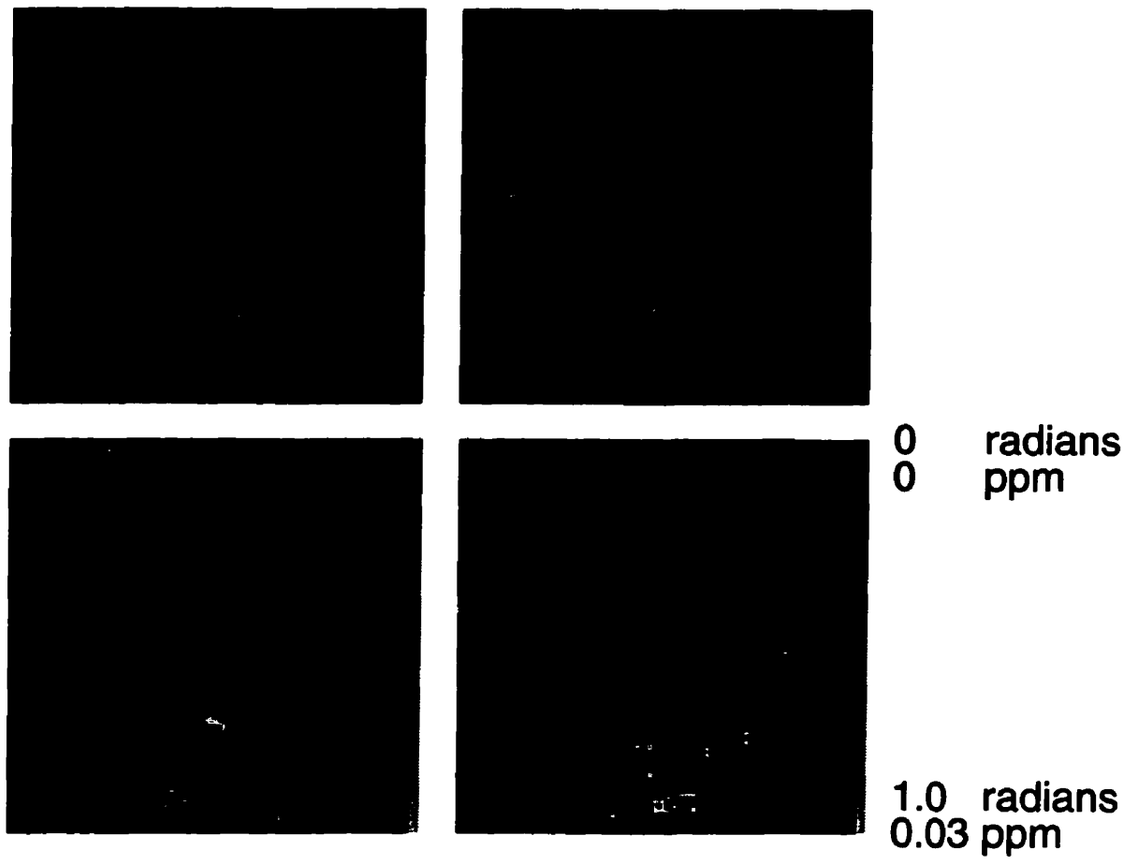

FIG. 2.12 Variation of T2*-weighted image phase (radians) and B0 field strength (ppm) with respiration as determined by the method of Fig. 2.11 for sagittal and coronal slice orientations (TR/TE = 74/40 ms, 64 x 128 matrix, α=10°). The field shift scale is calculated based on the assumption that most image signal is collected near the center of k-space, at time TE=40 ms.

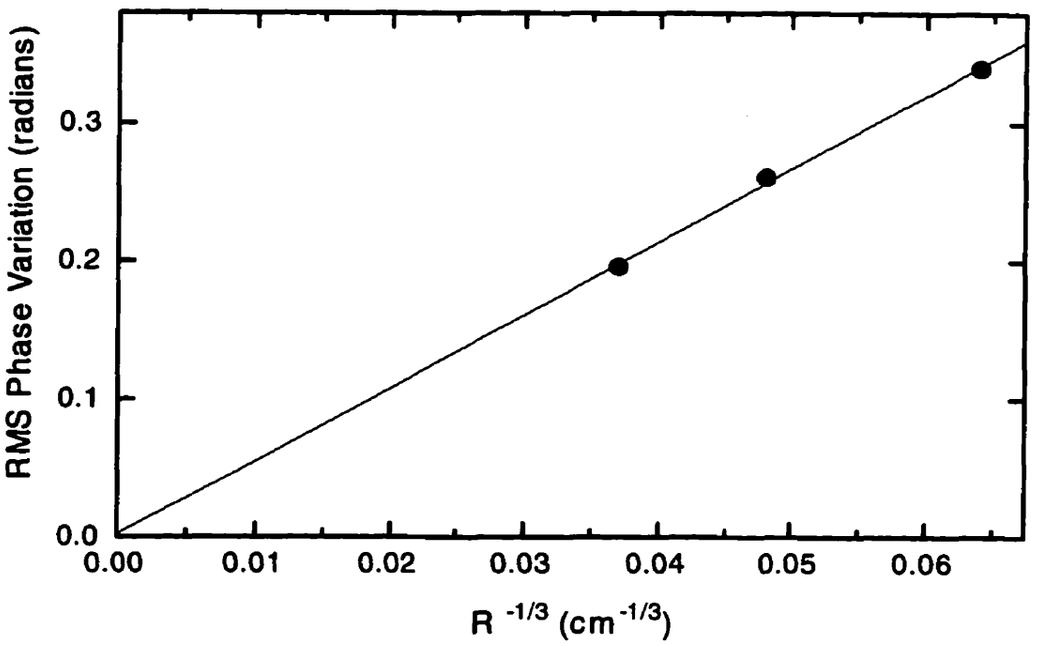

Fig. 2.13 RMS amplitudes of phase variations detected in k-space for the three different slice positions of Fig. 2.9 plotted against the inverse cube root of distance from the chest. (Chest center assumed to be 30 cm below the top slice.) The amplitude varies as the inverse cube of distance from the chest, consistent with a dipolar B0 perturbation located in the chest.

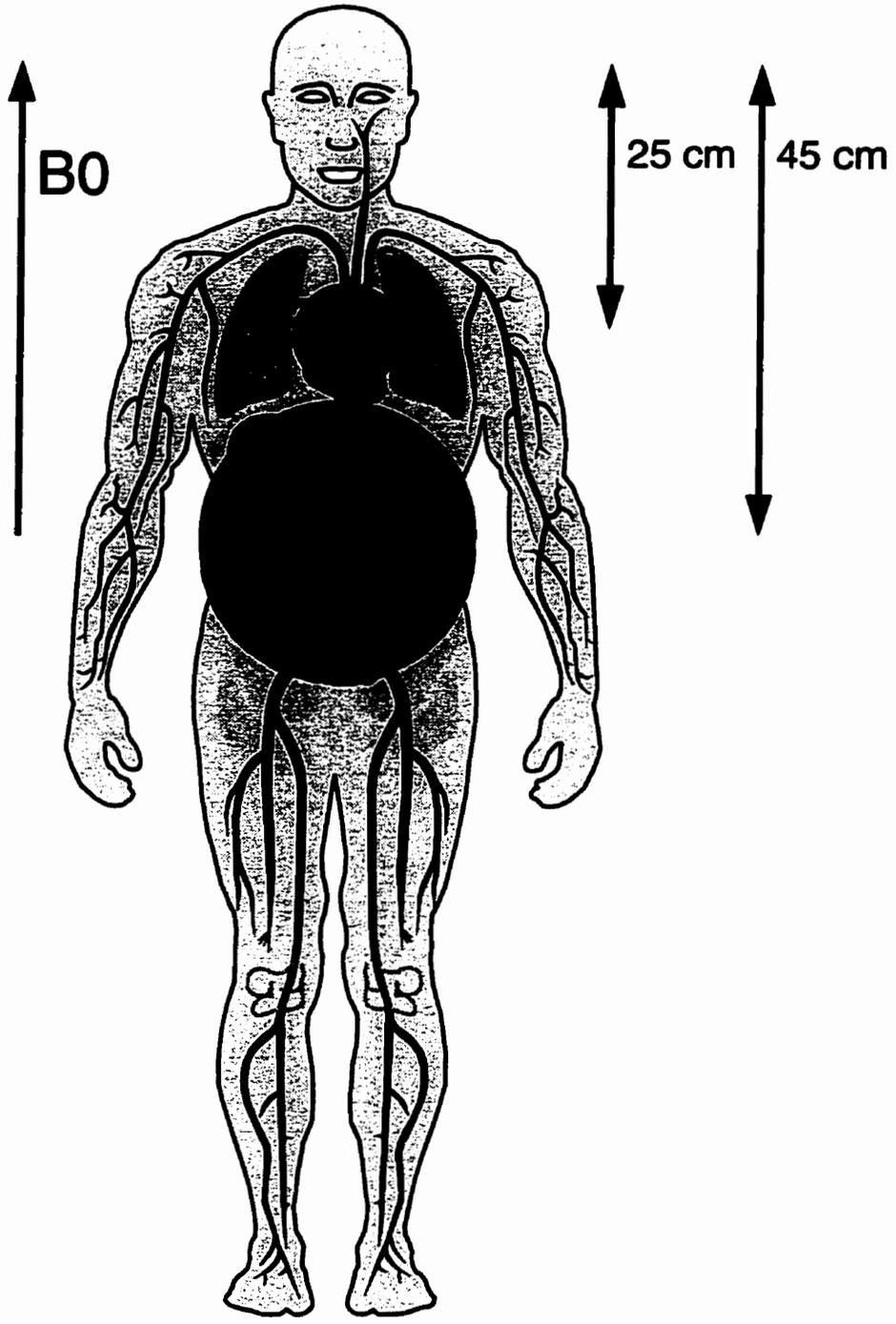

Fig. 2.14 The effect of heartbeat and respiration on the main magnetic field is modeled by considering the heart and abdomen as spherical masses of tissue. The heart expands and contracts as it beats, while the abdomen moves up and down simulating movement of the diaphragm during respiration.

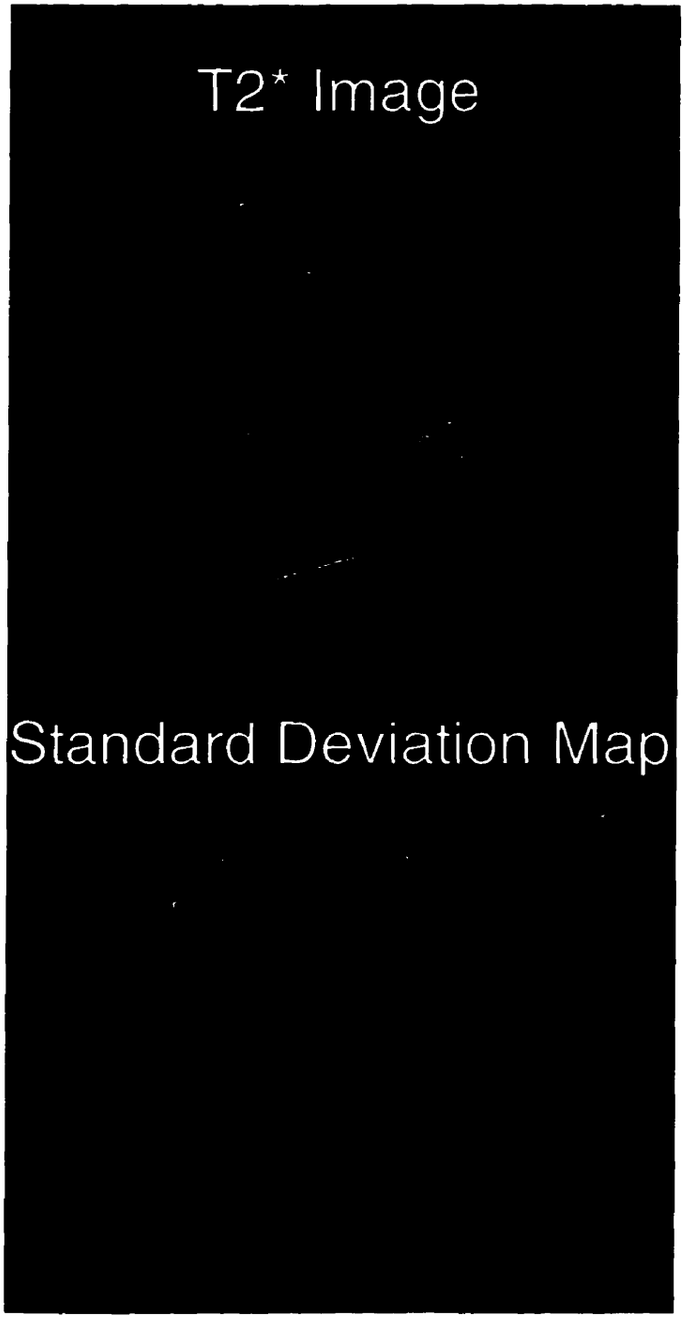

Fig. 2.15 Movement of the head during imaging causes misregistration errors that appear as artifactual signal changes near image edges, as seen on this standard deviation map (lower image) obtained over a time course of 60 images (ten minutes).

Chapter 3

FLOW ARTIFACT SUPPRESSION

3.1 INTRODUCTION

Blood oxygen level dependent (BOLD) contrast for fMRI is typically achieved by T2*-weighted gradient echo sequences that are sensitive to magnetic susceptibility changes associated with changes in blood oxygenation (BOLD effect). However, these same sequences can also be sensitive to changes in blood flow (inflow effect) (1-3). Flow sensitivity is an issue for any 2D sequence, such as FLASH or short-TR EPI which significantly suppresses longitudinal magnetization.

There is a need for flow-insensitive BOLD imaging for both theoretical and practical reasons. From a theoretical viewpoint, BOLD imaging with inflow effects is not true BOLD imaging. The absence of pure BOLD imaging with high temporal and spatial resolution is a handicap in the study of the mechanism of brain activation. As a practical matter, flow sensitivity is also a source of image noise and artifacts caused by pulsatile flow and bulk motion during fMRI studies. It sensitizes fMRI experiments to activation-related flow changes in large blood vessels that may be distant from sites of true cortical activation.

Various methods have been proposed to reduce or eliminate flow sensitivity from fMRI experiments. Reduced RF flip angles (1) (sometimes combined with centric phase ordering and inter-image delay (2)) are commonly employed (Figs. 3.1,3.2). However SNR is sacrificed, and even low flip angles retain some flow sensitivity at typical

repetition rates. 3D acquisitions (4,5) are inherently flow insensitive, but have poor time resolution and increased sensitivity to motion artifacts. Slice excitation can be performed so that only susceptibility changes generate signal (TRFGE method) (6) , but flow sensitivity will remain in areas of positive signal.

Multiple gradient echoes have been proposed as a means of simultaneously imaging changes in blood flow and T2* independently (7,8). While elegant in principle, the method fails for flow changes that occur on timescales shorter than the imaging time (cardiac pulsation). The method also retains sensitivity to out-of-plane bulk motion ("spin excitation history" effect (9)).

Another solution to the flow problem is to attenuate or remove signal from blood, relying instead upon T2* changes in stationary tissue for the functional signal. This can be achieved by either spatial presaturation (1,3) in which 90° pulses applied to slabs outside the slice null signal of spins flowing into the slice (Fig. 3.3) or diffusion weighting (10,11). Unfortunately these same diffusion weighted studies, and other magnetization transfer contrast (MTC) studies (12) suggest that most of the T2* signal change in BOLD imaging originates in blood, not stationary tissue. Furthermore, diffusion gradients increase sensitivity to bulk motion, and presaturation pulses cause additional signal loss by MTC effects (Fig. 3.4).

In this work a new method (13) of slice excitation is described that removes sensitivity to spin saturation effects. This partial presaturation (PSAT) technique allows 2D slice excitation and imaging while maintaining equilibrium of longitudinal magnetization over a large 3D volume. The technique allows rapid high flip angle imaging without inflow effects, and reduced motion artifacts. With PSAT, slice excitations can be performed at the Ernst angle (which maximizes MR signal) without creating inflow sensitivity.

3.2 PARTIAL PRESATURATION (PSAT)

Conventional presaturation excites spins outside the imaging slice with a 90° flip angle to completely eliminate signal from inflowing spins. An alternative is to excite spins outside the imaging slice with the same flip angle that is used to image the slice (Fig. 3.5). This partial presaturation (PSAT) method eliminates flow-related enhancement without complete loss of blood signal.

The PSAT slice excitation method is shown in Fig. 3.6. An initial weak slice selection gradient of 0.9 mT/m (12% of final strength) is applied. Cos-sinc (cosinusoidally modulated sinc) pulses P3 and P2 excite volumes shown in Fig. 3.7 with the flip angle α. The slice selection gradient is increased to 100%, and cos-sinc pulse P1 excites narrow slabs bounding the imaging slice. Transverse magnetization is then

spoiled, and the final sinc slice excitation α is applied. The result is the excitation of a 2D slice within a large 3D volume that has experienced the same spin excitation history.

All pulses in our current implementation are 3 ms long. The P3, P2, P1 pulses excite slabs of 3000 Hz bandwidth that are centered ±5250 Hz, ±2100 Hz, and ±2800 Hz from the origin respectively. The pulses were created by simply taking the discrete Fourier transform of the desired slab profiles. The slice excitation pulse is a standard 3-lobe sinc that is provided with the Bruker console (approximately 1600 Hz bandwidth). The phase of all pulses is toggled between 0° and 90° between alternate repetitions to minimize transverse coherences.

SAR (specific absorption rate of RF energy) was calculated to be 1.5 W/kg for TR = 65 ms and α = 30°. SAR is minimized by using two slice gradient strengths, which reduces bandwidth requirements for the out-of-slice pulses. (The use of two gradient strengths makes it important that the spectrometer resonant frequency be set correctly so that the PSAT slabs fit together properly.)

In total, PSAT preparation adds an extra 13 ms onto the TR time in this implementation. Some of this time can be recovered by removing spoiler gradients at the end of a FLASH sequence; the PSAT gradients serve as effective spoiler gradients. With sufficient peak RF power, the P2 and P3 pulses can also be combined into single 3 ms pulse without SAR penalty.

A convenient feature of the PSAT sequence is that simply turning off the P1-P3 pulses makes the sequence equivalent to conventional FLASH. The only side effect of turning on the pulses in our implementation is a ~10% signal loss due to magnetization transfer effects. The P1 and α pulses are fitted such that the signal loss due to slice interference effects in water phantoms with PSAT is negligible.

3.3 RESULTS AND DISCUSSION

3.3.1 FLOW INSENSITIVITY

The efficacy of the PSAT method is demonstrated in a flow phantom study in Fig. 3.9 (same phantom as Fig. 3.1). PSAT removes flow enhancement for all but the highest flow rates, for which spins do not dwell long enough in the entry PSAT slab to fully reach equilibrium.

In-vivo efficacy is demonstrated in Fig. 3.10 for a T1-weighted FLASH sequence. Flow enhancement disappears for even the largest vessels.

Fig. 3.11 compares the noise properties of sequential T2*-weighted FLASH images obtained for two different slice locations with flip angles α =30°, 10°, and 30° with PSAT. High flip angle FLASH images show strong signal fluctuations associated

with blood vessels, especially pial vessels on the surface of the brain. Pulsatile flow artifacts caused by the transverse sinus contaminate a wide area of the left slice. Reducing the flip angle helps considerably, but flow artifacts remain. PSAT excitation with a 30° flip angle appears to remove flow effects completely.

Arterial flow insensitivity is demonstrated in Fig. 3.12(a). A coronal slice shows severe ghosting artifacts caused by the middle cerebral arteries. The ghosting disappears almost completely with PSAT, showing that PSAT can suppress flow artifacts caused by even the most rapidly flowing blood in the brain. The success of PSAT in suppressing flow ghosts suggests that flow ghosts in FLASH imaging are caused predominantly by pulsatile inflow, and that phase effects are negligible when first-order flow compensation is used.

Fig. 3.12(b) shows that CSF flow noise in ventricles is also reduced by PSAT. This is an important benefit because pulsatile flow of CSF can ghost into cortical areas of interest in fMRI experiments.

3.3.2 OUT-OF-PLANE MOTION INSENSITIVITY

Spin excitation history has been identified as a source of movement-related artifact in fMRI (9). Small out-of-plane movements during consecutive imaging of a slice can cause signal instability as unsaturated spins from outside the slice move into the

imaging volume. By maintaining spins over a large volume in an equally-saturated state, the PSAT technique is ideally immune to this artifact.

Fig. 3.12(c) shows PSAT reduction of signal fluctuations and image artifacts caused by movement of the eye during imaging. This effect was observed with multiple subjects. Further optimization of the fit between the α and P1 slice profiles (Fig. 3.7) should further improve the insensitivity of the PSAT method to small out-of-plane movements.

3.3.3 IN-PLANE MOTION INSENSITIVITY

In-plane motion has been identified as a major source of artifacts in fMRI (14). Although image registration helps mitigate these artifacts, it is also beneficial to generate images that are inherently less sensitive to motion artifact.

Pure T2*-weighted images of the brain (Fig. 3.13(a)) are dominated by T2 contrast and show strong contrast between grey matter, white matter and CSF. These high-contrast features increase sensitivity to motion artifact, as is seen in Fig. 3.13(c) where Fig. 3.13(a) is digitally rotated by 1° and subtracted from the original image. Contrast can be reduced by adding T1 weighting. PSAT allows T1 weighting to be added by increasing the RF flip angle without adding flow sensitivity. The resulting low-contrast images (Fig. 3.13(b)) are much less prone to motion artifact (Fig. 3.13(d)).

3.3.4 FUNCTIONAL STUDY

The effect of PSAT on an fMRI experiment is demonstrated in a study of the visual cortex. A near-midline sagittal slice was imaged with a FLASH sequence (α=10°, TR/TE =74/40 ms) and then a PSAT-FLASH sequence with α=25°. Stimulation of the primary visual cortex was achieved with light-emitting diode goggles (Grass Instruments, Quincy, MA) flashing alternating red/green colors at 8 Hz. Stimulation was applied in the pattern off/on/off/on/off at 6 image intervals over a total of 30 images. The first image at the beginning of each interval was discarded. Remaining images were processed with a k-space phase correction to reduce physiological noise (15,16) as described in Chapter 4, and then registered to remove in-plane motion artifacts (17) as described in Chapter 5.

Activation maps in Fig. 3.14 are Student's T scores thresholded at the p=0.01 level, with isolated single pixels removed. The primary effects of PSAT are enhanced specificity, and attenuation of "hot spots" apparently associated with flow increases in large vessels. The study confirms that even low flip angle FLASH imaging remains flow-sensitive, resulting in activation patterns that differ from a true BOLD experiment.

3.3.5 OPTIMIZATION OF PSAT PULSES

The object of the PSAT method is to acquire single slice images from a 3D volume of spins with identical suppression of longitudinal magnetization. This objective depends on fitting excitation slabs together so that spins at slab junctions (experiencing excitation from both slabs) suffer the same net suppression as spins in the rest of the PSAT volume. The slice profiling and digital summation method of Figs. 3.6 and 3.7 is not a good measure of success for this objective because suppression of longitudinal magnetization ($1-\cos\theta$) is not a linear function of θ.

The "slice saturation" profiling sequence of Fig. 3.15 was developed to better measure the success of PSAT at achieving uniform 3D magnetization suppression. Rather than imaging the excitation profile of an RF pulse, the slice saturation profiling sequence images the state of longitudinal magnetization within a 3D volume after repeated RF pulsing. It is therefore a true look at the uniformity with which PSAT maintains magnetization within its active volume.

Evaluation of the initial version of the PSAT sequence described in this work by the slice saturation profiling sequence showed that slab fitting was not optimal (Fig. 3.16). The sequence was therefore adjusted in Nov. 1995 by increasing the initial PSAT gradient to 16% of final slice-selective strength, and increasing the P1 pulse bandwidth to 3400 Hz centered at ± 2600 Hz from the slice center. The result is an optimized

saturation profile (last profile, Fig. 3.16) that theoretically offers better immunity to slow flow and out-of-plane motion effects.

3.4 SUMMARY

Blood flow can be a major source of physiological noise and spurious activation in BOLD fMRI experiments. A new method of slice excitation has been developed that removes sensitivity to blood inflow effects. This partial presaturation (PSAT) technique allows imaging of 2D slices within a 3D volume of equally-saturated spins. Inflow enhancement is removed, and sensitivity to out-of-plane motion is reduced. With PSAT, T1 weighting can also be added to T2* images to reduce contrast and sensitivity to in-plane motion artifacts. PSAT is applicable to FLASH, spiral or EPI sequences, allowing for Ernst-angle excitation at high repetition rates without inflow effects, and reduced motion artifacts.

REFERENCES

1. J. Frahm, K.-D. Merboldt, W. Hanicke, A. Kleinschmidt, H. Boecker, Brain or vein--oxygenation or flow? On signal physiology in functional MRI of human brain activation. *NMR in Biomedicine* **7**, 45-53 (1994).

2. S.-G. Kim, K. Hendrich, X. Hu, H. Merkle, K. Ugurbil, Potential pitfalls of functional MRI using conventional gradient-recalled echo techniques. *NMR in Biomedicine* **7**, 69-74 (1994).

3. J. H. Duyn, C. T. W. Moonen, G. H. van Ypern, R. W. de Boer, P. R. Luyten, Inflow versus deoxyhemoglobin effects in BOLD functional MRI using gradient echoes at 1.5 T. *NMR in Biomedicine* **7**, 83-88 (1994).

4. S. Lai, A. L. Hopkins, E. M. Haacke, D. Li, B. A. Wasserman, P. Buckley, L. Friedman, H. Meltzer, P. Hedera, R. Friedland, Identification of vascular structures as a major source of signal contrast in high resolution 2D and 3D functional activation imaging of the motor cortex at 1.5T: preliminary results. *Magn. Reson. Med.* **30**, 387-392 (1993).

5. E. M. Haacke, A. Hopkins, S. Lai, P. Buckley, L. Friedman, H. Meltzer, P. Hedera, R. Friedland, S. Klein, L. Thompson, D. Detterman, J. Tkach, J. S. Lewin, 2D and

Monte Carlo modeling and diffusion-weighted studies in vivo. *Magn. Reson. Med.* **34**, 4-10 (1995).

11. A. W. Song. E. C. Wong, S. G. Tan, J. S. Hyde, Diffusion weighted fMRI at 1.5 T. *Magn. Reson. Med.* **35**, 155-158 (1996).

12. J. W. C. van der Veen, J. A. den Hollander, G. M. Pohost, Human brain activation: perfusion or BOLD effects?, *in* "Proc., SMR, 2nd Annual Meeting, San Francisco, 1994," p. 623.

13. B. Wowk, M. C. McIntyre, A. Hunchak, J. K. Saunders, High flip angle fMRI without inflow effects, *in* "Proc., SMR/ESMRMB, Annual Meeting, Nice, 1995," p. 808.

14. J. V. Hajnal, R. Myers, A. Oatridge, J. E. Schwieso, I. R. Young, G. M. Bydder, Artifacts due to stimulus correlated motion in functional imaging of the brain. *Magn. Reson. Med.* **31**, 283-291 (1994).

15. B. Wowk, M. C. McIntyre, J. K. Saunders, Physiologic artifact correction in fMRI without navigator echoes, *in* "Proc., ISMRM, 4th Annual Meeting, New York, 1996," p. 1822.

16. B. Wowk, M. C. McIntyre, J. K. Saunders, k-space detection and correction of physiological artifacts in fMRI. *Magn. Reson. Med* in press.

17. B. Wowk, M. C. McIntyre, G. Scarth, J. K. Saunders, Image registration for high resolution fMRI: Experience with a Fourier algorithm, *in* "Proc., SMR/ESMRMB, Annual Meeting, Nice, 1995," p. 845.

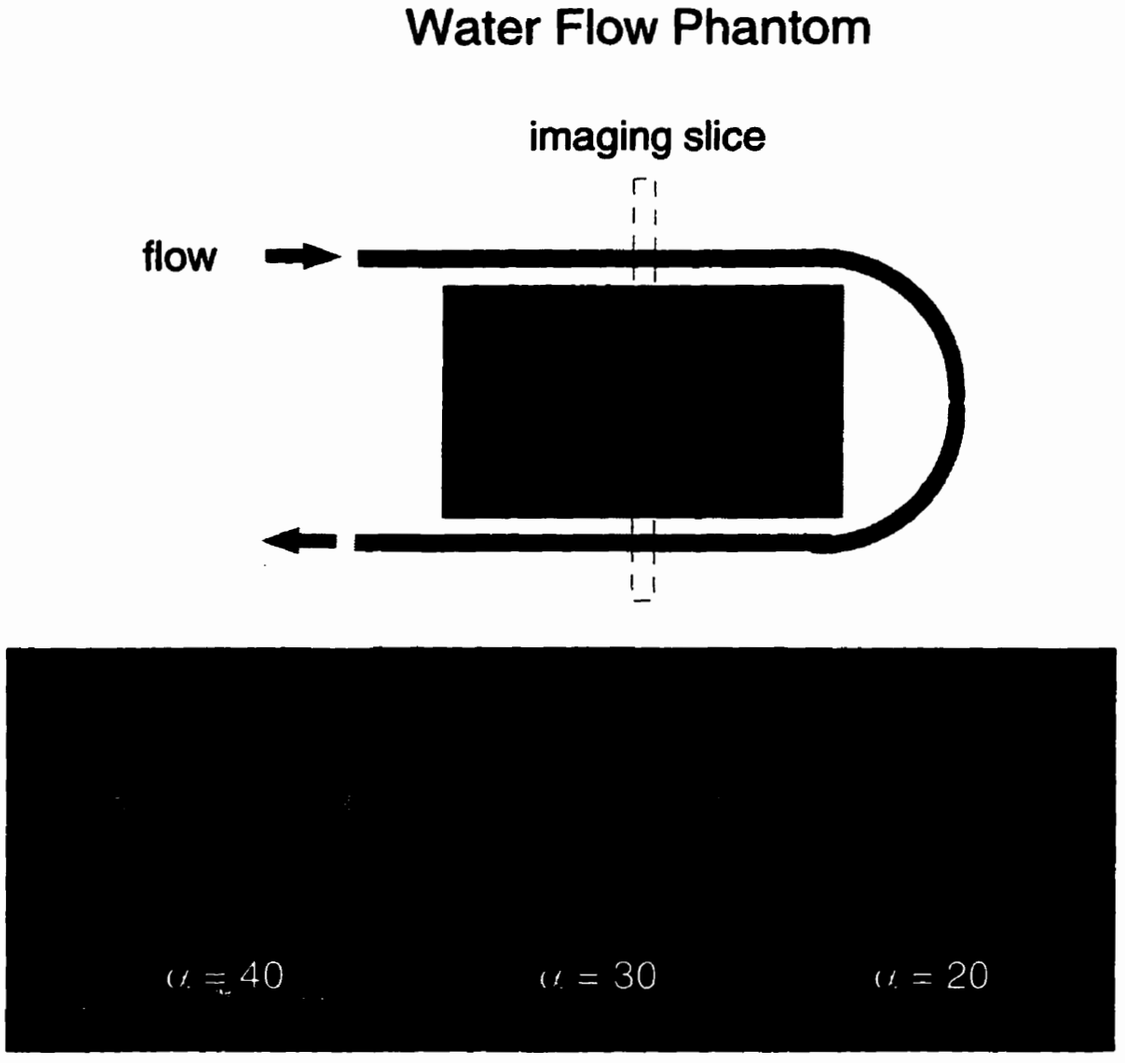

FIG. 3.1 Reduction of inflow enhancement by reduction of RF flip angle. FLASH images (TR/TE =50/12 ms) of a flow phantom with doped water (T1 = 1 sec) flowing at 50 mm/sec.

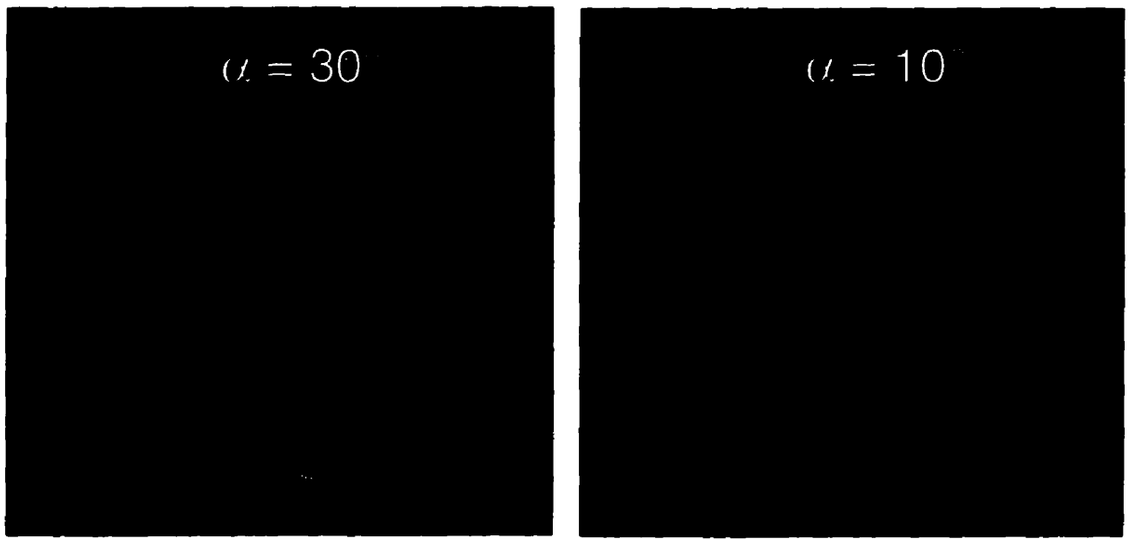

FIG. 3.2 In-vivo demonstration of reduction of inflow enhancement by reduction of RF flip angle. FLASH images (TR/TE =50/12 ms). The disadvantage of reduced flip angle is reduced MR signal (image brightness).

FIG. 3.3 Presaturation methods remove inflow enhancement by preceding the imaging slice excitation by presaturation pulses that excite the volume bounding the slice. In conventional presaturation, a 90° pulse is used to completely suppress magnetization of spins outside the slice. Blood flowing into the slice is then "black", and generates no MR signal.

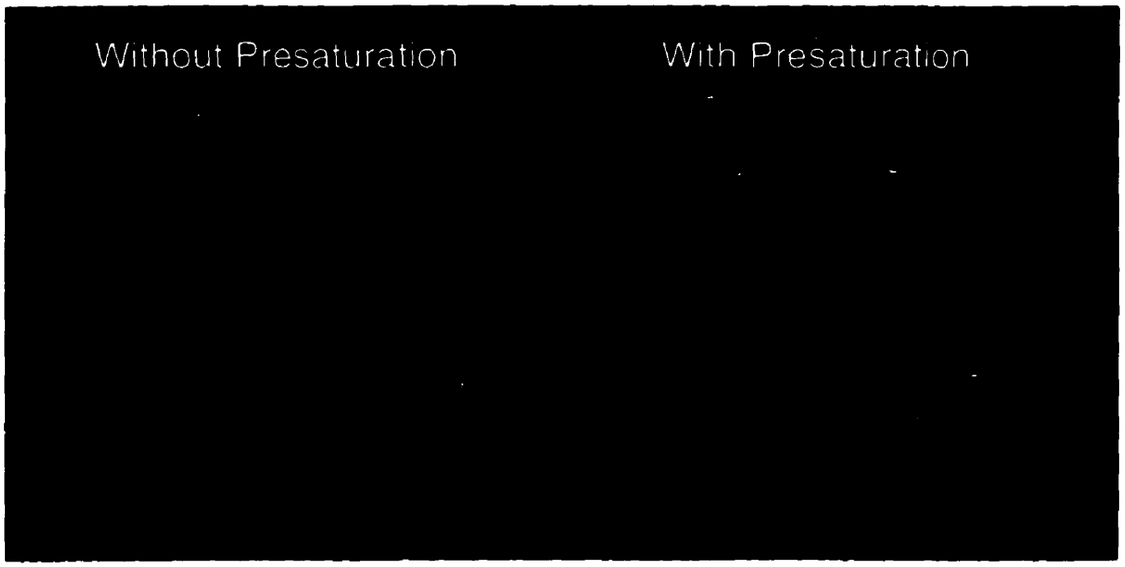

FIG. 3.4 FLASH images (TR/TE = 55/20 ms, $\alpha = 30°$) with and without conventional presaturation of the volume bounding the slice (±45 mm). Presaturation, while eliminating all signal from inflowing blood, causes a 45% signal loss in stationary tissue due to magnetization transfer effects. The MTC origin of the signal loss was confirmed by observing no signal loss when the same pulse sequences were tested on a water phantom.

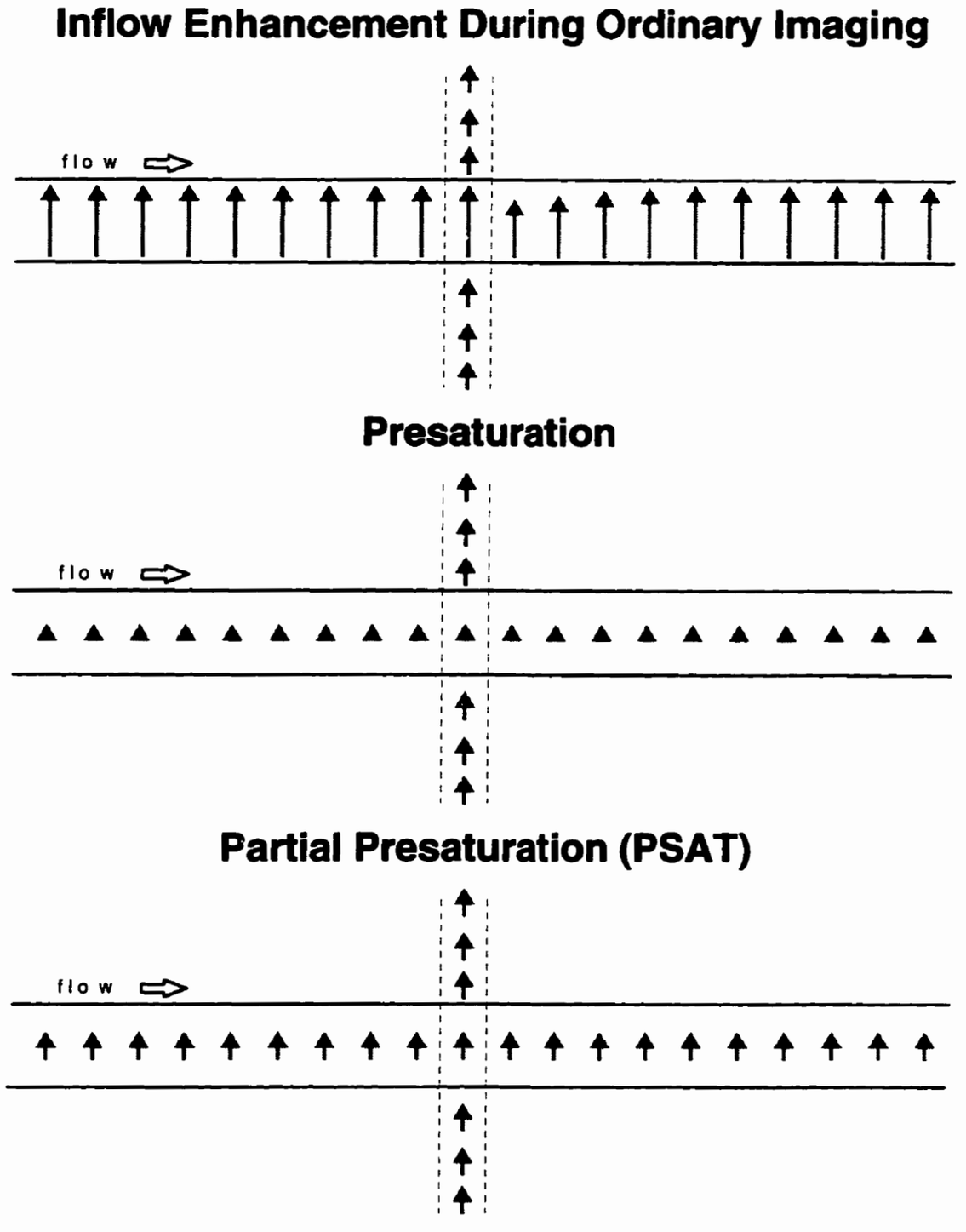

FIG. 3.5 Presaturation strategies. Conventional presaturation eliminates inflow enhancement by nulling signal from spins outside the slice. Partial presaturation eliminates inflow enhancement by bringing spins outside the slice into equilibrium with spins inside.

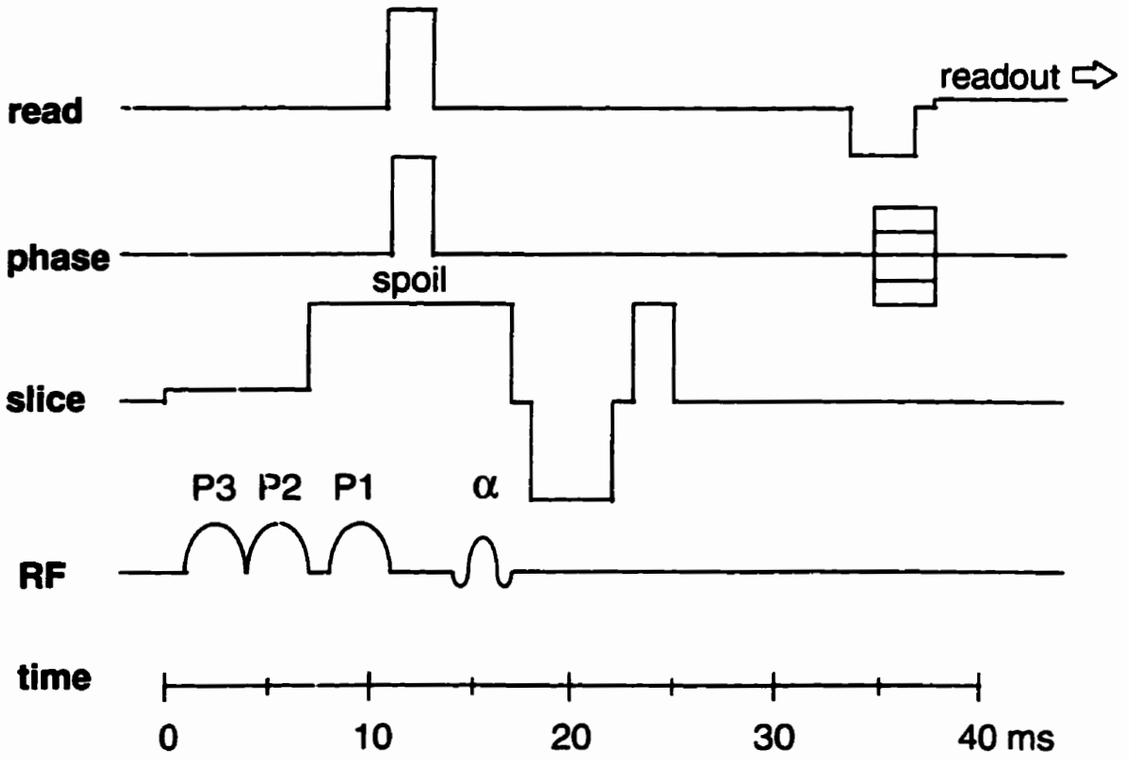

FIG. 3.6 Gradient and RF timing of the PSAT pulse sequence. Cos-sinc pulses P3, P2, P1 excite broad slabs bounding the slice to be imaged as shown in Fig. 3.7. Spoiler gradients remove transverse magnetization prior to slice excitation so that only a 2D image is acquired from the excited volume.

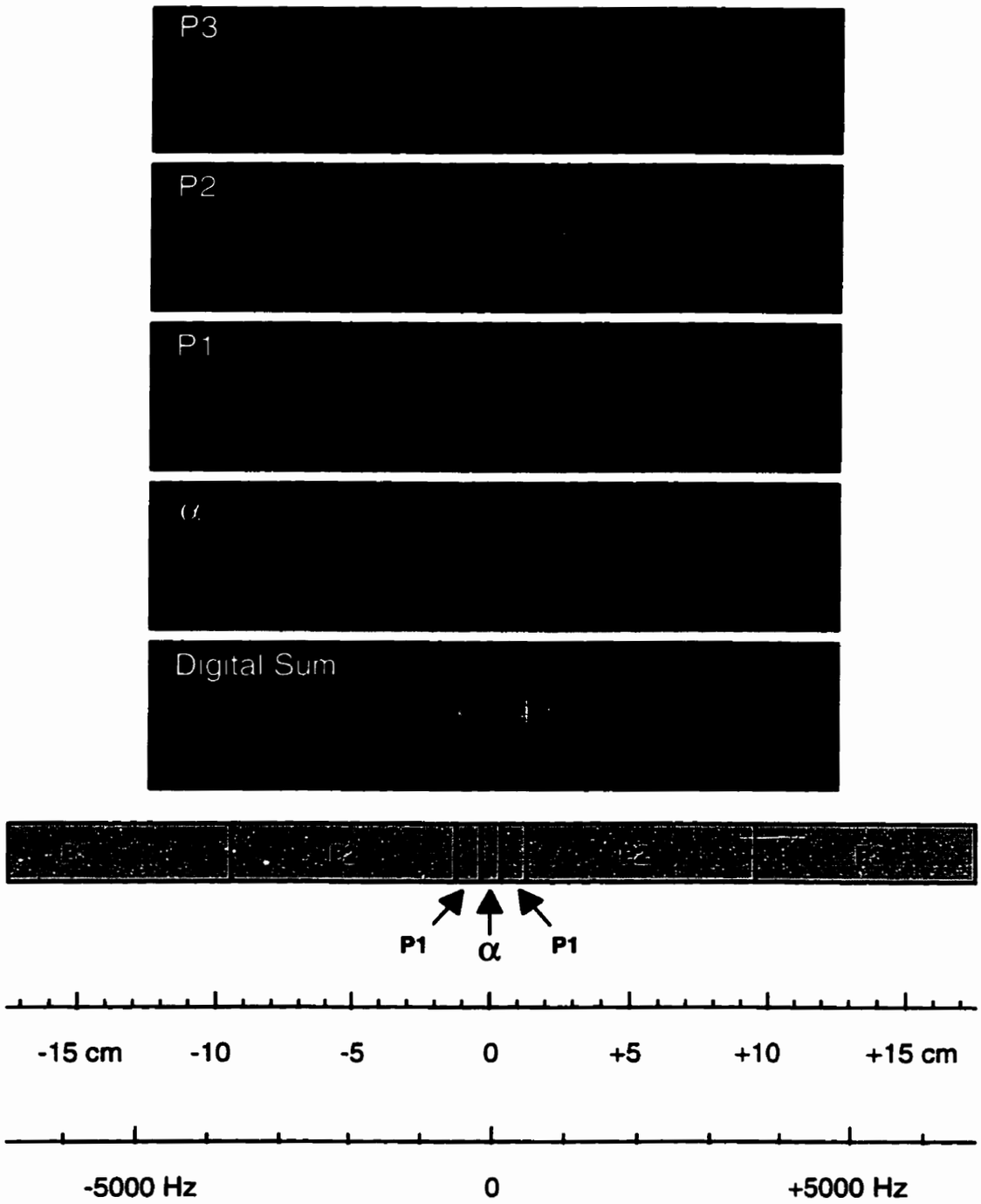

FIG. 3.7 PSAT Spatial coverage of excitation slabs. The images are slice profile images for each of the RF pulses in the PSAT sequence, including the final slice excitation, acquired with the pulse sequence of Fig. 3.8. The frequency scale is for the initial (weak) slice selection gradient, and shows the spectrum of the P3 and P2 pulses.

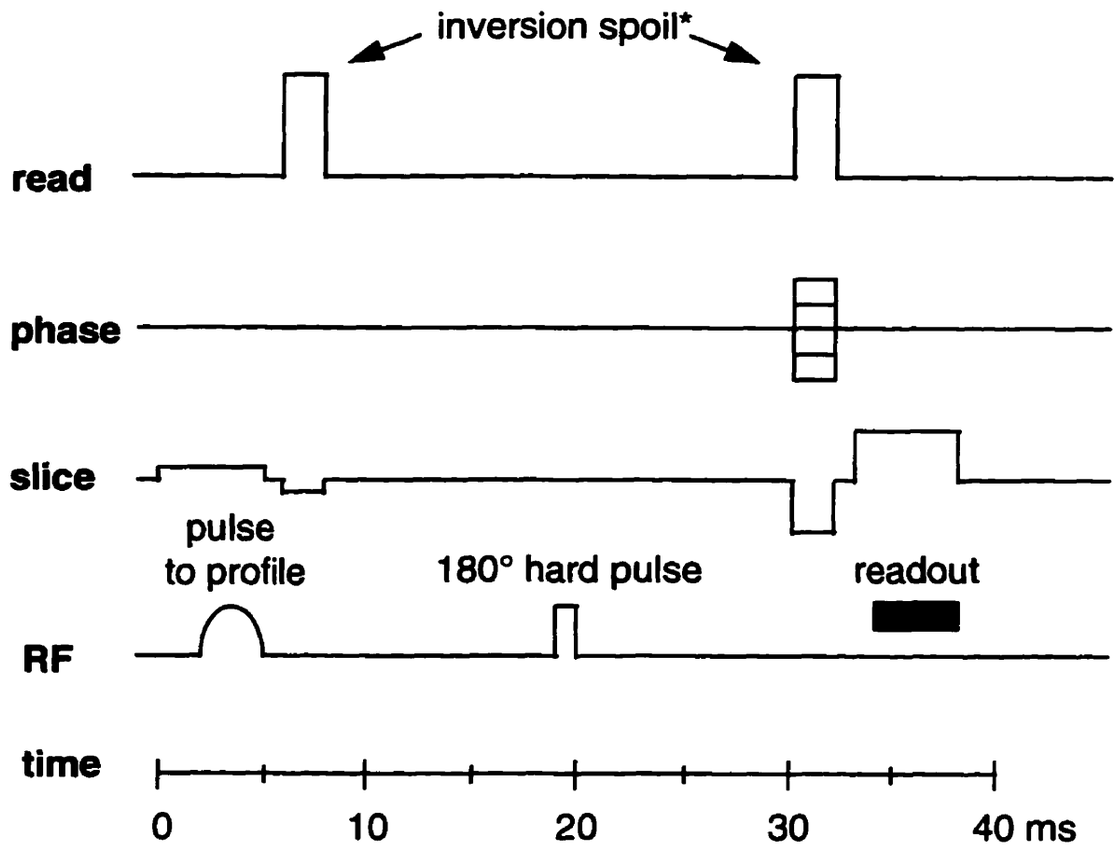

FIG. 3.8 Spin-echo slice profiling sequence. This pulse sequence was developed to acquire the RF pulse profiles of Fig. 3.7 to verify proper fitting of the PSAT excitation slabs. A spin-echo sequence was necessary because gradient echo profiling sequences suffered from signal loss away from the magnet center, where homogeneity is poor. Note that the sequence leaves the magnetization (initially excited by a low flip angle pulse) with a negative longitudinal component, necessitating a long TR (3 seconds) between phase encode steps.

*The inversion spoiling gradients ensure that only spins excited by the first RF pulse appear in the spin echo.

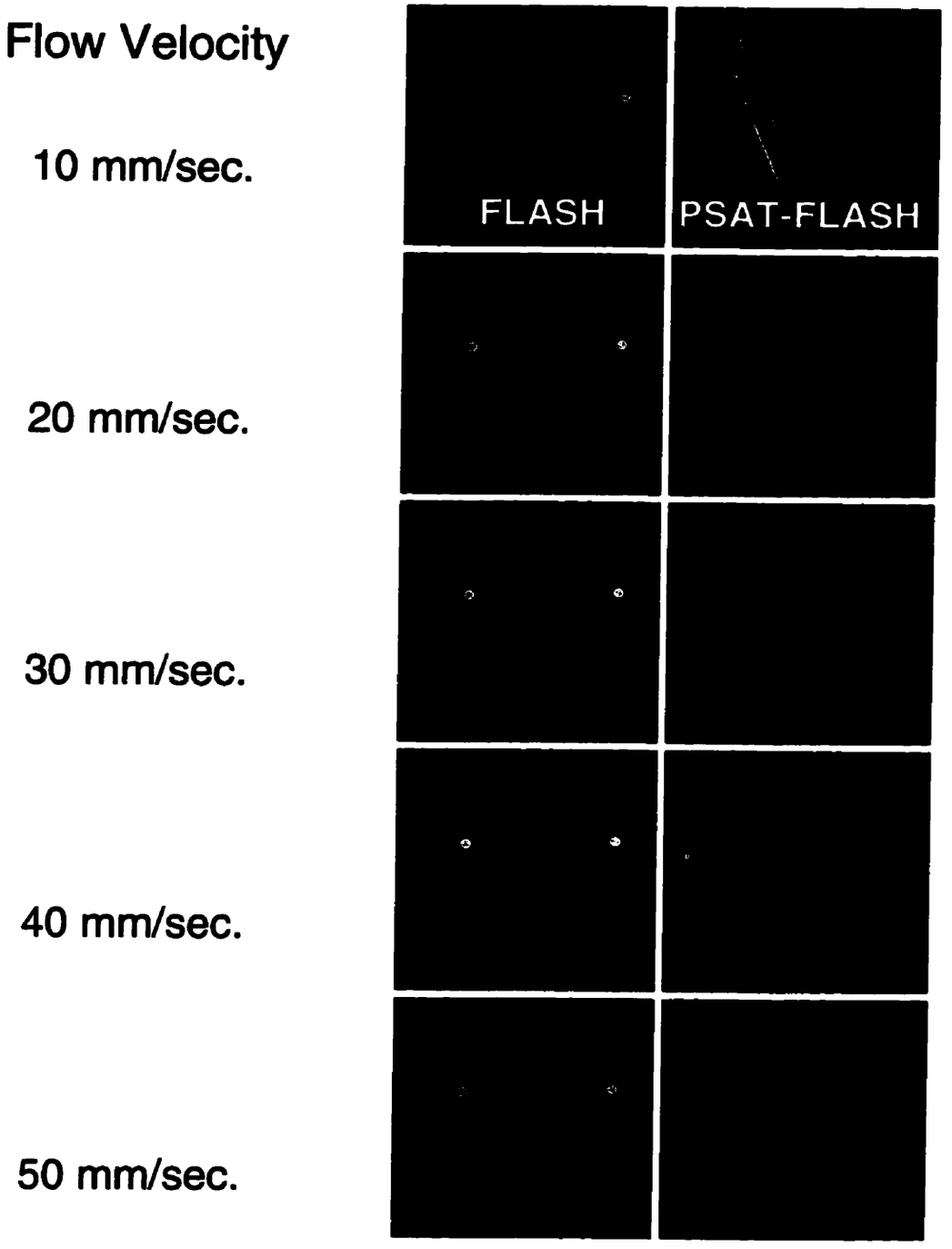

FIG. 3.9 Flow phantom demonstration of inflow suppression with PSAT pulses. FLASH images (TR/TE = 50/12 ms, α = 40°) acquired with and without PSAT slice excitation.

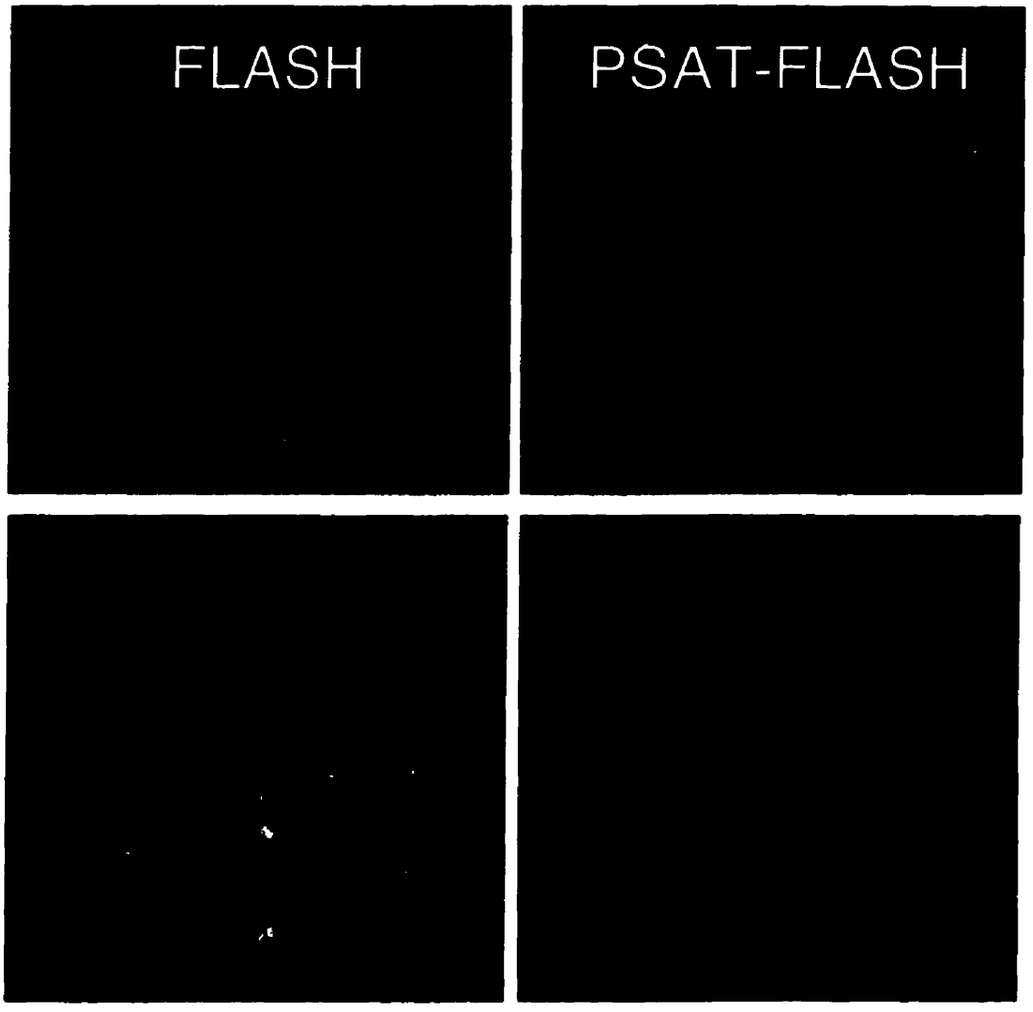

FIG. 3.10 In-vivo demonstration of inflow suppression with PSAT pulses. FLASH images (TR/TE = 67/12 ms, α = 30°) acquired with and without PSAT slice excitation. Inflow effects are removed with almost no loss of image brightness (15% loss to due to MTC effect).

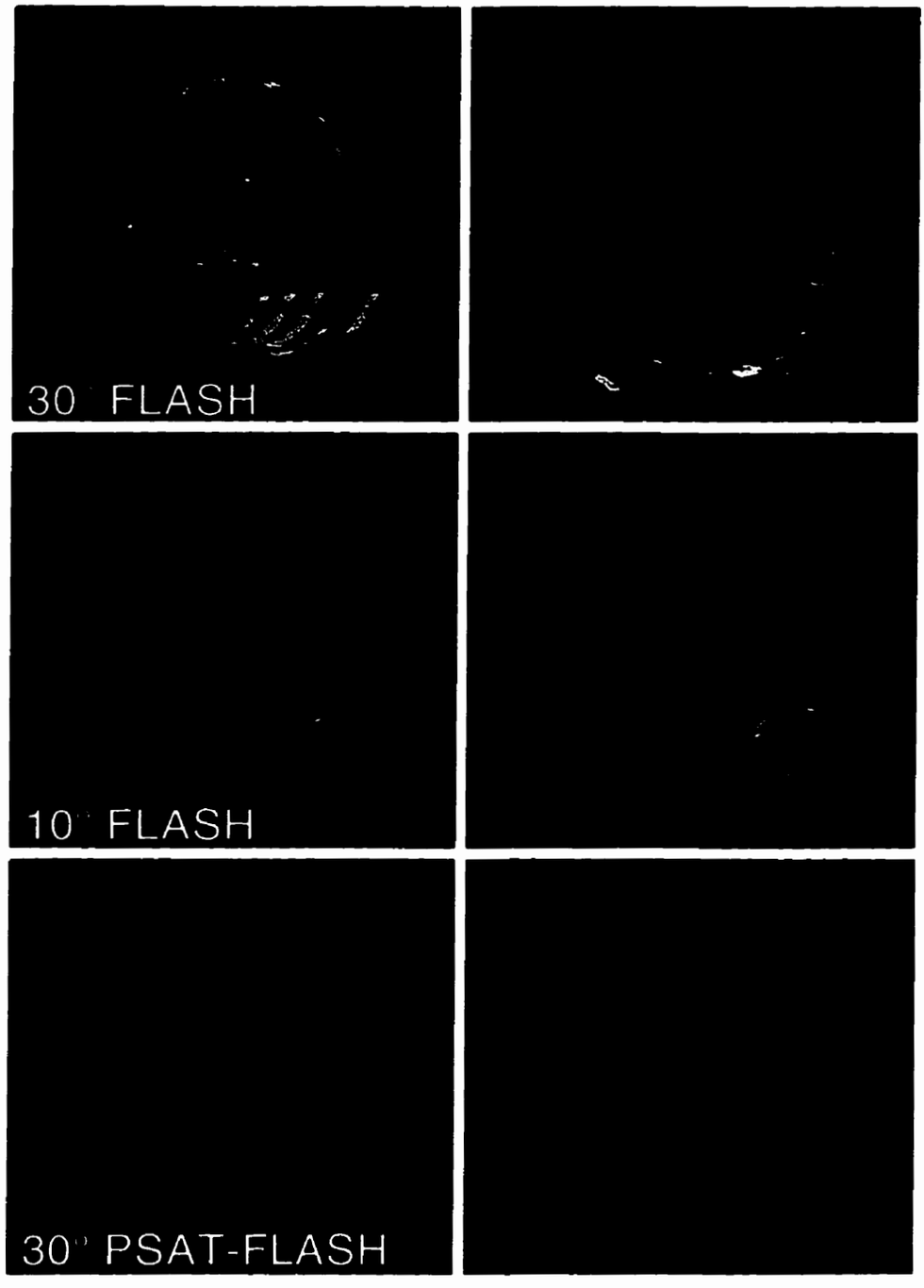

FIG. 3.11 Pixel standard deviation maps obtained over a time course of 25 FLASH images for two different oblique slices (TR/TE = 67/40 ms). Flow-related noise and artifacts that persist even at low flip angles are removed by the PSAT sequence. The prominent ghosting artifact in the left slice is due to pulsatile flow in the transverse sinus.

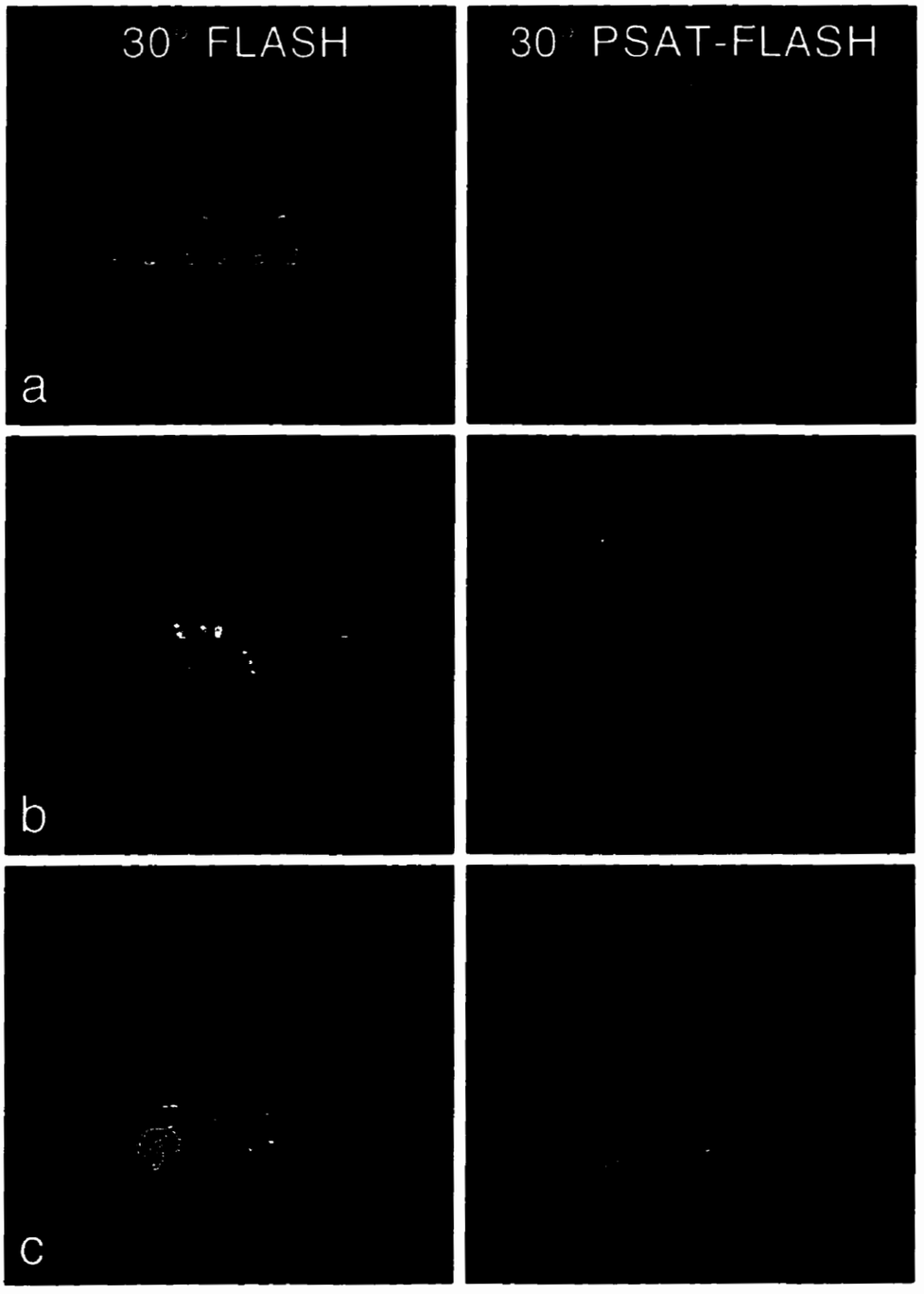

FIG. 3.12 Standard deviation maps showing (a) suppression of arterial flow artifact in a coronal slice, (b) suppression of CSF flow artifact in a transverse slice, (c) suppression of bulk motion artifacts due to saccadic eye movement in an oblique slice. Acquisition parameters were TR/TE =74/40 ms for (a) and (c), and TR/TE =87/60 ms for (b).

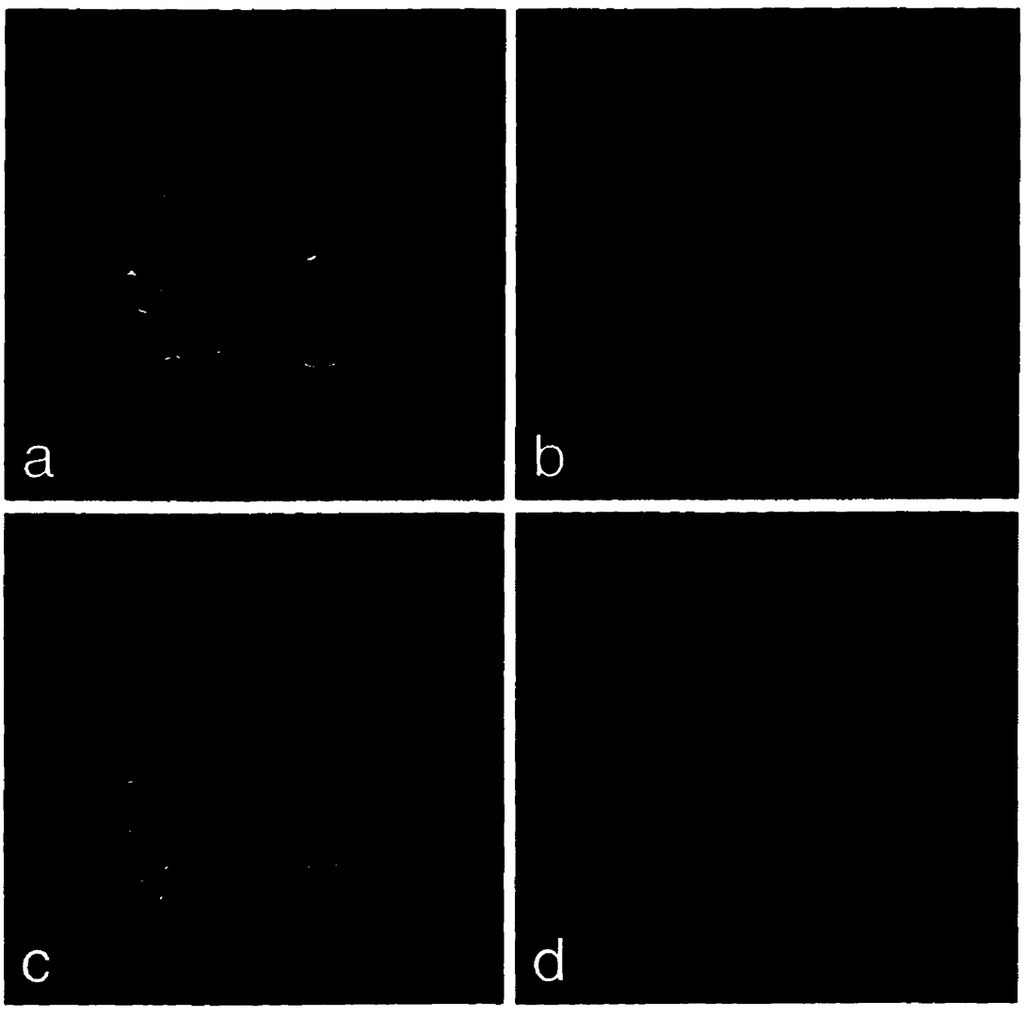

FIG. 3.13 a) Low flip angle FLASH (TR/TE = 74/40 ms, α = 10°) and (b) high flip angle PSAT-FLASH (TR/TE = 74/40 ms, α = 30°) images. Difference images (c) and (d) obtained after a 1° rotation of the original images demonstrate that reduced contrast at high flip angles (T1 weighting) reduces sensitivity to motion artifacts.

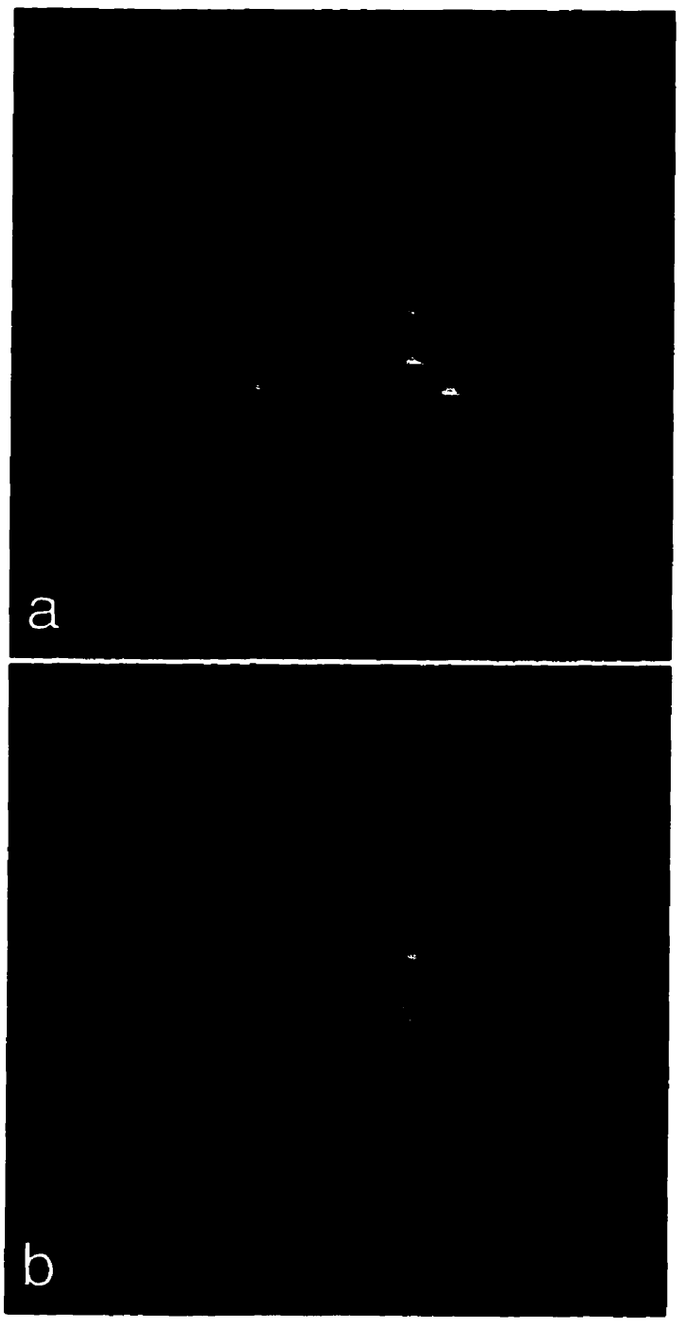

FIG. 3.14 Functional activation maps (Student's T) obtained for visual studies with (a) low flip angle FLASH (α = 10°), and (b) high flip angle PSAT-FLASH (α = 25°). Activations are overlaid on the mean T2* image for each study. Strong localized activations associated with flow changes in large vessels are attenuated in the PSAT study, and activations are more specifically confined to the visual cortex.

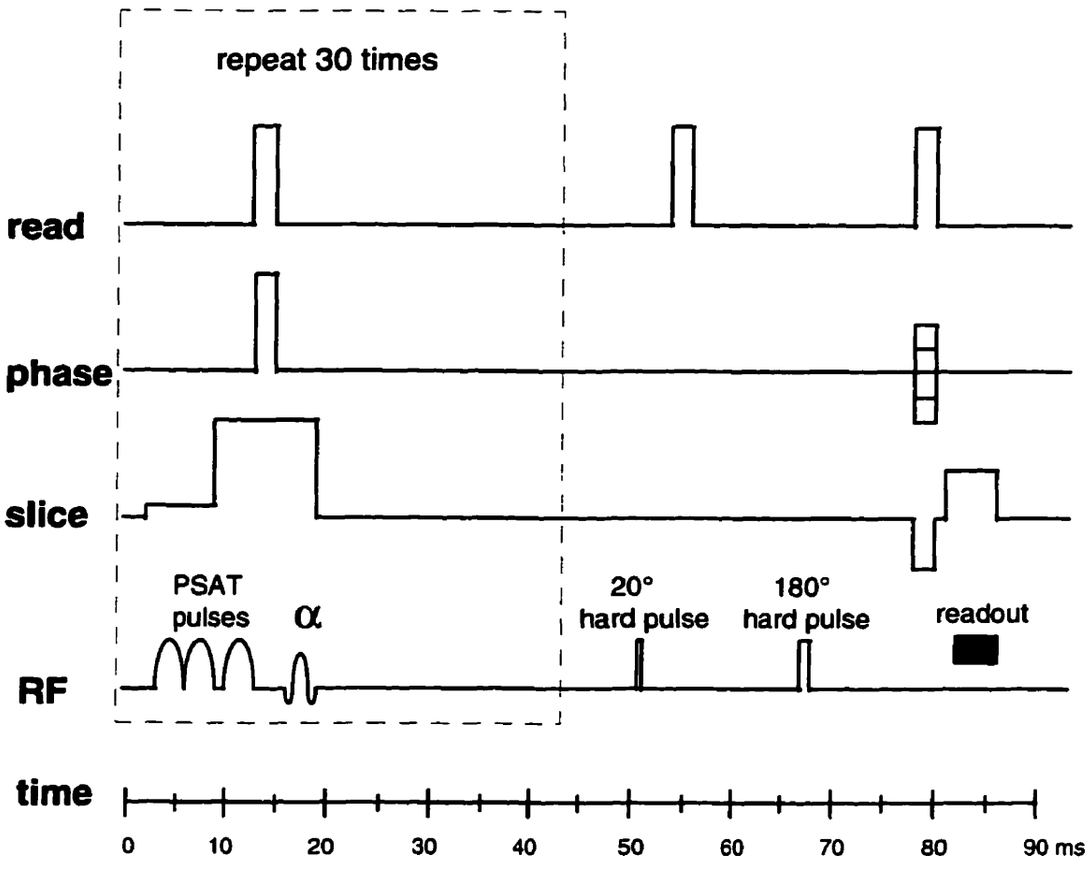

FIG. 3.15 Slice saturation profiling sequence. This pulse sequence was developed to image the true effect of PSAT acquisition on equilibrium magnetization over the excited volume. The PSAT excitation is first repeated 30 times at the desired TR rate to achieve equilibrium of longitudinal magnetization, as would occur during imaging. A spin-echo sequence then images the profile of the resulting equilibrium longitudinal magnetization. This pattern is repeated every five seconds for each phase encode step of the spin echo acquisition to allow full recovery of longitudinal magnetization between steps. The 20° flip angle is arbitrary, and could have been 90° to maximize signal.

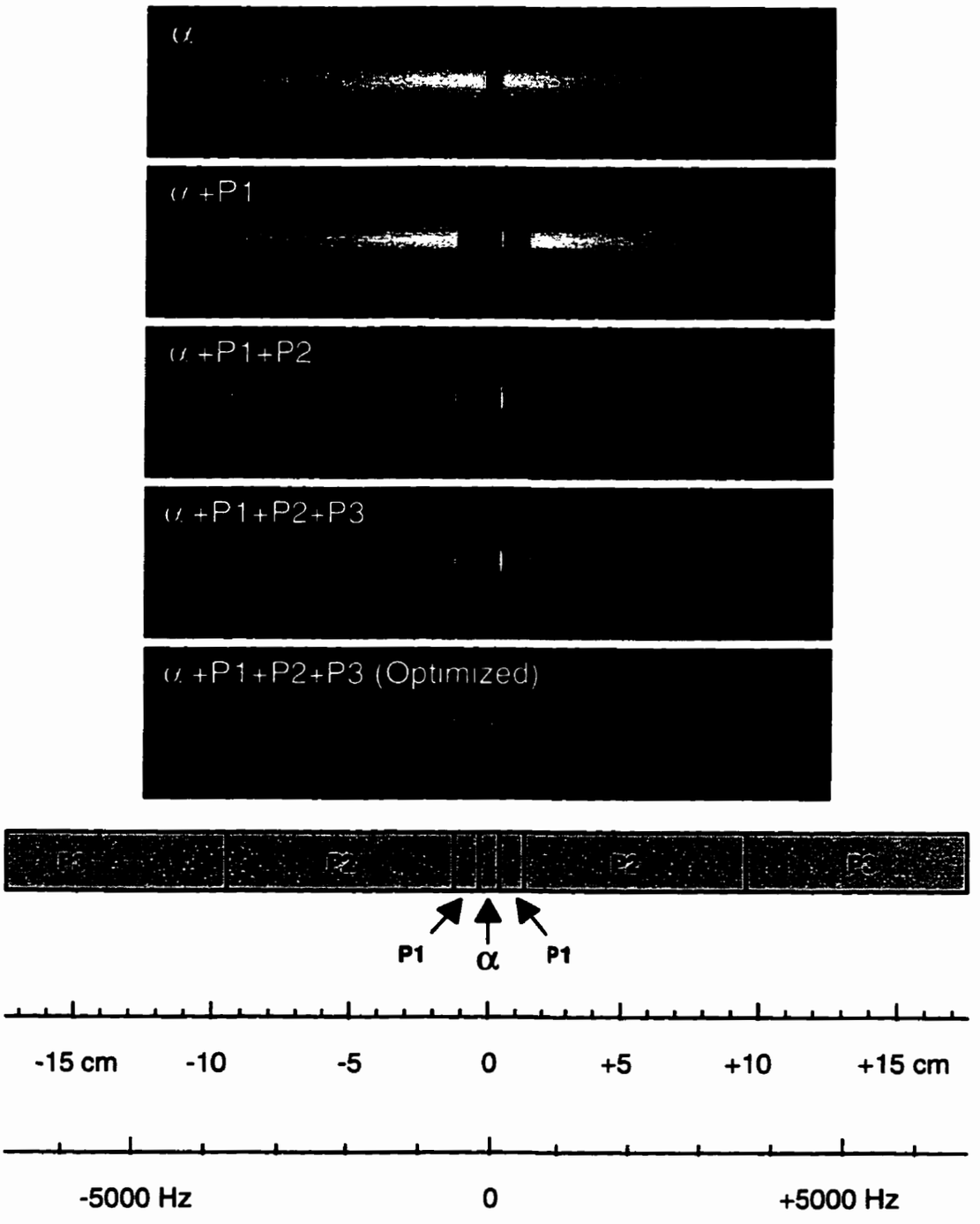

FIG. 3.16 Saturation profiles for PSAT pulses obtained with the sequence of Fig. 3.15. The first four profiles are for the PSAT implementation profiled in Fig. 3.7. Saturation profiling reveals that this implementation is not ideal. The final profile was obtained after further optimization. As in Fig. 3.7, the frequency scale is for the initial (weak) slice selection gradient.

Chapter 4

PHASE CORRECTION STRATEGIES

4.1 INTRODUCTION

Image stability is crucial if the small signal changes associated with fMRI studies are to be detected, and artifacts avoided. Factors that adversely affect image stability include gross motion (1) and localized cardiac and respiratory pulsations of blood and CSF (2,3). Gross motion and its consequences can be corrected by image registration (1) and other post-processing techniques (4). Localized physiological pulsations can be corrected by filtering time course data on a pixel-by-pixel basis (5,6).

More troubling, however, are global signal phase variations associated with physiology (7-18) as described in Section 2.3. These phase variations are particularly problematic for FLASH (or other multi-shot) imaging sequences (12), causing the k-space phase to vary between RF excitations. FLASH fMRI cannot be reliably performed, especially with long TE's at high field strengths, unless this phase instability problem is addressed.

Simple phase correction approaches have been proposed for fMRI by Merboldt *et al* (11) and for diffusion imaging by Ulug *et al* (19). In these approaches, the k-space phase of a single image is substituted for the phase of all other images of a series. This phase substitution approach can be implemented on either a point-by-point basis, or as a constant phase correction factor for each phase encode step.

Navigator echoes have been used successfully to correct phase variations in FLASH fMRI imaging (8,9). More recently Hu *et al* (13,14) proposed a sophisticated method for correcting cyclic phase and magnitude variations in k-space that treats each k-space point individually. The Hu method can potentially correct for both localized and global physiological fluctuations, provided the fluctuations follow cardiac and respiratory cycles in a regular manner.

In this work, new retrospective methods are proposed to measure and correct phase variations during multi-shot fMRI. The methods are superior to phase substitution methods in that there is no arbitrary assumption of an ideal (non-corrupted) image within a set. The methods also have the advantage of operating directly in k-space without need for navigator echoes. Furthermore, the methods are not constrained by the assumption that phase variations necessarily follow cardiac and respiratory cycles.

4.2 K-SPACE PHASE CORRECTION

4.2.1 INTRODUCTION

The phase variation mapping method of Sec. 2.3.2 shows that phase variations within an fMRI image series can be extracted directly from k-space data. The largest phase variations also follow a rather obvious pattern of slow variation through time (Fig. 2.6). By examining k-space, it should therefore be possible to remove unwanted

phase variations while still preserving phase changes associated with true functional activation.

4.2.2 K-SPACE PHASE CORRECTION METHOD

The premise of k-space phase correction is that physiological phase variations are best measured in k-space because k-space is where the corrections must be made. A k-space phase variation map $\Delta\Phi_i(t,s)$ (such as Fig. 2.6) is first computed for each image by Eqs. [2.4] and [2.5]. This map shows mostly "unwanted" phase change for each point in k-space. Care must be taken, however, not to remove all phase variation from all k-space points as some phase changes will be caused by true image change (activation) and not physiology.

A simple, yet highly effective approach is to assume that the artifactual phase change is constant near the center of k-space for each phase encode step (19). The phase variation is averaged over k-space for each phase encode step, and the k-space phase correction is given by

$$\Phi_i'(t,s) = \Phi_i(t,s) - \frac{\int_{k-space} \Delta\Phi_i(t',s) M_i(t',s) dt'}{\int_{k-space} M_i(t',s) dt'}, \qquad [4.1]$$

where $M_i(t,s)$ is the signal magnitude, and the integrals are performed over time within the readout sampling window. The phase variation average is weighted by the signal magnitude so that it is measured near the center of k-space for each readout line, where the SNR is high, and where the correction is most important.

Equation [4.1] subtracts a constant phase correction, calculated individually for each readout line (phase encode step) in k-space. Because the phase variation increases linearly with time after slice excitation, this correction should theoretically be applied as a linear ramp through k-space (as in Eq. [4.2] below). However it was found empirically that when the phase variation is measured near the center of k-space for each readout line (instead of in a navigator echo as described below), the time ramp is not necessary for the correction; the effect of adding a ramp was not noticeable even with long (32 ms) readout times.

4.2.3 EXTRAPOLATED NAVIGATOR CORRECTION METHOD

To evaluate the efficacy of k-space phase correction, experiments were performed in which a conventional navigator echo signal was acquired before phase encoding as shown in Fig. 2.5. The navigator phase variation $\Delta\phi_i(s)$ for each image i and phase encode step s was computed by the methods of Eqs. [2.4] and [2.5], and averaged for 3 ms around the navigator center at TE=15 ms. Because physiological phase variations increase with time after slice excitation, it is necessary to extrapolate the navigator phase

correction into k-space (8). Let $\Phi_i(t,s)$ be the phase of k-space for image i, where t is time after slice excitation and s is the phase encode number. The extrapolated navigator correction is then given by

$$\Phi_i'(t,s) = \Phi_i(t,s) - \Delta\phi_i(s)\left(\frac{t}{15\text{ms}}\right). \qquad [4.2]$$

4.2.4 RESULTS

Fig. 4.1 shows the results of extrapolated navigator echo correction (Eq. [4.2]) and k-space phase correction (Eq. [4.1]) on the entire set of 24 images that Figs. 2.6 and 2.7 are based on. The k-space phase correction is more effective at reducing noise due to phase variations.

In another volunteer in Fig. 4.2, sets of 19 consecutive images were obtained at three difference transverse slice locations (TR/TE = 74/40 ms, α=10°). k-Space phase correction reduces image instability at all slice locations, especially the inferior slice, which is closer to the chest.

The utility of the k-space phase correction is demonstrated in a simple visual stimulation study. 30 images were acquired (TR/TE = 74/40 ms, α=10°), with visual stimulation alternately turned off and on every six images. (Stimulation was performed

with light-emitting diode goggles (Grass Instruments, Quincy, MA) flashing alternating red/green colors at 8 Hz.) The first image of each stimulation or rest interval was discarded, leaving a total of 25 images in the time course. These images were registered (20) as described in Chapter 5 to correct for inter-image motion.

Temporal image noise and activation results are shown in Fig. 4.3. Noise is reduced, and false activations are removed by the correction. The spatial extent of apparent activation is also reduced by the correction. However, examination of pixel time courses in peripheral active areas removed by the correction reveals time courses that do not correlate well with the paradigm, suggesting that the broader activation in the uncorrected images is artifactual.

The false nature of an activation removed by the correction is illustrated by the time courses in Fig. 4.4. The apparent activation indicated by the arrow in Fig. 4.3(c) is due to an anomalous signal drop occurring during the first rest period. This drop is removed by the correction, as are other fluctuations that bear no relationship to the paradigm. In the true active region, the correction removes the signal drop artifact, while leaving the more obvious visual activation time course unchanged.

It still might be asked whether under some circumstances k-space phase correction might remove true activations. Complete removal of activations doesn't seem likely given the very limited class of image changes that would be associated with a global

phase change across a readout line, although attenuation of some activations remains a theoretical possibility. In practice with dozens of studies we have found that the opposite is more typically true: k-space phase correction removes image instabilities that were making true activations undetectable in the uncorrected image set.

4.3 K-SPACE ORTHOGONALIZATION

4.3.1 INTRODUCTION

k-Space phase correction, as described above, removes only a limited class of phase variations; variations that are global across the slice being imaged. While this is sufficient to improve image stability in most cases, it is not a comprehensive correction. Intra-image motion and localized physiological pulsations introduce complex variations in signal phase and magnitude that are not constant across a k-space readout line.

To address this problem, Hu *et al* (13,14) developed a correction method in which the magnitude and phase of each k-space point is corrected individually over the image time course. The variation pattern of each k-space point is first measured during a resting state. A "unit cycle" variation waveform is then calculated for each point over cardiac and respiratory cycles. Later, during the fMRI experiment, physiological monitoring (external monitoring or navigator echo) is used to determine where the subject is within cardiac and respiratory cycles at any given moment. The appropriate correction for that

point in the cycle is then applied to each k-space point. A key assumption of the method is pseudoperiodicity; the assumption that physiological variations will always follow the same waveform as during the resting state.

Another comprehensive approach is possible that does not assume pseudoperiodicity, or require baseline measurements during a resting state. If n images are acquired, the time course of each k-space point can be regarded as an n-dimensional vector. Physiology (measured externally or by MR signal) can also be regarded as a vector-- a vector that represents an unwanted signal pattern. Any component of k-space time course vectors that is correlated with the physiology vector (or vectors) can then be mathematically removed. This is k-space orthogonalization.

4.3.2 K-SPACE ORTHOGONALIZATION METHOD

Let $S(k_x,k_y,i)$ be the k-space representation of image i, with magnitude and phase components S_m and S_p. In a FLASH imaging sequence, a physiological variation vector (containing respiration, cardiac, and gross motion components) can be extracted from k-space data as

$$p(k_y,i) = \frac{\sum_{k_x} \bar{S}_m(k_x,k_y)(S_p(k_x,k_y,i) - \bar{S}_p(k_x,k_y))}{\sum_{k_x} \bar{S}_m(k_x,k_y)} \qquad \text{Eq. [4.3]}$$

where k_y is the phase encode direction, and $\bar{\mathbf{S}}$ is the mean of k-space over all images. (Note that Eq. [4.3] is simply the discrete version of the phase variation calculated in Eqs. [2.6] and [4.1].) Alternatively, $p(k_y,i)$ can be obtained from the phase of a navigator echo, or even by external monitoring of respiration.

Let $\mathbf{s}(k_x,k_y,i) = \mathbf{S}(k_x,k_y,i) - \bar{\mathbf{S}}(k_x,k_y)$ be the image-to-image variation of k-space from the mean. Then define vectors $\bar{\mathbf{s}}(k_x,k_y)$ and $\bar{\mathbf{p}}(k_y)$ in image number space. The essence of k-space orthogonalization is to remove all components of variation "parallel" to physiology:

$$\bar{\mathbf{s}}' = \bar{\mathbf{s}} - \frac{\bar{\mathbf{p}}(\bar{\mathbf{p}} \cdot \bar{\mathbf{s}})}{\bar{\mathbf{p}} \cdot \bar{\mathbf{p}}} \qquad \text{Eq. [4.4]}$$

The correction can in principle be performed on either the Cartesian or polar representation of complex k-space data. In practice it is found that performing the correction on the magnitude and phase representation is more effective, probably because most of the correction is to the phase part of the data.

If strong cardiac fluctuations are present, a small additional benefit can be obtained by decomposing $\bar{\mathbf{p}}$ into cardiac and respiratory components $\bar{\mathbf{c}}$ and $\bar{\mathbf{r}}$ by bandpass filtering, and orthogonalizing with respect to them separately:

$$\bar{s}' = \bar{s} - \frac{\bar{c}(\bar{c}\cdot\bar{s})}{\bar{c}\cdot\bar{c}} - \frac{\bar{q}(\bar{q}\cdot\bar{s})}{\bar{q}\cdot\bar{q}} \qquad \text{Eq. [4.5]}$$

where $\bar{q} = \bar{r} - \bar{c}(\bar{c}\cdot\bar{r})/(\bar{c}\cdot\bar{c})$, which is a Gram-Schmidt process making k-space orthogonal to the cardiac/respiratory hyperplane.

4.3.3 RESULTS

Fig. 4.5 shows standard deviation maps for a set of consecutive sagittal images (TR/TE = 74/40 ms, α=20°) with strong arterial pulsation artifacts. k-Space orthogonalization is more effective than k-space phase correction for reducing the artifacts.

In the study of Fig. 4.6, the subject was trained to nod his head in ~5 mm excursions at a rate of once per second during imaging (TR/TE = 74/40 ms, α=10°). k-Space orthogonalization is remarkably effective in correcting the associated motion artifacts. This study shows one of the most powerful advantages of k-space orthogonalization: The method is not limited to the correction of cardiac and respiratory phase variations. Rather, the method can correct for any artifact, regardless of complexity, provided the artifact is correlated with a global phase shift.

In Fig. 4.7, results from a visual study are shown (same experiment parameters as the visual study of Sec. 4.2.4). k-Space orthogonalization produces an enhancement and smoothing of the inferior activation, with an improved time course (Fig. 4.8) compared to k-space phase correction. The superior activation is attenuated by k-space orthogonalization. This implies that the superior activation has a component correlated with physiology, suggesting a possible vascular origin.

Orthogonalizing with respect to cardiac and respiratory components independently as per Eq. [4.5] produces even more attenuation of the superior activation, and attenuation of the inferior activation as well (Fig. 4.9). The tradeoff of sensitivity for specificity with independent orthogonalization may therefore be excessive.

4.4 SUMMARY

k-Space phase correction is a simple and effective method for reducing phase variation artifacts in multi-shot fMRI. Obvious artifacts in signal time courses are removed without apparent effect on authentic activations. The technique does not assume any regularity in phase variation, and is therefore also suitable for correcting non-physiological artifacts, such as motion-related phase shifts. Artifactual phase shifts can be produced by motion in the imaging volume (gradient moment effect) and also by motion anywhere inside the bore of the magnet (B0 perturbation effect).

k-Space phase correction does not require navigator echoes or any other pulse sequence modification. With appropriate adjustment of Eq. [4.1] for k-space trajectory, it can be used retrospectively to correct data acquired with any multi-shot sequence, including spiral and interleaved EPI imaging. k-Space phase correction may be of special utility for simultaneous multislice acquisitions (21-23) that suffer from increased motion sensitivity due to intensive gradient play.

Beyond k-space phase correction, k-space orthogonalization is a more comprehensive correction that removes any changes in k-space that are correlated with global phase shifts. The method is especially effective for correcting complex intra-image motion artifacts, and artifacts associated with localized physiological pulsations.

REFERENCES

1. J. V. Hajnal, R. Myers, A. Oatridge, J. E. Schwieso, I. R. Young, G. M. Bydder, Artifacts due to stimulus correlated motion in functional imaging of the brain. *Magn. Reson. Med.* **31**, 283-291 (1994).

2. R. M. Weisskoff, J. Baker, J. Belliveau, T. L. Davis, K. K. Kwong, M. S. Cohen, B. R. Rosen, Power spectrum analysis of functionally-weighted MR data: What's in the noise?, *in* "Proc., SMRM, 12th Annual Meeting, New York, 1993," p. 7.

3. P. Jezzard, D. LeBihan, C. Cuenod, L. Pannier, A. Prinster, R. Turner, An investigation of the contribution of physiological noise in human functional MRI studies at 1.5 Tesla and 4 Tesla, *in* "Proc., SMRM, 12th Annual Meeting, New York, 1993," p. 1392.

4. K. J. Friston, S. Williams, R. Howard, R. S. J. Frackowiak, R. Turner, Movement-related effects in fMRI time-series. *Magn. Reson. Med.* **35**, 346-355 (1996).

5. P. A. Bandettini, A. Jesmanowicz, E. C. Wong, J. S. Hyde, Processing strategies for time-course data sets in function MRI of the human brain. *Magn. Reson. Med.* **30**, 161-173 (1993).

6. B. Biswal, E. A. DeYoe, J. S. Hyde, Reduction of physiological fluctuations in fMRI using digital filters. *Magn. Reson. Med.* **35**, 107-113 (1996).

7. D. C. Noll, W. Schneider, J. D. Cohen, Artifacts in functional MRI using conventional scanning, *in* "Proc., SMRM, 12th Annual Meeting, New York, 1993," p. 1407.

8. D. C. Noll, W. Schneider, Respiration artifacts in functional brain imaging: Sources of signal variation and compensation strategies, *in* "Proc., SMR, 2nd Annual Meeting, San Francisco, 1994," p. 647.

9. X. Hu, S.-G. Kim, Reduction of physiological noise in functional MRI using navigator echo. *Magn. Reson. Med.* **31**, 495-503 (1994).

10. G. H. Glover, A. T. Lee, Motion artifacts in fMRI: Comparison of 2DFT with PR and spiral scan methods. *Magn. Reson. Med.* **33**, 624-635 (1995).

11. K. D. Merboldt, G. Kruger, W. Hanicke, A. Kleinschmidt, J. Frahm, Functional MRI of human brain activation combining high spatial and temporal resolution by a CINE FLASH technique. *Magn. Reson. Med.* **34**, 639-644 (1995).

12. D. C. Noll, J. O'Brien, Simulation of physiological effects in functional MRI. *in* "Proc., SMR/ESMRMB, Annual Meeting, Nice, 1995," p. 794.

13. X. Hu, T. H. Le, T. Parish, P. Erhard, Retrospective estimation and correction of physiological fluctuation in functional MRI. *Magn. Reson. Med.* **34**, 201-212 (1995).

14. T. H. Le, X. Hu, Retrospective estimation and correction of physiological artifacts in fMRI by direct extraction of physiological activity from MR data. *Magn. Reson. Med.* **35**, 290-298 (1996).

15. B. Wowk, M. C. McIntyre, J. K. Saunders, Physiologic artifact correction in fMRI without navigator echoes, *in* "Proc., ISMRM, 4th Annual Meeting, New York, 1996," p. 1822.

16. B. Wowk, M. C. McIntyre, J. K. Saunders, Origin and removal of fMRI physiological noise: a multi-modal approach, *in* "Proc., ISMRM, 5th Annual Meeting, Vancouver, 1997," p. 1690.

17. B. Wowk, M. C. McIntyre, J. K. Saunders, k-Space orthogonalization: A new remedy for fMRI physiological noise, *in* "Proc., ISMRM, 5th Annual Meeting, Vancouver, 1997," p. 351.

18. B. Wowk, M. C. McIntyre, J. K. Saunders, k-space detection and correction of physiological artifacts in fMRI. *Magn. Reson. Med.* **38**, in press (1997).

19. A. M. Ulug, P. B. Barker, P. C. M. van Zijl, Correction of motional artifacts in diffusion-weighted images using a reference phase map. *Magn. Reson. Med.* **34**, 476-480 (1995).

20. B. Wowk, M. C. McIntyre, G. Scarth, J. K. Saunders, Image registration for high resolution fMRI: Experience with a Fourier algorithm, *in* "Proc., SMR/ESMRMB, Annual Meeting, Nice, 1995," p. 845.

21. R. S. Menon, H. Merkle, K. Ugurbil, A novel multi-slice FLASH sequence for functional magnetic resonance imaging, *in* "Proc., SMRM, 12th Annual Meeting, New York, 1993," p. 1203.

22. G. Liu, G. Sobering, J. Duyn, C. T. Moonen, A functional MRI technique combining principles of echo-shifting with a train of observations (PRESTO). *Magn. Reson. Med.* **30**, 764-768 (1993).

23. T. Loenneker, F. Hennel, J. Hennig, Multislice interleaved excitation cycles (MUSIC): An efficient gradient-echo technique for functional MRI. *Magn. Reson. Med.* **35**, 870-874 (1996).

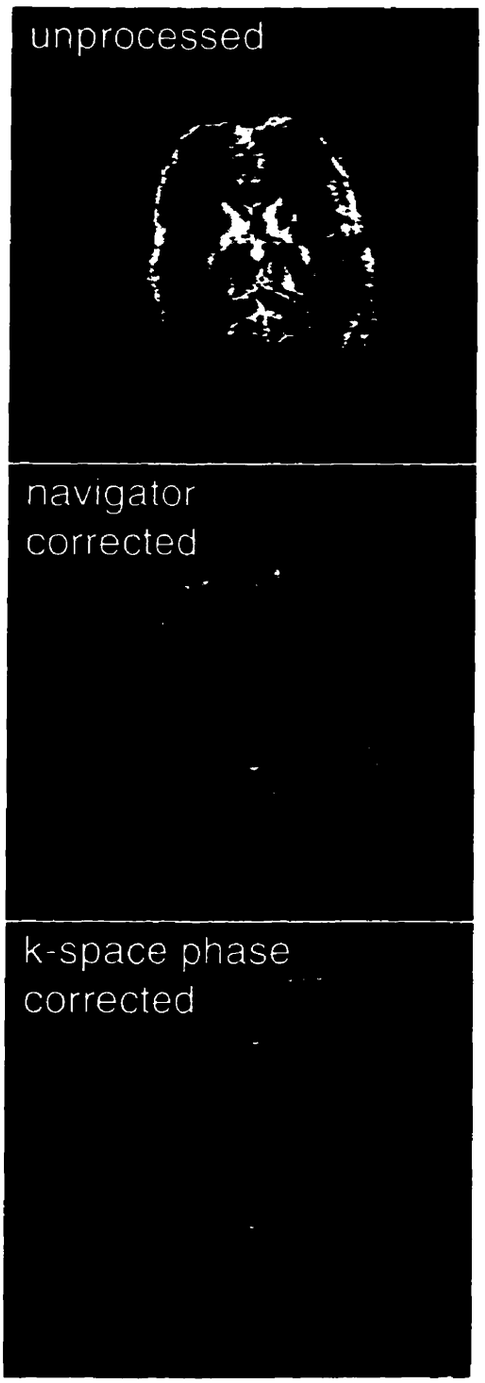

FIG. 4.1 Pixel standard deviation maps obtained prior to correction, and after extrapolated navigator correction vs. k-space phase correction. k-Space phase correction is more effective than navigator echo correction at reducing signal fluctuations.

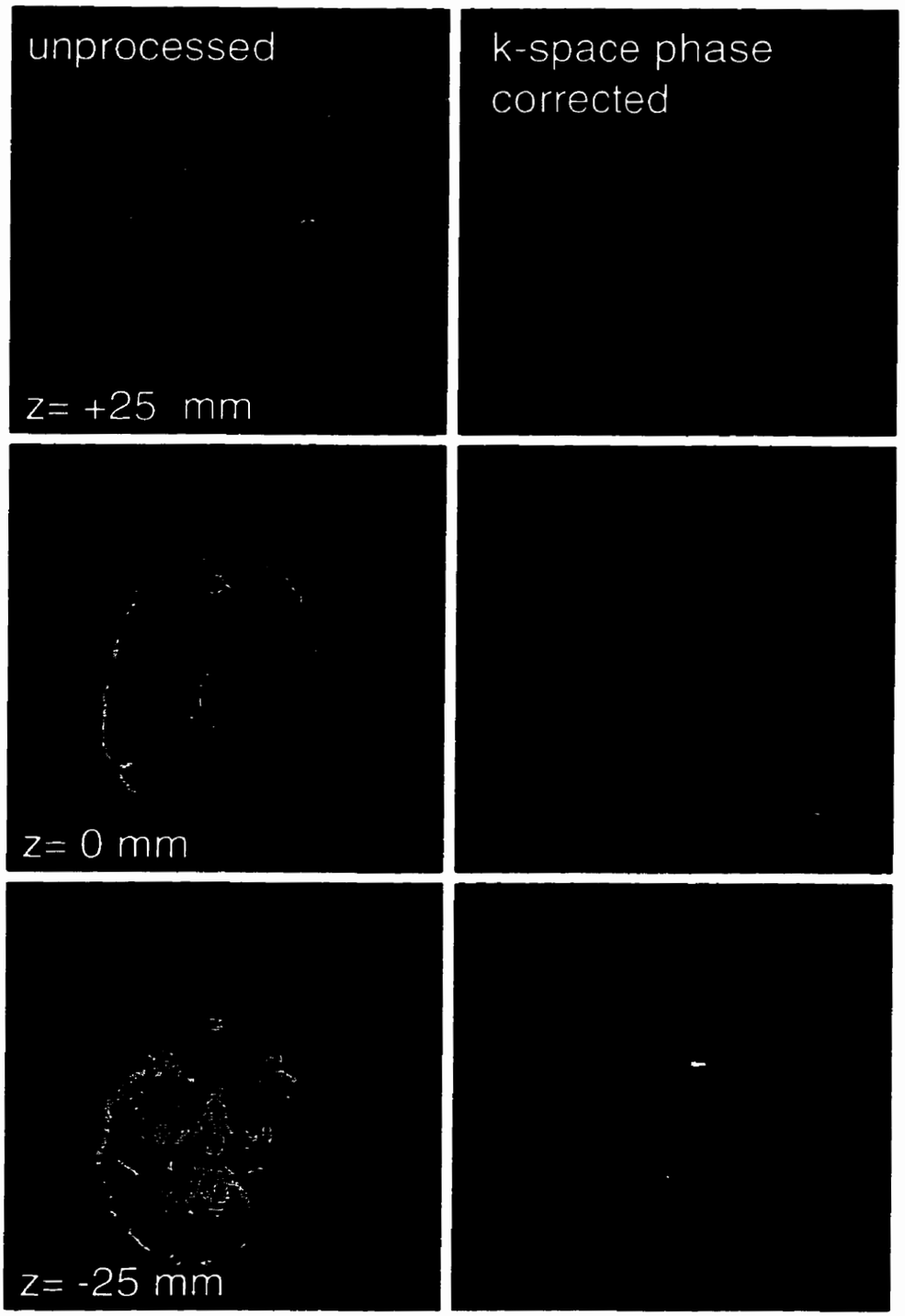

FIG. 4.2 Standard deviation maps obtained from consecutive FLASH images at three different transverse slice locations, before and after k-space phase correction. Correction has the most dramatic effect on inferior slices, where phase variations are greatest.

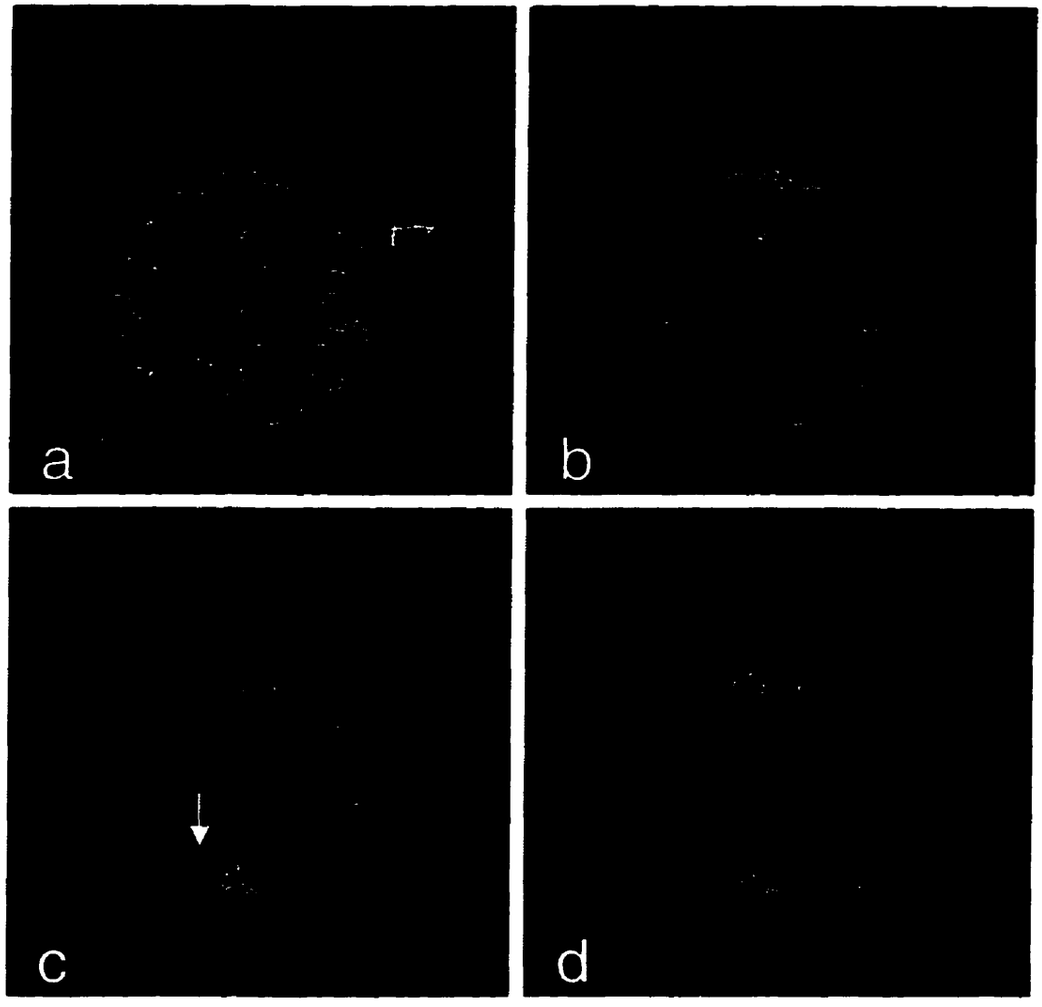

Fig. 4.3 Standard deviation maps obtained during a functional study of the visual cortex before (a) and after (b) k-space phase correction. Activation maps prepared by simple subtraction show numerous artifacts in the uncorrected image set (c) vs. the corrected set (d). The arrow in (c) shows a prominent and misleading artifact that is removed by the correction.

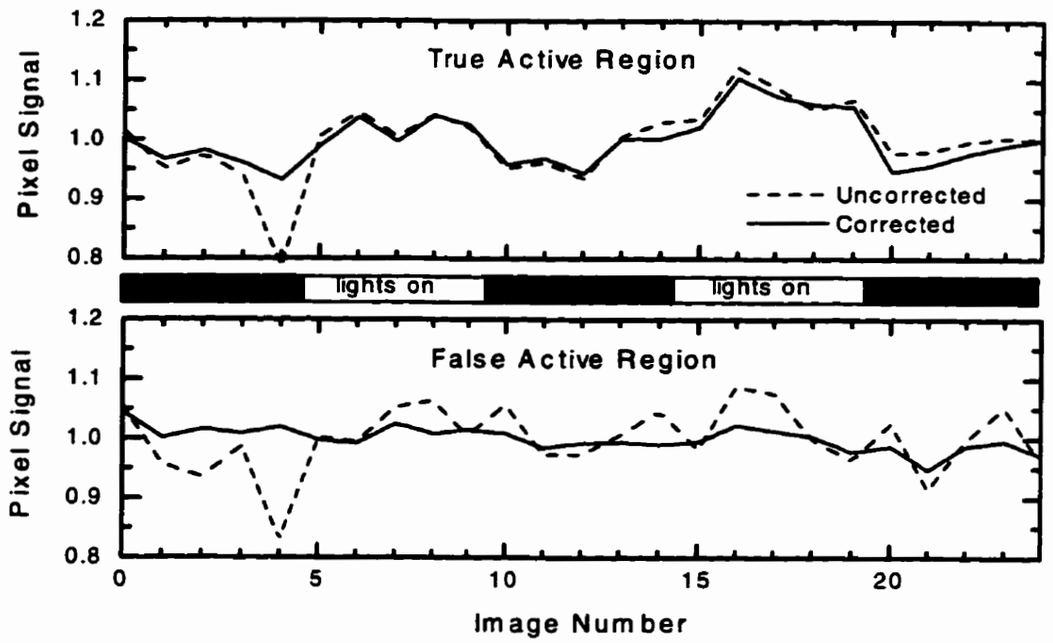

Fig. 4.4 Effect of correction on the time course of single pixels in true active and false active regions. The false active region is indicated by the arrow on the subtraction image in Fig. 4.3(c). The true active region is the region that remains active after correction in Fig. 4.3(d).

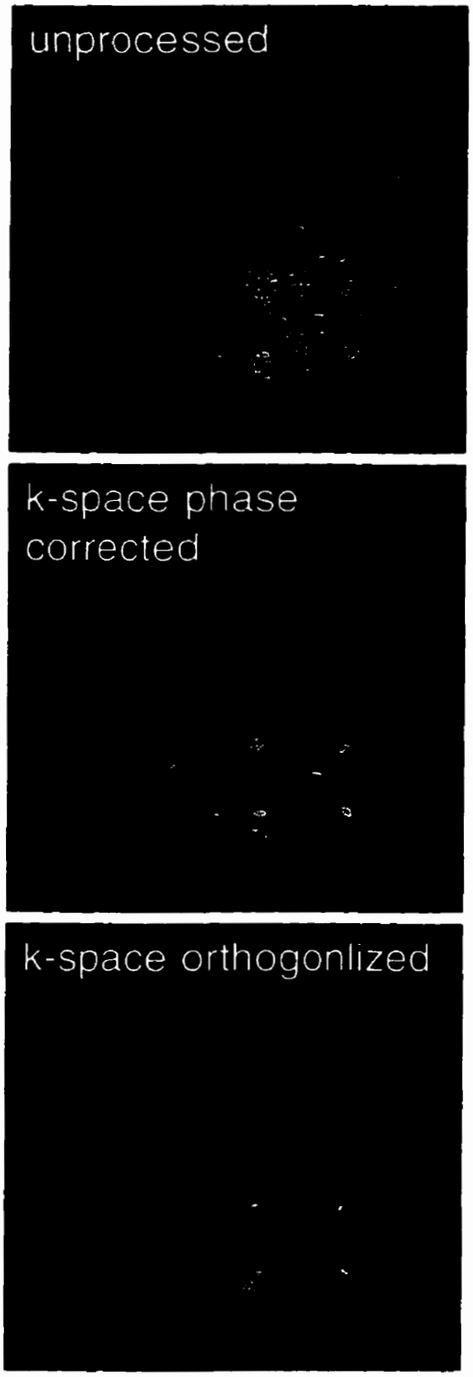

FIG. 4.5 Standard deviation maps of a sagittal slice obtained prior to correction, and after k-space phase correction vs. k-space orthogonalization. k-Space orthogonalization is more effective than simple phase correction for reducing ghosting artifacts caused by cardiac pulsations.

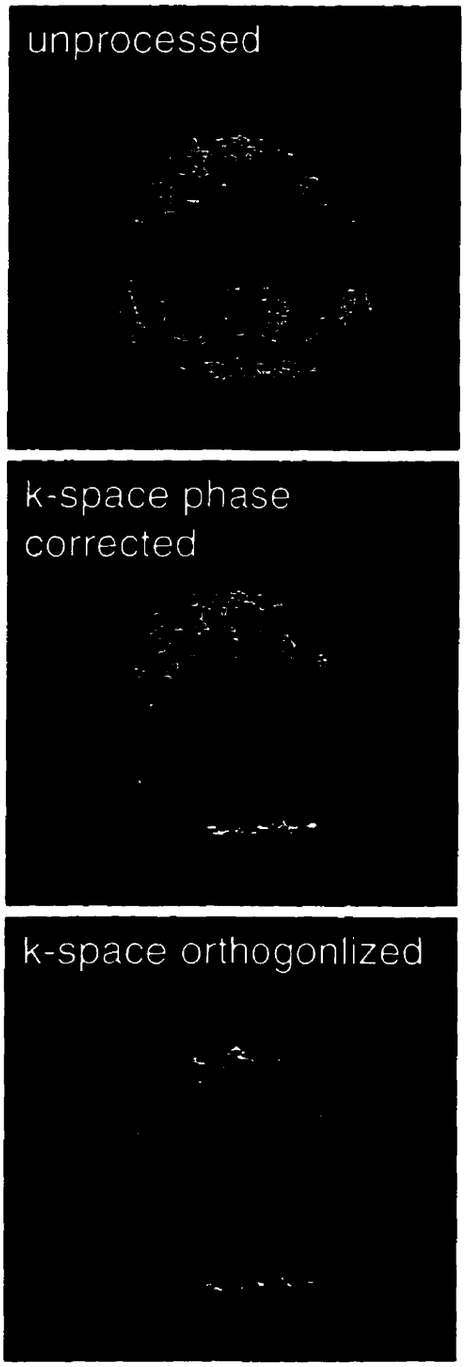

FIG. 4.6 Standard deviation maps of a transverse slice imaged while the subject was nodding their head. k-Space orthogonalization is more effective than phase correction for correcting the complex artifacts introduced by this motion.

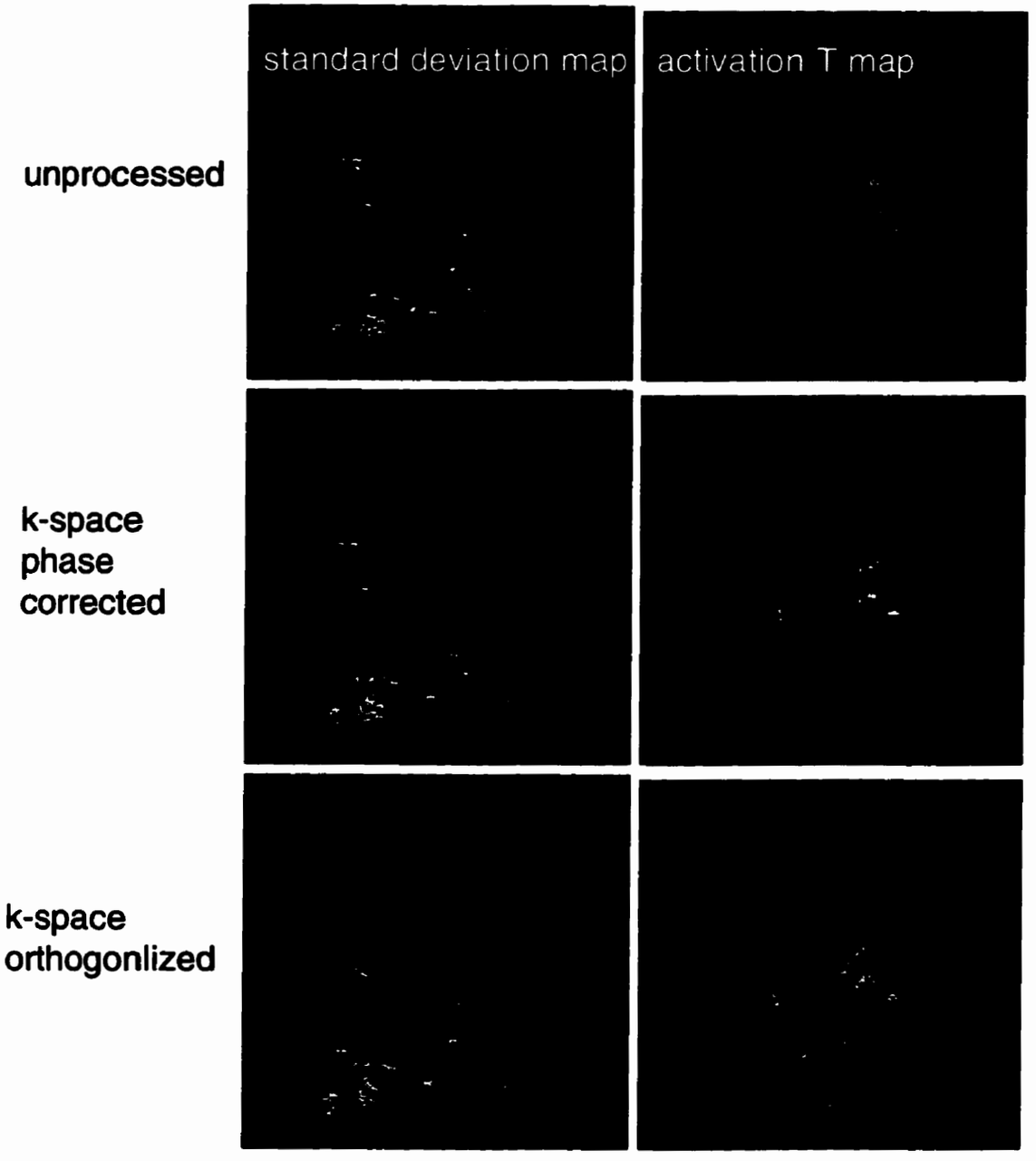

Fig. 4.7 Standard deviation maps and activation maps (zoomed to show the area of interest) obtained from a visual stimulation study in the sagittal plane. k-Space orthogonalization results in a smoother cortical activation pattern without the vascular hot spots apparent after k-space phase correction.

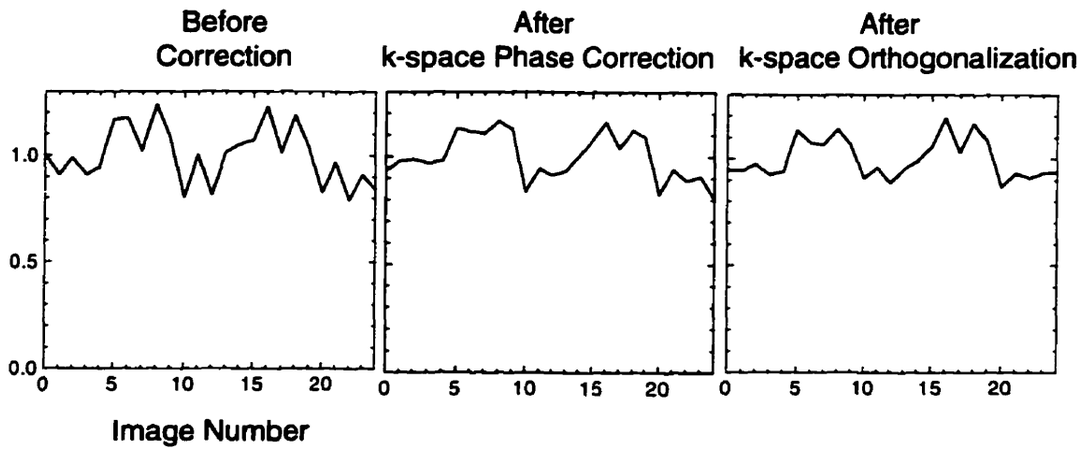

Fig. 4.8 Time course of a single pixel in an active region of Fig. 4.7. k-Space orthogonalization results in a time course with the most stable baseline (resting state) level.

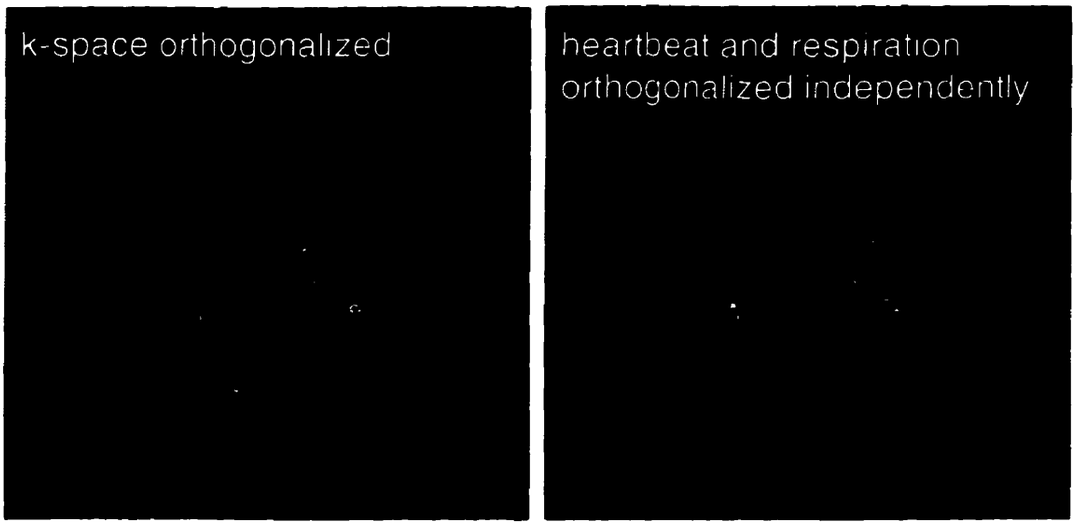

Fig. 4.9 Activation T maps for the study of Fig. 4.7, comparing k-space orthogonalization using Eq. [4.4] to orthogonalization using Eq. [4.5], which removes cardiac and respiratory correlations independently. The independent orthogonalization strongly suppresses activations, suggesting that a cardiac frequency component exists in the activations.

Chapter 5

IMAGE REGISTRATION

5.1 INTRODUCTION

As discussed in Chapter 2, inter-image motion is an important source of fMRI artifacts (1,2). Even with restraining devices, small movements during long fMRI studies are inevitable. Furthermore, the use of restraining devices is not always practical (such as for elderly or infirm subjects). A variety of algorithms for digitally realigning, or registering, fMRI image sets with sub-voxel accuracy have therefore between implemented in two (1-10) and three (4,5,7) dimensions.

Two dimensional (in-plane) registration is most important because pixel dimensions are usually smaller than the image slice thickness. A time-tested method of in-plane image registration is image cross correlation (3,11,12). The cross correlation between two images A(x,y) and B(x,y) is given by

$$CC(x,y) = \sum_{x'} \sum_{y'} A(x',y')B(x' - x, y' - y). \qquad \text{Eq. [5.1]}$$

If image B contains the same features as A, but translationally displaced, the translational displacement will be given by the values of x and y for which CC is maximum. The cross correlation function is most conveniently calculated via the Correlation Theorem of Fourier analysis:

$$CC(x,y) = FT^{-1}(FT(A)FT(B)^{*}) \qquad \text{Eq. [5.2]}$$

where FT denotes Fourier transformation. Rotations can be detected and corrected by either iterative maximization of CC as a function of rotation angle (11,12), or by performing the Fourier cross correlation procedure in polar coordinates (10).

Cross correlation is computationally slow compared to other, more sophisticated image registration methods (1,4,5,8,9,10). Its virtues are simplicity and robustness (due to its largely non-iterative nature, and utilization of all image points). It was implemented in this work due to the practical necessity of rapidly developing an image registration capability at a time when no other software was readily available.

5.2 IMAGE REGISTRATION METHOD

The algorithm outlined in Fig. 5.1 was implemented on a SGI Challenge XL server using the IDL (Research Systems, Inc.) programming language. The program code is listed in Appendix C. Because discrete cross correlation only determines translations to the nearest pixel, images are interpolated to successively larger matrix sizes as the registration progresses. The core routine (performed for each matrix size) consists of only 20 lines of IDL code.

Images (typically 128 x 256 matrix size) are first reduced to a 128 x 128 scale. The image to be registered is then rotated between -10° and +10° in 1° steps, computing

Motion Factor analysis also provides justification for stopping the registration process at 1024 x 1024 matrix size. In image registration trials with a high quality fMRI dataset, registering on the 1K x 1K scale reduced the Motion Factor to 10 compared to 14 with only 512 x 512 registration. However extending the registration to a 2K x 2K matrix only improved the Motion Factor from 10.45 to 9.9.

5.3 MOTION FACTOR

One possible measure of goodness-of-registration between two images is the sum of all squared differences between corresponding pixels (which is ideally zero in the case of identical images with no noise). However this parameter is relatively insensitive to small motions. A more sensitive measure of misregistration may be constructed by weighting the squared differences by an edge detection function. An example of such a parameter operating between images A and B is the Edge Weighted Variance defined by

$$\mathrm{EWV} = \frac{\sum_x \sum_y \mathrm{sobel}(\mathrm{A}(x,y))(\mathrm{A}(x,y) - \mathrm{B}(x,y))^2}{\sum_x \sum_y \mathrm{sobel}(\mathrm{A}(x,y))} \qquad \text{Eq. [5.3]}$$

where sobel(A(x,y)) is the sobel filtered (13) (edge-enhanced) version of the reference image A.

If a set of images is perfectly registered, then the only difference between image pairs will be random noise. Values of EWV computed for different image pairs under these circumstances will be normally distributed (Central Limit Theorem) with a mean and variance determined by the noise properties of the image set. If the intrinsic noise of the images is known or measured, the variance of EWV can be theoretically calculated. The difference between the theoretical variance of EWV, and the observed variance, then becomes a measure of non-random noise (i.e. motion or other image instability) within the image set.

Let s be the signal difference between corresponding pixels of an image pair. Assume that s is a random variable with a normal distribution of mean zero, and variance σ_s^2. The function s^2 will then have a mean $<s^2>=\sigma_s^2$ and variance

$$\sigma_{s^2}^2 = <(s^2-\sigma_s^2)^2> \qquad \text{Eq. [5.4]}$$

$$= <(s^4 - 2s^2\sigma_s^2 + \sigma_s^4)>$$

$$= <s^4> - 2<s^2>\sigma_s^2 + \sigma_s^4$$

$$= 3\sigma_s^4 - 2\sigma_s^4 + \sigma_s^4 \qquad \text{(4th central moment of gaussian} = 3\sigma^4)$$

$$= 2\sigma_s^4$$

This result is necessarily an approximation because s is not expected to strictly follow a normal distribution. Nevertheless the assumption of normal statistics permits some useful further development.

Consider the function $T = \frac{\sum w_i s_i^2}{\sum w_i}$, where w_i are arbitrary weighting factors. T will have a mean $<T>=\sigma_s^2$ and variance

$$2\sigma_s^4 \frac{\sum w_i^2}{\left(\sum w_i\right)^2} = 2 < T >^2 \frac{\sum w_i^2}{\left(\sum w_i\right)^2} . \qquad \text{Eq. [5.5]}$$

Note that EWV is of the same form as function T (where the weighting factors are pixels of the sobel filtered image), and is therefore expected to show a variance over an image set of

$$\sigma_{EWV}^2 = 2 < EWV >^2 \frac{\sum_x \sum_y \text{sobel}(A(x,y))^2}{\left(\sum_x \sum_y \text{sobel}(A(x,y))\right)^2} \qquad \text{Eq. [5.6]}$$

if random noise is the only cause of image differences.

Let $(\sigma_{EWV})_{observed}$ be the observed standard deviation of EWV calculated between the first image and all subsequent images of a series. Let $(\sigma_{EWV})_{Eq.\ [5.6]}$ be the theoretical standard deviation of EWV calculated by Eq. [5.6] (which assumes that the only difference between image pairs is random noise). The Motion Factor (MF) is then defined as

$$MF = \frac{(\sigma_{EWV})_{observed}}{(\sigma_{EWV})_{Eq.\ [5.6]}}, \qquad \text{Eq. [5.7]}$$

and is expected to be close to unity if only random noise is present in the image set. In practice the Motion Factor is invariably much larger than unity, reflecting both image misregistration, the general instability of fMRI images, and perhaps the non-gaussian statistcs of image noise.

5.4 RESULTS

Fig. 5.2 shows results from a cognitive/motor fMRI study performed on an elderly male using no head restraints (TR/TE = 60/40 ms, α=10°, 60 consecutive images). The image registration program detected a 4° roll during the study (Fig. 5.4). Without image registration, the motion is far too large to permit meaningful detection of functional activations. However after image registration, interesting cognitive and motor activations can be detected. The Motion Factor changes from 379 pre-registration to 45 post-registration.

Even with healthy, compliant subjects small motions are unavoidable, as seen in the high resolution study of Fig. 5.3. In this case the image registration program detects

and corrects a 1/2° rotation and 0.5 mm displacement with noticeable improvement of the activation results.

5.5 SUMMARY

Fourier domain cross correlation with iterative optimization of rotations is a simple and robust method for in-plane registration of fMRI images to correct for inter-image motion. With image registration, meaningful activations can be detected even when large in-plane motions are present.

The Motion Factor statistic is a useful measure of inter-image motion and stability of images within fMRI datasets. It can provide an objective accept/reject criterion for the quality of fMRI data.

REFERENCES

1. J. V. Hajnal, R. Myers, A. Oatridge, J. E. Schwieso, I. R. Young, G. M. Bydder. Artifacts due to stimulus correlated motion in functional imaging of the brain. *Magn. Reson. Med.* **31**, 283-291 (1994).

2. J. V. Hajnal, G. M. Bydder, I. R. Young, fMRI: Does correlation imply activation? *NMR in Biomedicine* **8**, 97-100 (1995).

3. Y. Cao-Y, V. L. Towle, D. N. Levin, J. M. Balter, Functional mapping of human motor cortical activation with conventional MR imaging at 1.5 T. *J. Magn. Reson. Imaging.* **3**, 869-875 (1993).

4. J. V. Hajnal, N. Saeed, A. Oatridge, E. J. Williams, I. R. Young, G. M. Bydder, Detection of subtle brain changes using subvoxel registration and subtraction of serial MR images. *J. Comput. Assist. Tomogr.* **19,** 677-691 (1995).

5. K. J. Friston, J. Ashburner, C. D. Frith, J. B. Poline, J. D. Heather, R. S. J. Frackowiak, Spatial registration and normalization of images. *Human Brain Mapping* **3**, 165-189 (1995).

6. W. F. Eddy, M. Fitzgerald, D. C. Noll, Improved image registration by using Fourier interpolation. *Magn. Reson. Med.* **36**, 923-931 (1996).

7. A. Kassam, M. L. Wood, Fourier registration of three-dimensional brain MR images: exploiting the axis of rotation. *J. Magn. Reson. Imaging*. **6**, 894-902 (1996).

8. M. E. Alexander, R. L. Somorjai, The registration of MR images using multiscale robust methods. *Magn. Reson. Imaging*. **14**, 453-468 (1996).

9. M. E. Alexander, G. Scarth, R. L. Somorjai, An improved robust heirarchical registration algorithm. *Magn. Reson. Imaging*. **15**, 505-514 (1997).

10. L. C. Maas, B. D. Frederick, P. F. Renshaw, Decoupled automated rotational and translational registration for functional MRI time series data: the DART registration algorithm *Magn. Reson. Med.* **37**, 131-139 (1997).

11. S. M. Jones, A. L. Boyer, Investigation of an FFT-based correlation technique for verification of radiation treatment setup. *Med. Phys*. **18**, 1116-1125 (1991).

12. D. H. Hristov, B. G. Fallone, A grey-level image alignment algorithm for registration of portal images and digitally reconstructed radiographs. ***Med. Phys.* 23**, 75-84 (1996).

13. C. A. Lindley, *in* "Practical Image Processing in C" Wiley, New York, 1991.

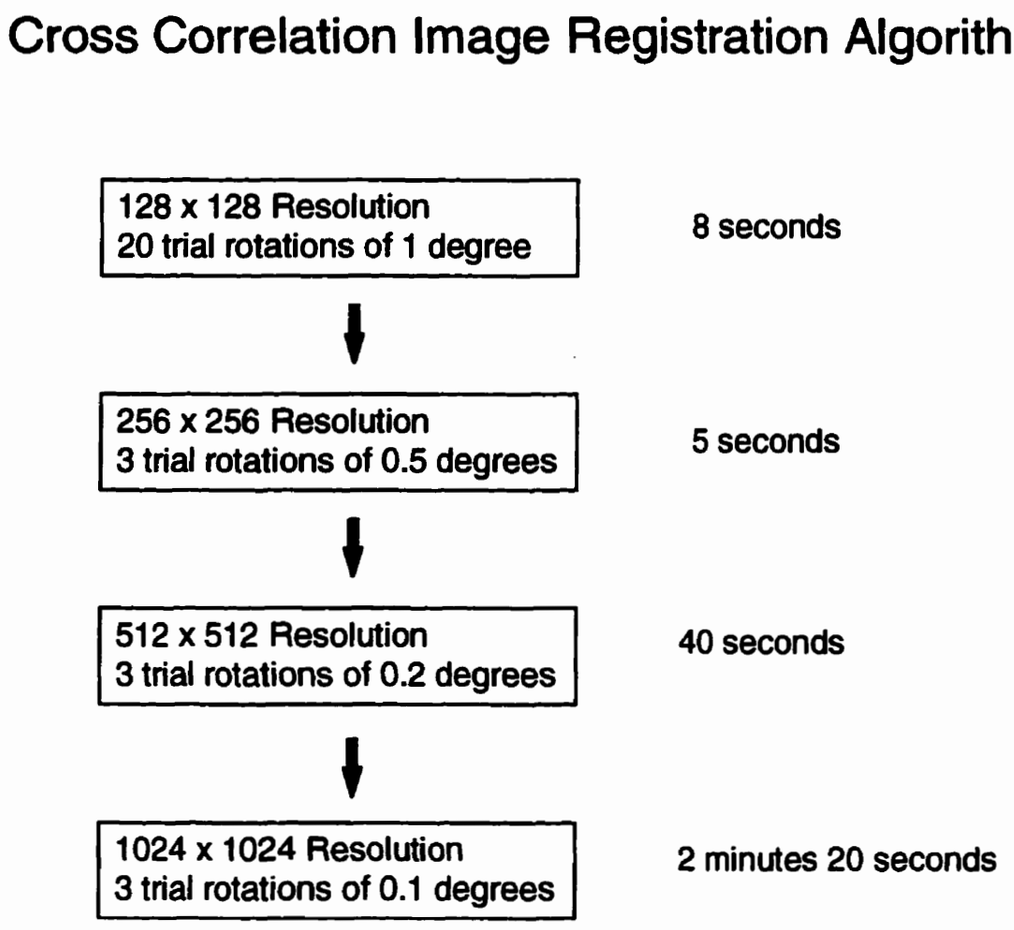

FIG. 5.1 Fourier domain cross correlation is used to determine the optimum translation for each rotation trial increment. The process is repeated on successively finer scales. The computer time spent on each scale is shown on the right.

FIG. 5.2 fMRI study of a 87 year old male. For this subject's comfort, head restraints were not used. A 4 degree roll occurred during the 10 minute study, as is evident in the temporal standard deviation map of the unregistered image set. After registration, activations related to the combined cognitive, right-hand motor task were successfully detected.

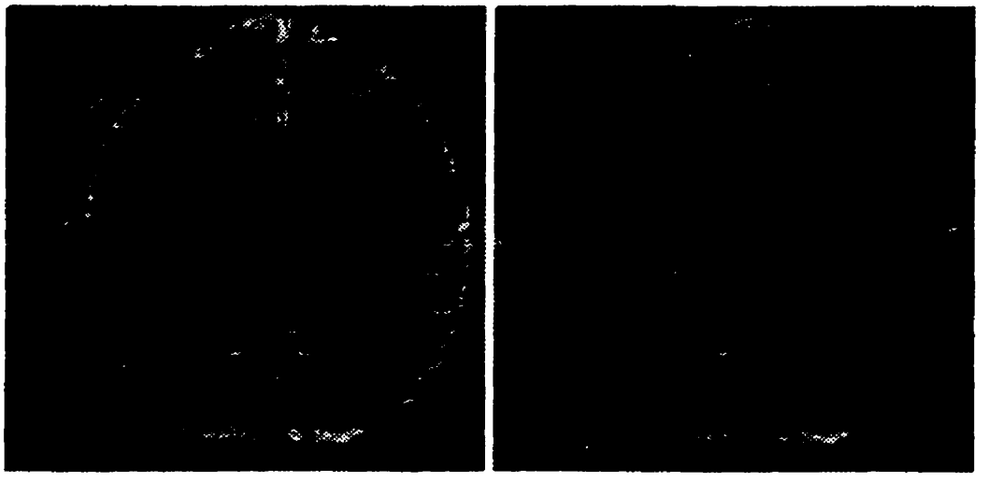

Fig. 5.3(a) Standard deviation maps obtained during a high resolution study of the visual cortex (1.2 x 0.6 mm^2 in-plane resolution). Movements as small as 1/2° rotation (Fig. 5.4(b)) seriously affect signal stability near edges.

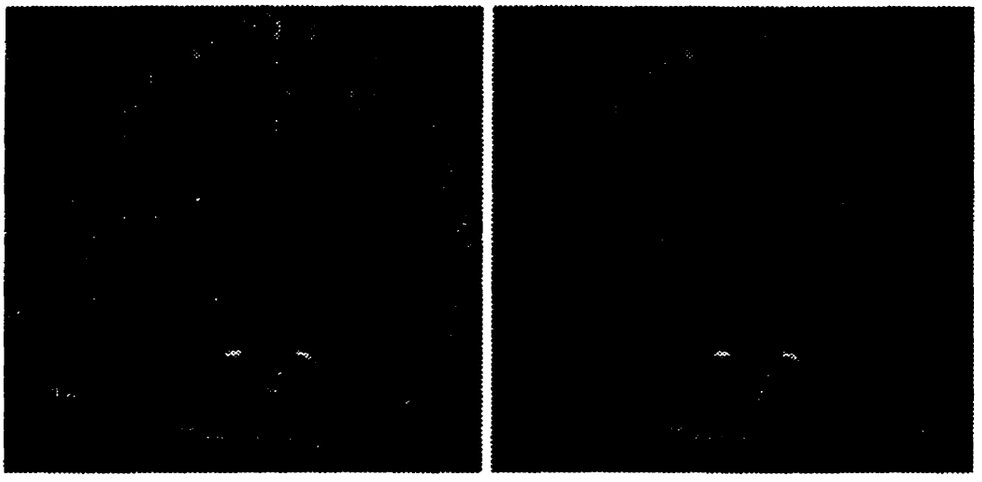

Fig. 5.3(b) Difference images obtained by subtracting 10 stimulation images from 15 rest images within the dataset above. Activations produced by the 8Hz alternating red/green stimulation are clearly visible with minimum artifacts after image registration.

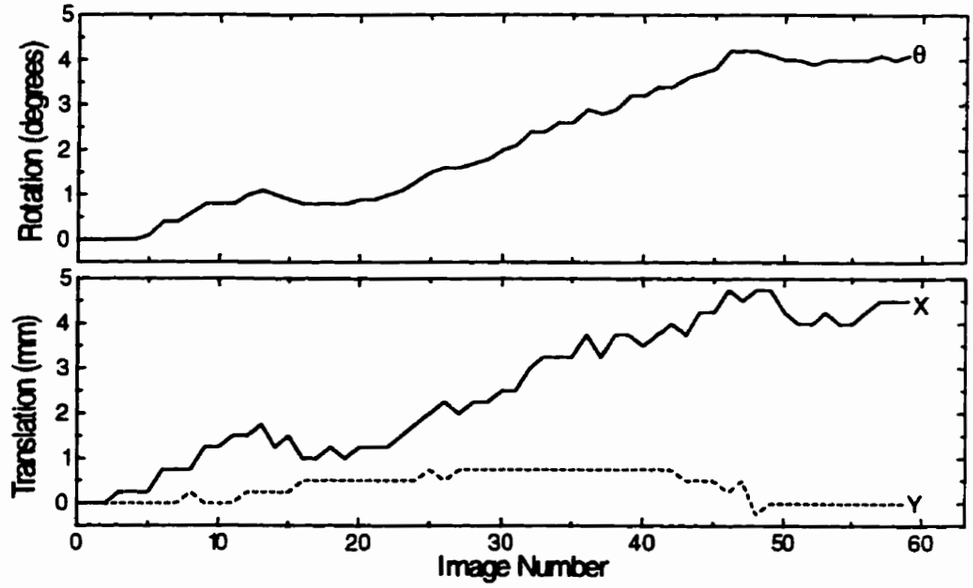

Fig. 5.4(a) Large movements detected and corrected by the registration program for the study of Fig. 5.2.

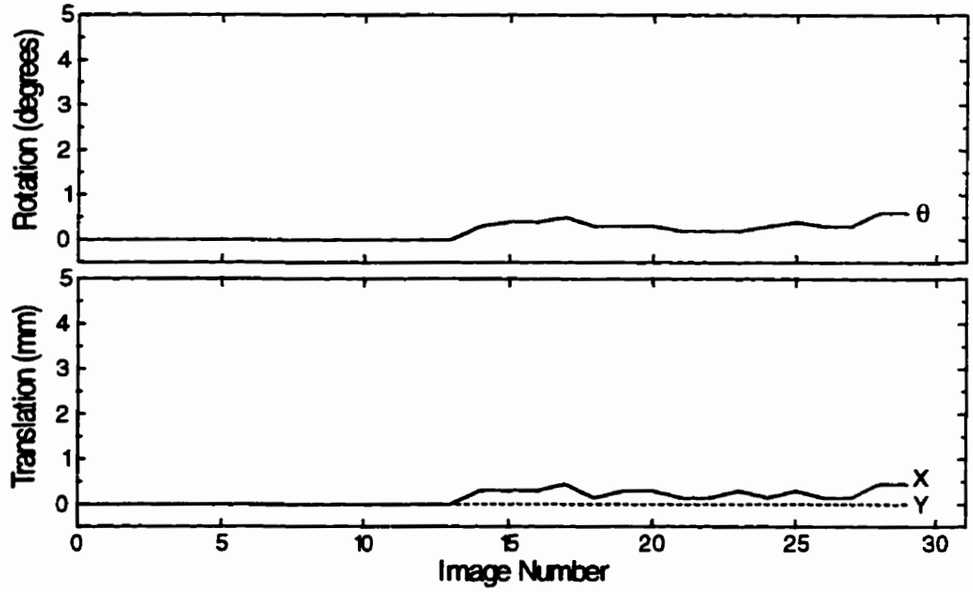

Fig. 5.4(b) Small movements detected and corrected for the study of Fig. 5.3. Small movements of this magnitude are almost universal in fMRI studies.

Chapter 6

COMBINED CORRECTIONS

In this brief Chapter, the synergy of combining PSAT acquisition, phase correction and image registration methods to fMRI studies is explored. Examples are taken from the visual stimulation study described in Sec. 3.3.4., which was performed in a difficult, artifact-prone sagittal slice orientation.

Figure 6.1 shows the interplay between k-space phase correction and image registration. The unregistered datasets show artifactual activations on the superior margin of the brain caused by stimulus-correlated motion. Image registration removes the artifact. However without phase correction there is little remaining statistically significant activation. The combination gives the greatest density of activations in anatomically correct areas.

The interactions between different phase correction methods and PSAT acquisition are shown in Fig. 6.2. Compared to simple k-space phase correction, both k-space orthogonalization and PSAT acquisition reduce the number and extent of significant activations. Sensitivity is sacrificed for specificity in each case, but by different mechanisms. k-Space orthogonalization attenuates activations that contain a physiological pulsation component. PSAT acquisition attenuates activations associated with changes in flow rather than changes in oxygenation.

The synergy between artifact reduction methods is not always subtle. In the case of the inferior transverse slice of Fig. 6.3, the combination of intense physiological phase

fluctuations and pulsatile flow makes fMRI virtually impossible. Only the combination of PSAT acquisition and k-space phase correction gives images sufficiently stable for activations to conceivably be detected.

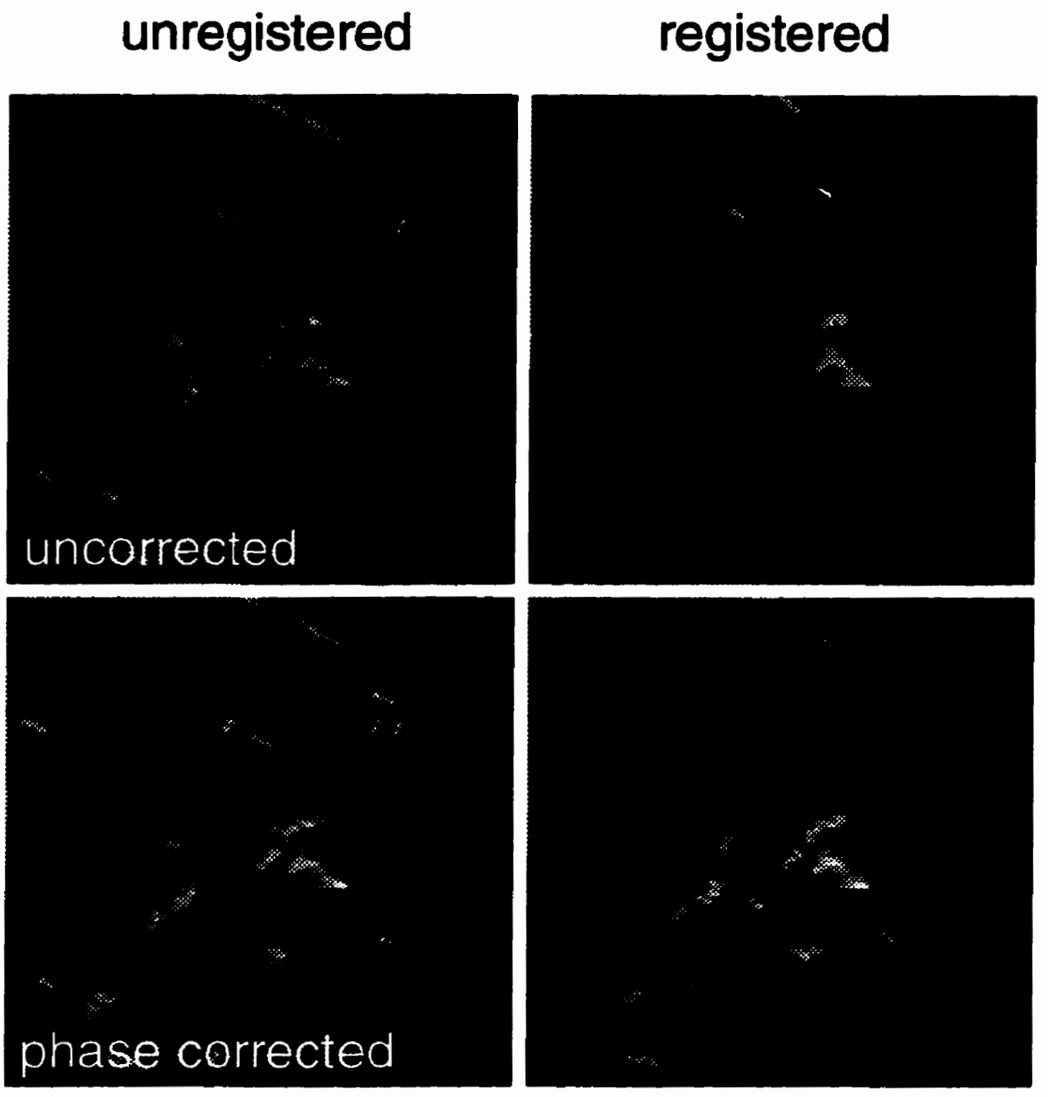

FIG. 6.1 Activation T-maps ($p<0.01$) obtained for a visual study (TR/TE =74/40 ms, $\alpha=10°$) as a function of image registration and k-space phase correction.

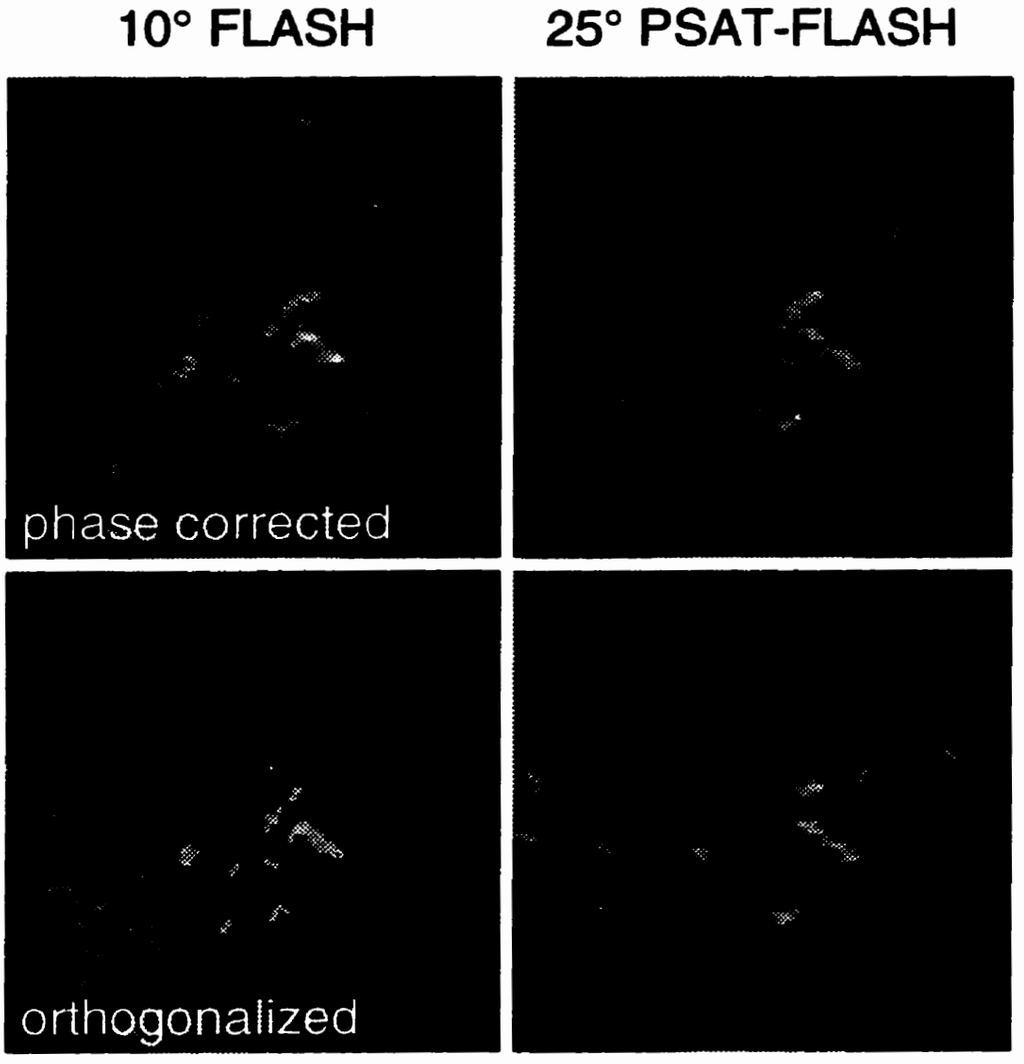

FIG. 6.2 Activation T-maps obtained as a function of phase correction method and slice excitation method. All image sets are registered.

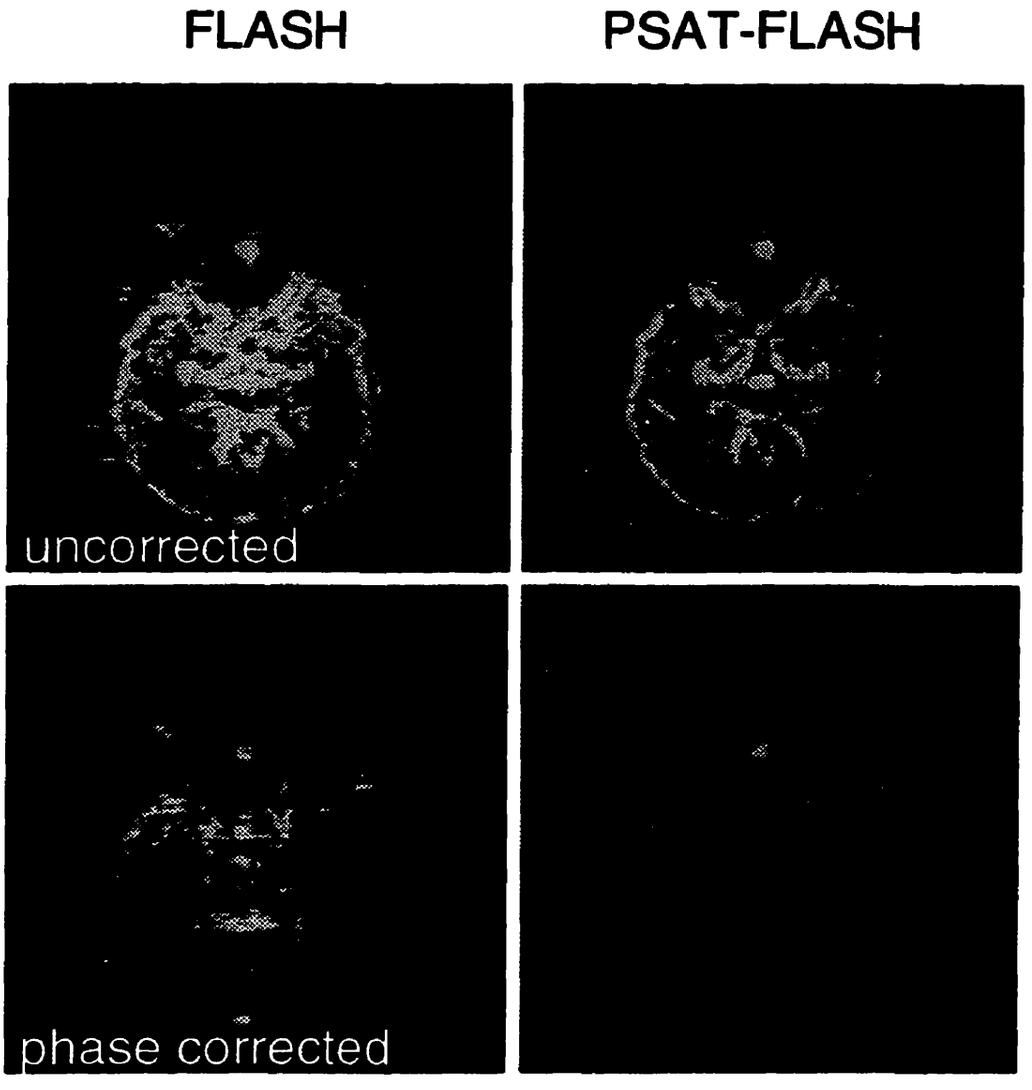

FIG. 6.3 Standard deviation maps showing the combined effect of PSAT flow suppression and k-space phase correction. The combination is highly effective for reducing physiological noise in this inferior transverse slice (TR/TE = 74/40 ms, α=30°).

Chapter 7

SUMMARY AND DISCUSSION

Blood-oxygen-level-dependent (BOLD) fMRI detects localized changes in brain activity via changes in blood oxygenation. Deoxyhemoglobin is slightly paramagnetic, and induces magnetic field non-uniformities, signal dephasing and image intensity loss on T2*-weighted MRI images. Conversely, increased oxygenation associated with brain activation causes a signal increase within these images.

BOLD fMRI is prone to artifacts caused by blood flow variations, magnetic field variations, and gross motion. fMRI in the presence of these artifacts can be unreliable, and sometimes impossible.

To address the problem of sensitivity to changes in blood flow, a new method of slice excitation called Partial Presaturation (PSAT) was developed. PSAT is a method of applying RF excitation to a 3D volume, but only acquiring an image from a 2D slice. PSAT is immune to flow-related signal enhancement, which makes it ideal for acquiring images at high repetition rates and high RF flip angles that optimize signal strength. PSAT allows the addition of T1-weighting to fMRI images, which improves immunity to in-plane motion artifacts. In addition, the uniform suppression of longitudinal magnetization over a 3D volume reduces out-of-plane motion artifacts

Movement of the heart and lungs during multi-shot MR imaging causes minute (~0.01 ppm) shifts in the main magnetic field, B0, that are sufficient to corrupt the phase and stability of T2*-weighted functional images. Several retrospective corrections to the

activation maps (enhancing some activations, attenuating others), but the correction is nevertheless always beneficial because the slow phase variations that the correction removes are highly unlikely to be caused by anything other than motion or physiology.

The PSAT acquisition method helps insure that fMRI experiments are true BOLD experiments (exclusively dependent on blood oxygenation changes). Whether to allow some flow sensitivity by not using PSAT (with the understanding that flow-related signal changes will originate from macrovasculature) is a matter of discretion for the investigator.

The utility of k-space orthogonalization, as opposed to k-space phase correction, is uncertain given the marked attenuation of activations that sometimes occurs after the correction. Whether the attenuated activations are false positives (perhaps associated with pulsing vessels) is matter for further study.

In conclusion, image registration and k-space phase correction are very valuable tools for improving the quality of FLASH fMRI studies. PSAT acquisitions are useful when specificity for BOLD (blood-oxygen-level-dependent) effects, and freedom from flow-related artifacts, are desired. The development of acquisition and post-processing methods to further minimize physiological noise in fMRI experiments remains an ongoing concern, especially for FLASH imaging. In particular, more sophisticated post-

processing techniques that remove physiology-correlated changes without attenuating true activations need to be explored.

Appendix A

INTRODUCTION TO MR IMAGING

Magnetic resonance imaging (MRI) is a process whereby an NMR sample is excited by a brief radiofrequency (RF) pulse, and magnetic field gradients are applied during signal reception to encode spatial information. After RF excitation, a sample in a main magnetic field of strength B_0 will generate a signal of frequency $\omega=\gamma B_0$, where γ is the gyromagnetic ratio (42.5 MHz/Tesla for protons). Field gradients of the form $G_x= dB_0/dx$, $G_y=dB_0/dy$, $G_z=dB_0/dz$ are then imposed to create a position-dependent frequency distribution of the MR signal.

Perhaps the simplest MR imaging method is the FLASH ("Fast Low-Angle Shot") sequence shown schematically in Fig. A.1. An RF excitation with a small frequency distribution about the resonant frequency γB_0 is applied in the presence of a G_z gradient. This results in the selective excitation of a "slice" within the object to be imaged. A "phase encode" gradient G_y is then applied for a brief time t_p. This induces a position-dependent phase variation in the MR signal of the form $\exp(iy\gamma G_y t_p)$. Finally a "readout" gradient G_x is applied that induces an additional phase variation of the form $\exp(ix\gamma G_x t)$, where t is time during signal readout. Neglecting relaxation, the total received signal from the object at time instant t during readout will be given by

$$F(G_y,t) = \int_{x,y-plane} f(x,y)e^{i\gamma xG_x t + i\gamma yG_y t_p}\,dxdy\,. \qquad \text{Eq. [A.1]}$$

This sequence of events (RF excitation, gradient manipulation, and signal reception as shown in Fig. A.1) is repeated for different values of G_y (typically 128 values), compiling a complete 2D dataset $F(G_y,t)$. Performing the substitution

$$k_x = \gamma G_x t \quad \text{and} \quad k_y = \gamma G_y t_p \qquad \text{Eq. [A.2]}$$

allows $F(G_y,t)$ to be re-expressed as

$$F(k_x,k_y) = \int_{x,y-plane} f(x,y) e^{ik_x x + ik_y y} dxdy, \qquad \text{Eq. [A.3]}$$

giving $F(k_x,k_y)$, the Fourier representation of the object in so-called "k-space". Neglecting normalization, the MR image may then be reconstructed by the corresponding inverse Fourier Transform:

$$f(x,y) = \int_{k-space} F(k_x,k_y) e^{-ik_x x - ik_y y} dk_x dk_y \qquad \text{Eq. [A.4]}$$

In FLASH imaging, the time between successive RF excitations during image acquisition called the TR time. The time between slice excitation and signal reception is called the TE time. The TR time (and RF flip angle) controls T1 image contrast. Short TR and high RF flip angle adds image weighting that is related to the T1 relaxation constant of tissue. TE controls T2* contrast. Long TE adds image weighting that is

related to the T2* relaxation time of tissue. (T2* being relaxation due to the combined effects of T2 relaxation and dephasing due to static field non-uniformity within voxels.) Low RF flip angle (or long TR) combined with short TE gives a pure proton density image.

EPI ("Echo-Planar Imaging") is similar to FLASH imaging, except that the G_x and G_y gradients are both manipulated during readout to collect signal from all points in k-space after a single RF excitation. For EPI, the TR time is synonymous with the image repetition time.

The most commonly-used clinical MR imaging method is spin-echo imaging. In spin-echo imaging, a 90° RF pulse is followed by a 180° pulse, which has the effect of time-reversing phase dispersions caused by static magnetic field non-uniformity. Long-TE spin-echo images are therefore purely T2-sensitive instead of T2*-sensitive as FLASH images would be.

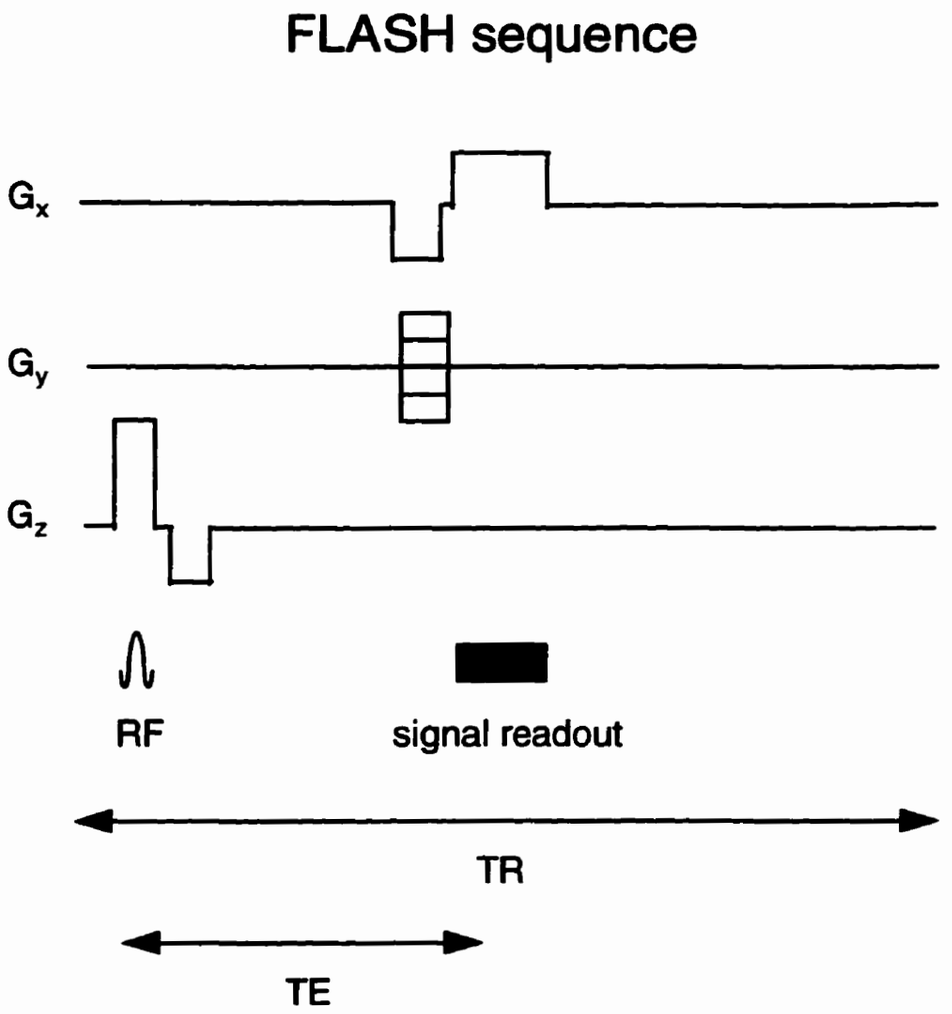

FIG. A.1 Prototypical FLASH imaging sequence. The pattern of RF excitation and signal reception is repeated with different values of the phase encode gradient, G_y, until data sufficient for a complete image is obtained.

Appendix B

SLOW-RAMP

ECHO PLANAR IMAGING (EPI)

A.1 INTRODUCTION

Echo planar imaging (EPI) was first introduced by Mansfield in 1977 (1,2), with additional refinements appearing a decade later (3-5). In EPI, a single RF excitation is followed by rapid gradient switching to cover all of k-space in a single acquisition (Fig. B.1). This "single shot" characteristic of EPI makes it immune to artifacts caused by intra-image physiological fluctuations.

EPI imaging was the premier imaging method used in early fMRI experiments (6-11). It has since become the method of choice for most fMRI studies, allowing rapid volumetric coverage with minimum physiological artifacts. EPI is also the cornerstone of perfusion-based fMRI (9,12,13).

It was therefore desirable to implement EPI for fMRI studies on the 3T human system at the Institute for Biodiagnostics. However, modern "blipped" EPI requires gradient performance (~25 mT/m, 300μs rise time) that could not be met by the gradient system available at IBD during 1995 (~10 mT/m, 900μs rise time). An alternative EPI implementation consistent with available gradient performance was therefore developed.

A.2 METHODS

Instead of standard blipped EPI, a "slow-ramp" EPI sequence was developed according to the concept shown in Fig. B.2. The near-rectangular read gradient pulses of

blipped EPI were replaced with triangular waveforms requiring a lower slew rate from the gradient amplifiers. This allowed k-space to be covered in a single shot, but at the price of a more complicated k-space trajectory (Fig. B. 3).

Slow-ramp EPI was implemented at IBD in 1995 using the body gradients and quadrature RF head coil of a Magnex 3T whole-body magnet, and UXNMR software running on a Bruker Biospec console. The pulse program code, called "EPIB", is listed in Appendix B, and shown schematically in Fig. B.4. The resulting gradient waveforms are shown in Figs. A.5 and A.6 (Bruker "ramp time" parameter set to 900 μs). The read gradient cycle repeats 16 times, with 256 signal samples per cycle, giving a matrix size of 32 x 64.

Excellent shim (B0 field homogeneity) is critical for EPIB imaging. Therefore a supplementary sequence called EPISIM was created to aid magnet shimming before EPIB is run. EPISIM is a FLASH sequence with an extremely low-bandwidth readout that simulates the long, weak phase encode gradient of the EPIB sequence. Images acquired with EPISIM therefore suffer from the same inhomogeneity-related spatial distortions as EPIB images. Prior to acquisition of EPIB images, magnet shims are adjusted until acceptable quality EPISIM images are obtained.

EPIB images are acquired with both reconstruction and FID display turned OFF on the Bruker console. (Otherwise the console becomes overwhelmed by the high speed

of data acquisition.) As many as 1000 EPIB images can be acquired consecutively, with a TR time as little as 100 ms.

Because of the complex k-space trajectory of the sequence, image reconstruction is necessarily performed offline. After image data acquisition, FID data is moved from the Bruker console to "Zeno" (SGI Challenge XL server), and images are reconstructed with the IDL program "repi.pro" listed in Appendix C. (Another version, "repiangle.pro", is available for correcting residual spatial distortions after reconstruction.)

To perform image reconstruction, the nominal read gradient waveform (Fig. B.6) and phase encode gradient are integrated over time to obtain the floating point k-space coordinates of each of the 4096 data points acquired for a single image. (This process is termed "regridding".) The data point values are then added to the four adjacent integral-valued points in 32 x 64 k-space, weighted in proportion to their distance from each point (i.e. bilinear interpolation). A running total of weight factors for data summed into each k-space point is maintained and used to renormalize k-space at the end of the process. This is necessary because k-space is not sampled uniformly; points near edges in the read direction are oversampled (Fig. B.3). Finally, k-space is Fourier transformed to obtain the reconstructed image.

A.3 RESULTS AND DISCUSSION

Fig. B.7 shows a cross sectional image of a water bottle obtained with the EPIB sequence. A spatial resolution of 4 mm x 2 mm was achieved with a read gradient peak strength of 11.5 mT/m. Fig. B.7 also shows the importance of mapping data into k-space with the correct trajectory (regridding).

The residual ghosts in Fig. B.7 ("Nyquist ghosts") are ubiquitous in EPI. The ghosts are caused by data asymmetry in odd vs. even k-space lines. The asymmetry occurs because transient eddy currents following gradient pulses in the magnet bore create a difference in the positive vs. negative read gradient lobes, even though lobes are nominally identical (Fig. B.6). A phase adjustment parameter ("fid readout start") is available within the repi.pro reconstruction software to empirically minimize ghosting.

The EPIB sequence has been used successfully to image the human brain (Fig. B.8) and to obtain fMRI data (Fig. B.9). Unfortunately the sequence proved to be unsuitable for routine use. The extremely weak phase encode gradient (intrinsically related to the slow rate of read gradient switching) of approximately 0.1 mT/m, or 15 Hz/pixel, made the sequence pathologically sensitive to B0 field inhomogeneity. For example, at 3 Tesla an inhomogeneity of only 1 ppm would create a spatial distortion of more than 3 cm in EPIB images. Consequently it was necessary to manually adjust the

magnet shim for up to one hour before obtaining EPIB images in some cases. It was therefore concluded that the EPIB sequence was not practical for routine use.

REFERENCES

1. P. Mansfield, Multiplanar image formation using NMR spin echoes, *J. Phys. C* **10**, L55 (1977).

2. P. Mansfield, I. L. Pykett, Biological and Medical Imaging by NMR, *J. Magn. Reson.* **29**, 355 (1978).

3. M. Doyle, R. Turner, M. Crawley, et al, Real-time cardiac imaging of adults at video frame rates by magnetic resonance imaging, *Lancet* **2**, 682 (1986).

4. B. Chapman, R. Turner, R. J. Ordidge, et al, Real-time movie imaging from a single cardiac cycle by NMR, *Magn. Reson. Med.* **5**, 246 (1987).

5. A. M. Howesman, M. K. Stehling, B. Chapman, et al, Improvements in snapshot nuclear magnetic-resonance imaging, *Br. J. Radiol* **61**, 822 (1988).

6. R. Turner, D. Le Bihan, C. T. Moonen, D. Despres, J. Frank, Echo-planar time course MRI of cat brain oxygenation changes. *Magn. Res. Med.* **22**, 159-166 (1991).

7. J. W. Belliveau, D. N. Kennedy Jr., R. C. McKinstry, B. R. Buchbinder, R. M. Weisskoff, M. S. Cohen, J. M. Vevea, T. J. Brady, and B. R. Rosen, Functional mapping

of the human visual cortex by magnetic resonance imaging. *Science* **254**, 716-719 (1991).

8. P. A. Bandettini, E. C. Wong, R. S. Hinks, R. S. Tikofsky, J. S. Hyde, Time course EPI of human brain function during task activation. *Magn. Reson. Med.* **25**, 390-398 (1992).

9. K. K. Kwong, J. W. Belliveau, D. A. Chesler, I. E. Goldberg, R. M. Weisskoff, B. P. Poncelet, D. N. Kennedy, B. E. Hoppel, M. S. Cohen, R. Turner, Dynamic magnetic resonance imaging of human brain activity during primary sensory stimulation. *Proc. Natl. Acad. Sci. (USA)* **89(12)**, 5675-5679 (1992).

10. A. M. Blamire, S. Ogawa, K. Ugurbil, D. Rothman, G. McCarthy, J. M. Ellerman, F. Hyder, Z. Rattner, R. G. Shulman, Dynamic mapping of the human visual cortex by high-speed magnetic resonance imaging. *Proc. Natl. Acad. Sci. (USA)* **89**, 11069-11073 (1992).

11. R. Turner, P. Jezzard, H. Wen, K. K. Kwong, D. Le Bihan, T. Zeffiro, R. S. Balaban, Functional mapping of the human visual cortex at 4 and 1.5 Tesla using deoxygenation contrast EPI. *Magn. Reson. Med.* **29**, 277-279 (1993).

12. R. R. Edelman, B. Siewart, D. G. Garby, V. Thangaraj, A. C. Nobre, M. M. Mesulam, and S. Warach, Qualitative mapping of cerebral blood flow and functional localization

with echo-planar MR imaging and signal targeting with alternating radio frequency. *Radiology* **192**, 513-520 (1994).

13. S.-G. Kim, Quantification of relative cerebral blood flow change by flow-sensitive alternating inversion recovery (FAIR) technique: Application to functional mapping. *Magn. Reson. Med.* **34**, 293-301 (1995).

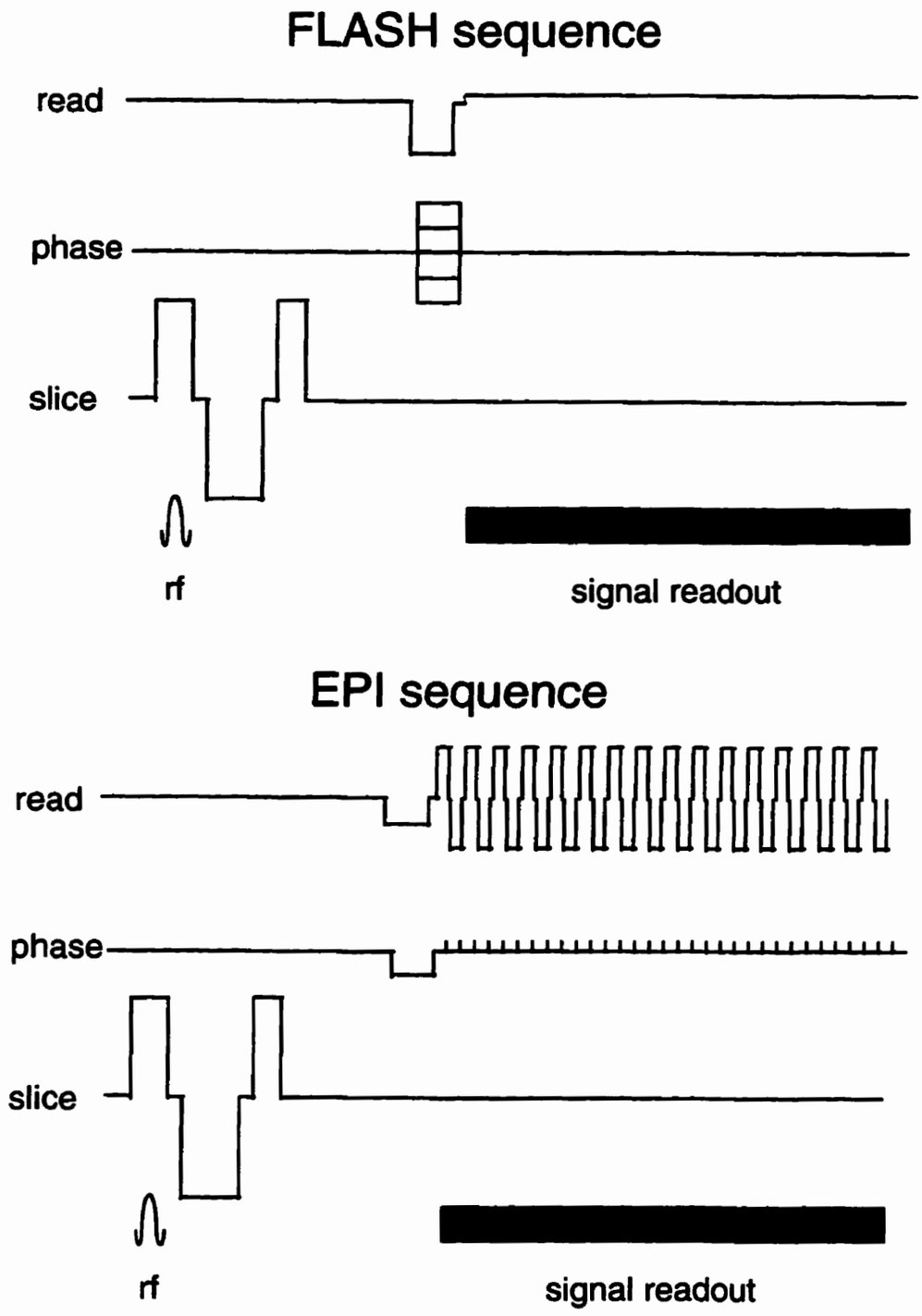

FIG. B.1 Gradients are rapidly switched during EPI imaging to sweep the acquired signal through all of k-space after one RF excitation, in contrast to FLASH imaging which only acquires one line of k-space.

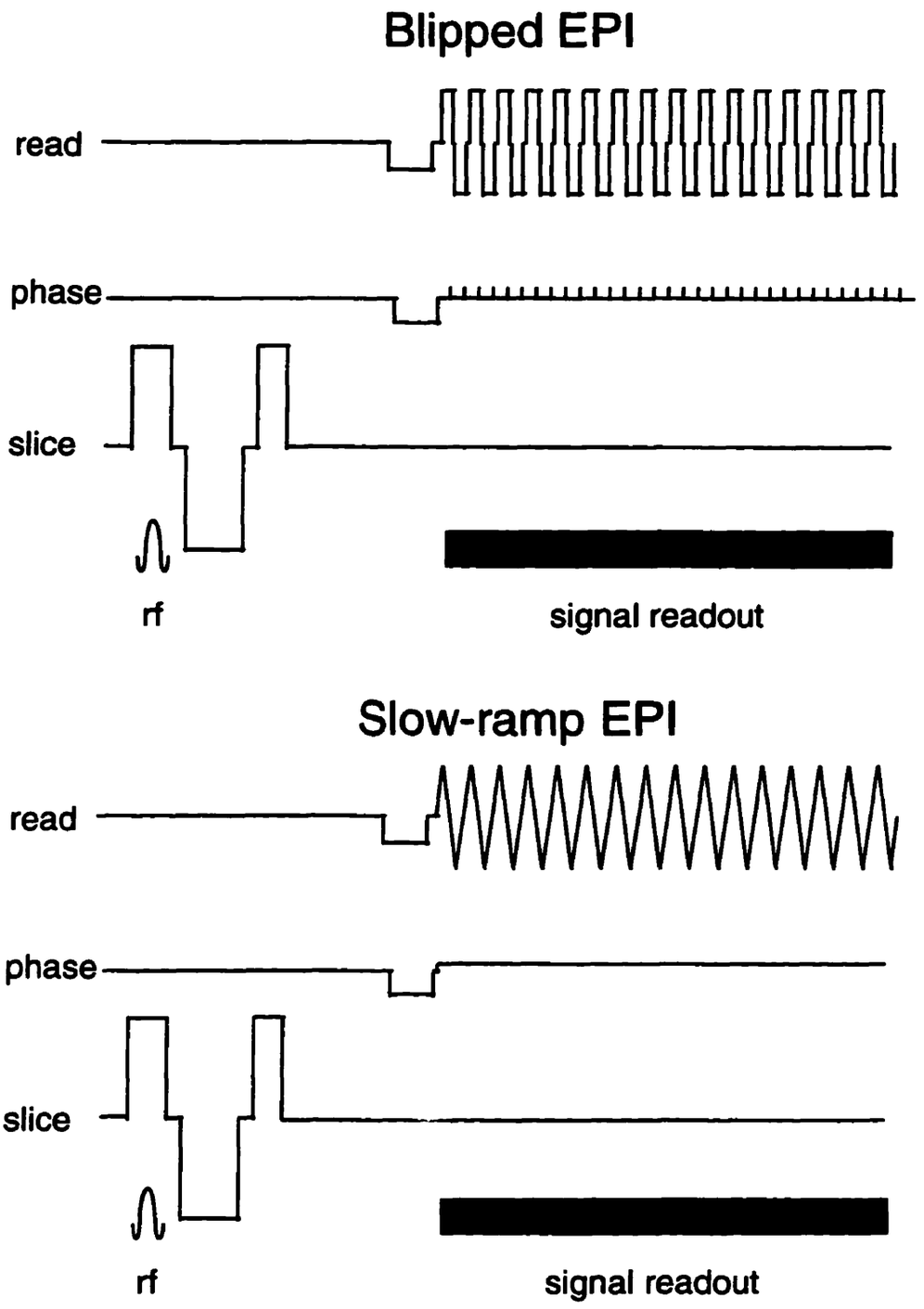

FIG. B.2 In blipped EPI, the phase encode gradient is "blipped" between read gradient steps, tracing a rectilinear path through k-space. In slow-ramp EPI, the phase encode gradient is held constant during read gradient oscillations, resulting in a more complicated path in k-space (Fig. B.3).

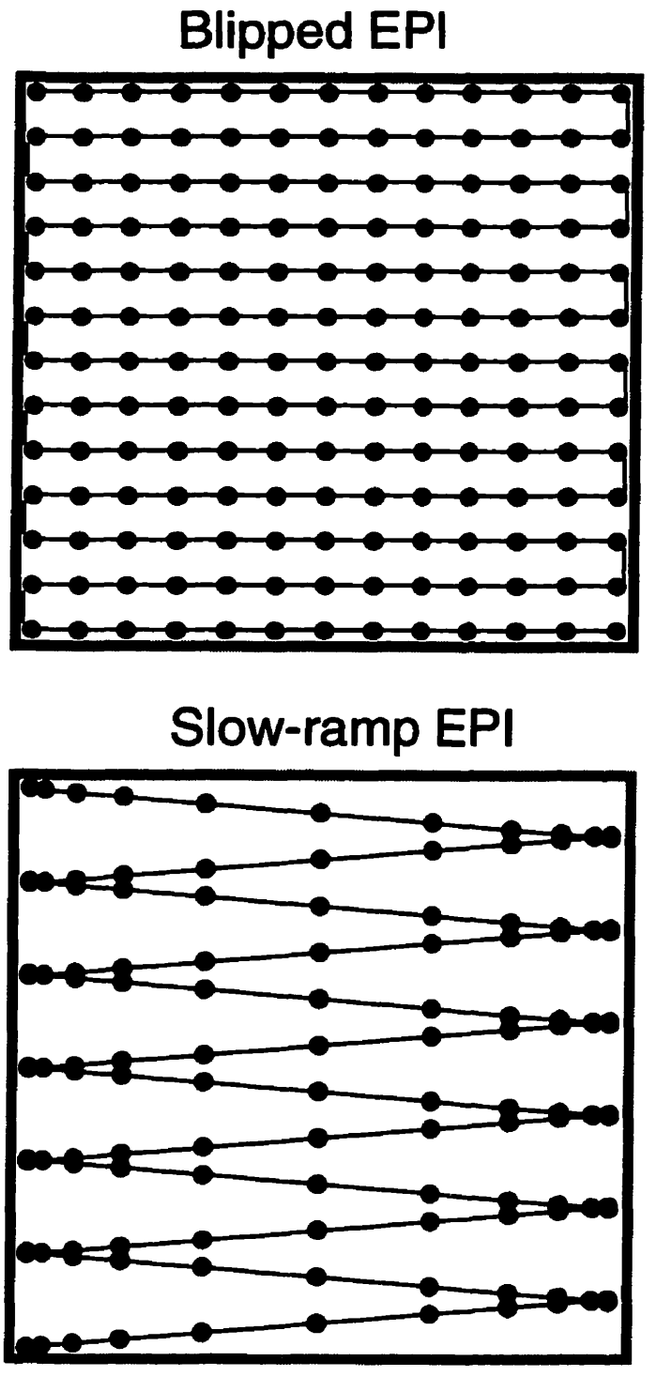

FIG. B.3 k-space trajectories of blipped EPI and slow-ramp EPI. The distribution of k-space points acquired during slow-ramp readout is not rectilinear, necessitating further digital processing ("regridding") before Fourier transforming to obtain the final image.

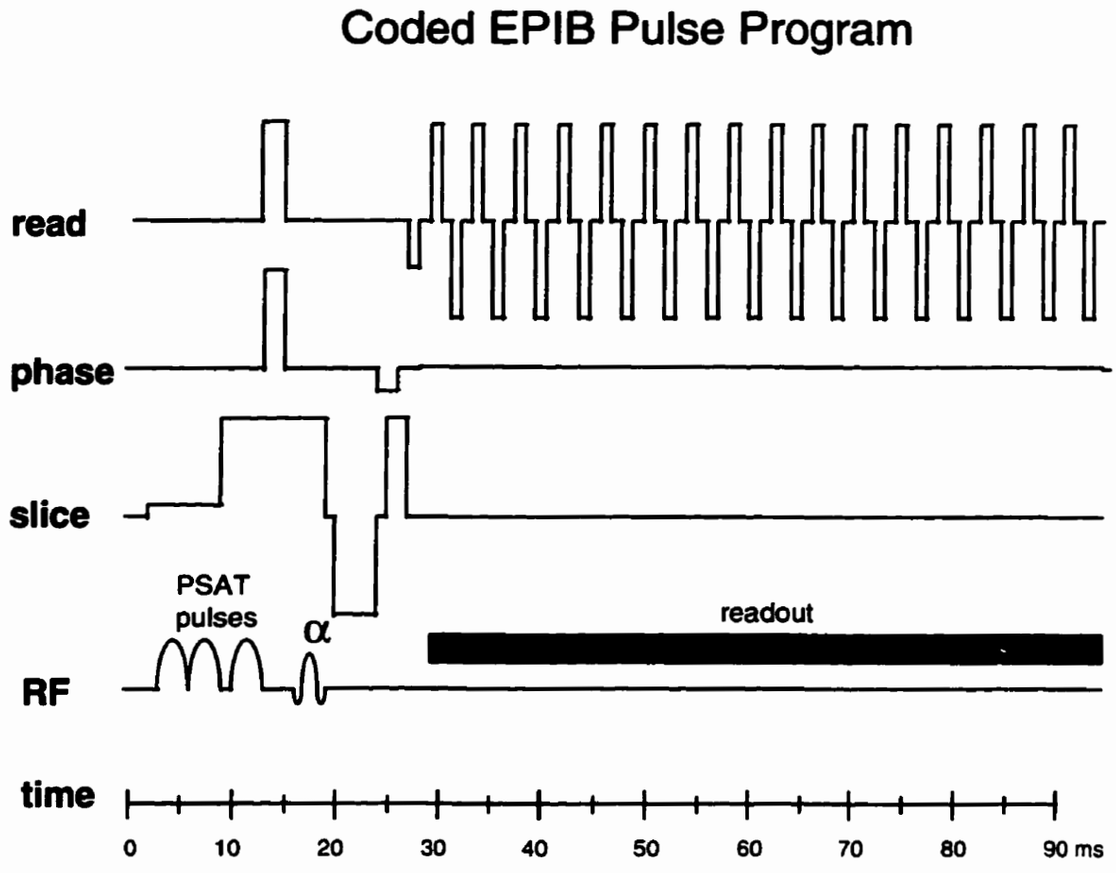

FIG. B.4 "EPIB" pulse program as coded by the author on the Bruker console for slow-ramp EPI. PSAT slice excitation was implemented as an option for the sequence.

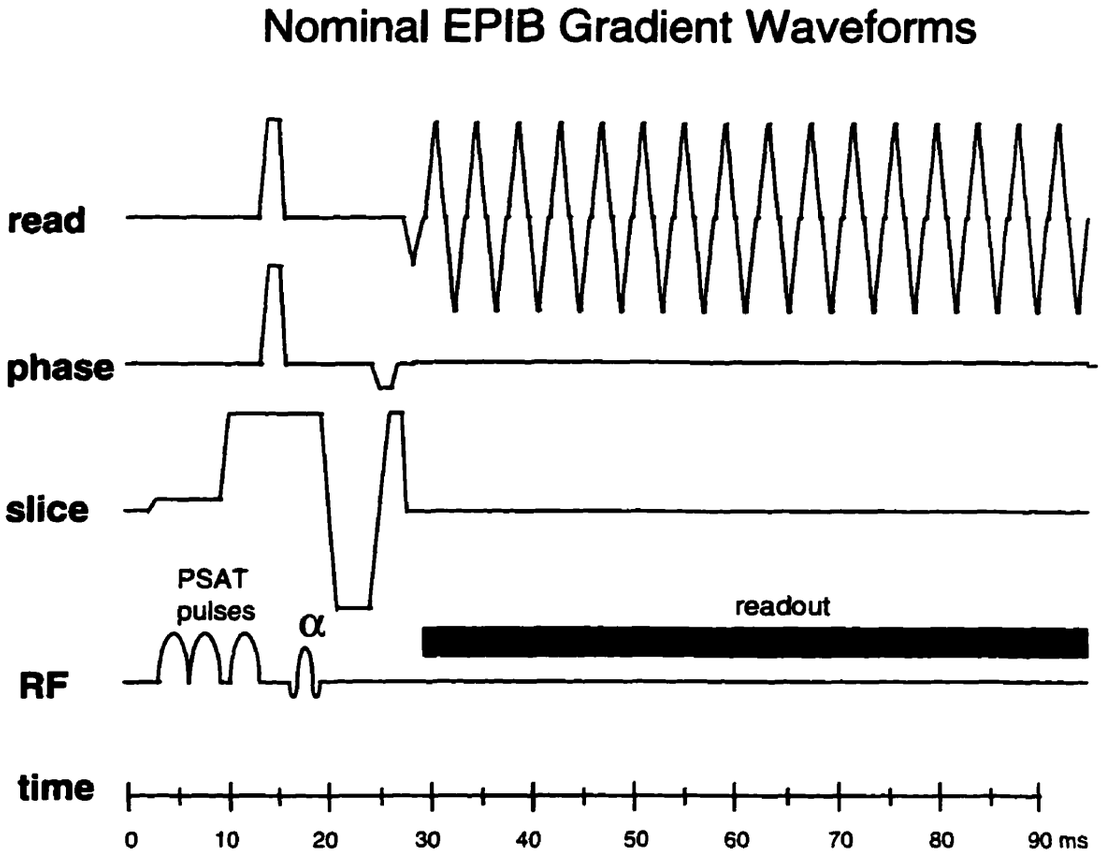

FIG. B.5 Gradient waveforms of the EPIB sequence (verified by oscilloscope measurement of amplifier output current). These waveforms differ from the coded pulse program because of the finite rise time (900 μs) of the gradient system.

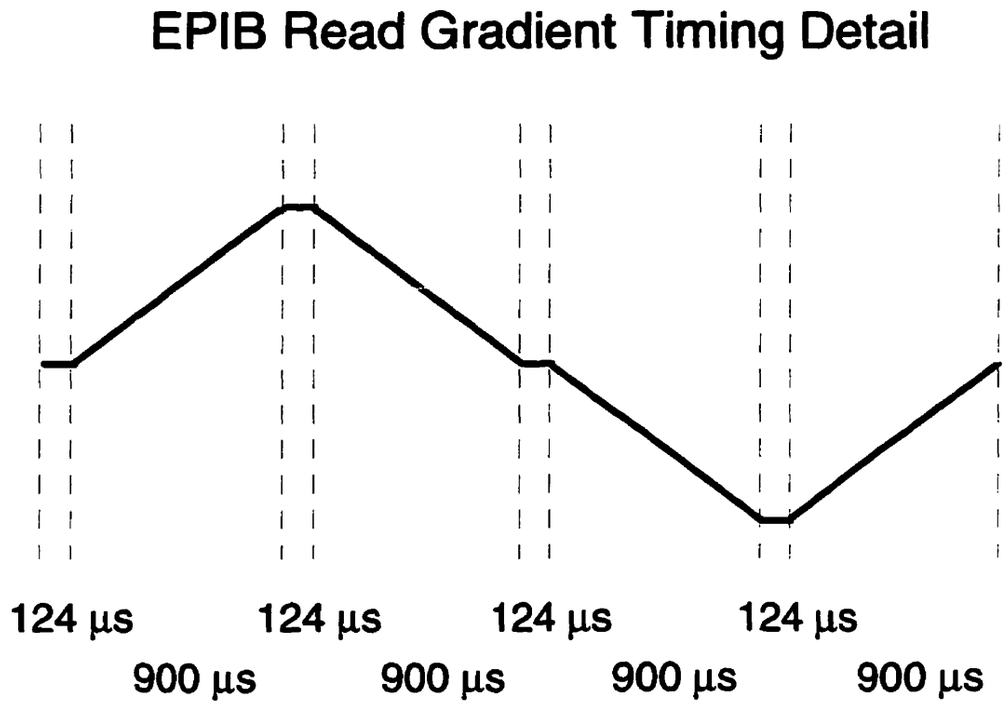

FIG. B.6 The EPIB sequence reads 32 lines of k-space by repeating the above read gradient pattern 16 times. 256 complex data points are acquired during each repetition at a bandwidth of 62.5 kHz (16 µs per complex point).

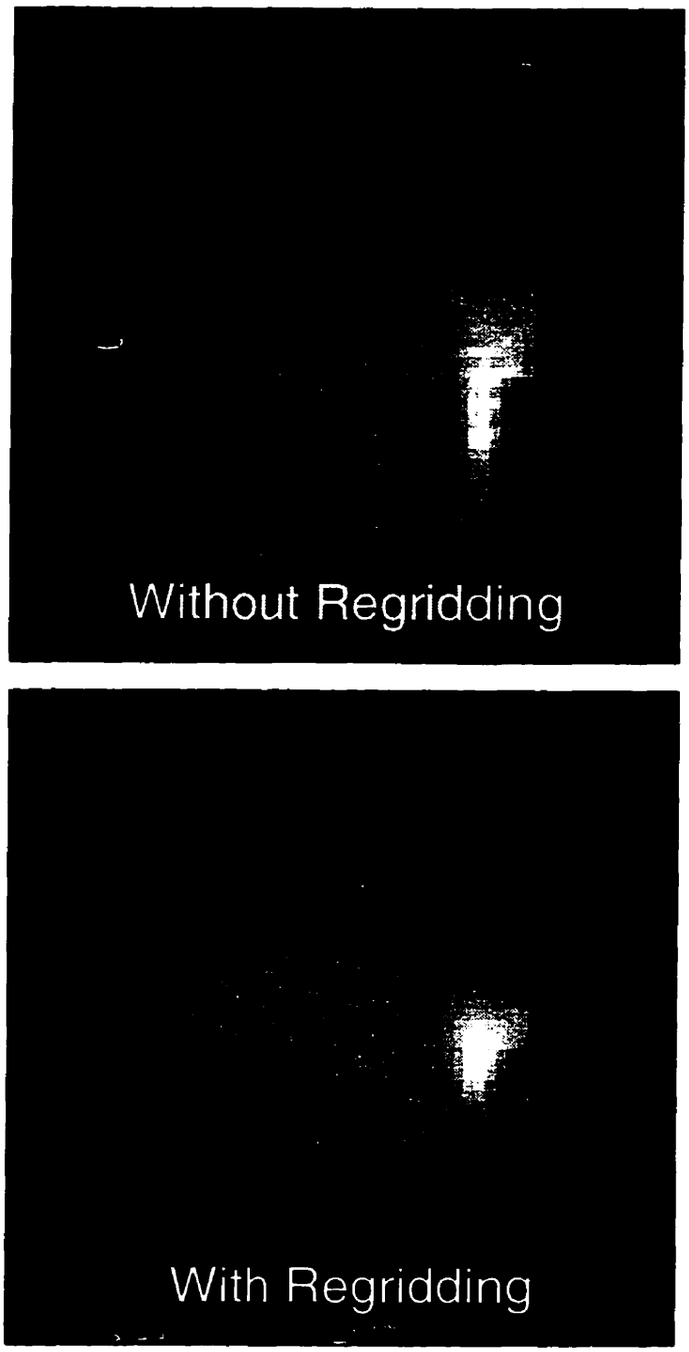

FIG. B.7 EPIB image of a water bottle (TE= 40 ms, FOV= 12.8 cm, 32 x 64 matrix) with and without regridding to compensate for non-rectilinear k-space trajectory. Remaining distortion in regridded image is due to B0 field inhomogeneity. Ghosting is due to gradient eddy currents.

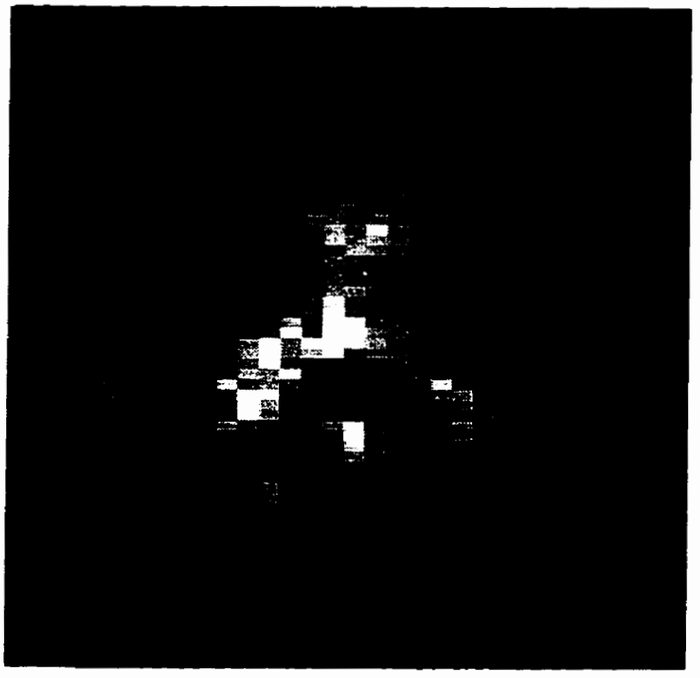

FIG. B.8 Single EPIB image of a human brain (TE= 40 ms, FOV= 17 cm, 32 x 64 matrix, $\alpha = 30°$).

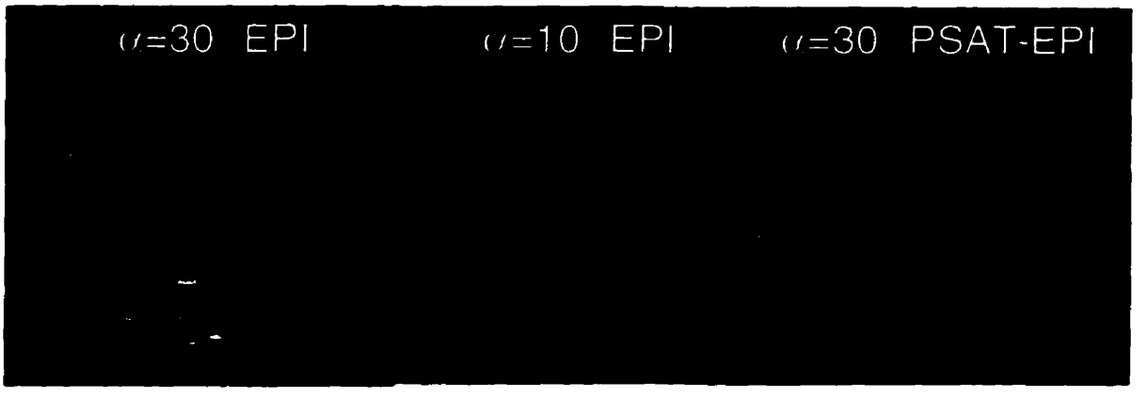

FIG. B.9 A visual activation study performed using the EPIB sequence. 1000 EPI images (TR/TE = 100/40 ms, 32 x 64 matrix, 17 cm FOV) of an oblique slice passing through the visual cortex were acquired contiguously over 100 seconds. The volunteer was exposed to 8 Hz alternating red/green visual stimulation for two 20 second periods interleaved with 20 second rest periods. The experiment was repeated three times. The first two trials were conventional EPI with 30° and 10° flip angles. The last trial was performed with α=30° PSAT slice excitation. Activations are shown as Student's T scores overlaid on an EPI brain image. The α=30° EPI experiment shows numerous flow-related activations which are absent in the reduced flip-angle EPI and PSAT-EPI experiments.

Appendix C

IDL COMPUTER PROGRAM CODES

C.1 IMAGE RECONSTRUCTION CODE

The "nophys.pro" program reads Bruker FID data in 2 byte integer format (i.e. files created by the "compress" option of Jie Shen's xrcp file transfer program), and reconstructs images by simple Fourier transform. As far as can be determined, the resulting images are identical to that produced by the Bruker console itself.

Note that the program takes special steps to remove DC signal offsets (that would cause baseline artifacts) by subtracting a signal average obtained near the edges of k-space, where the signal is nominally zero. The program also corrects for the peculiar Bruker "qseq" acquisition mode, in which a single ADC is apparently used in an interleaved mode to digitize the real and imaginary signal components. (The real and imaginary components are thus temporally misregistered by 1/2 dwell time.) This is corrected for by a sinc interpolation of the imaginary data.

```
;nophys.pro
;IDL FLASH image reconstruction program with no physio correction
;by Brian Wowk, Jan. 1996

;Reconstructs 256 x 128 images (Read extension factor 2)
;from Bruker fid files

!ORDER=1

images=35               ;number of images in dataset
groupsize=7             ;number of images in each group

rshift=128              ;reduced FOV reco shift

k=COMPLEXARR(512,128)         ;k space (including navigator)
pcorr=FLTARR(128,images)      ;phase correction list
pcorra=FLTARR(128)            ;average phase correction

kift =COMPLEXARR(512)         ;FT of single ki line
lkift=COMPLEXARR(1024)        ;zero-filled expansion of kift
lki  =FLTARR(1024)            ;sinc interpolated version of ki

an   =INTARR(1024,128)

pi=acos(-1)             ;pi
pi2=2*pi                ;2 pi
degrad=180.0/pi               ;radians to degrees conversion

OPENR,1,'fid'                 ;open fid (short integer)
a=ASSOC(1,INTARR(1024,128))

OPENW,2,'pdata/1/2dseq'       ;open reconstructed image file
b=ASSOC(2,FLTARR(128,256))

baseline=COMPLEX(0,0)

FOR image=0,images-1 DO BEGIN ;compute ADC baseline
an=a(image)
BYTEORDER,an                  ;swap byte order (Bruker -> Zeno)

FOR i=0,511 DO k(i,*)=COMPLEX(an(i*2,*),an(i*2+1,*))
```

```
baseline=baseline+TOTAL(k(1:40,40:79))/1600
END                              ;compute ADC baseline
                                 ;from edge of k space

baseline=baseline/(images)

WINDOW,0,XSIZE=512,YSIZE=128

FOR image=0,images-1 DO BEGIN       ;count through images
print,'Reconstructing image',image

an=a(image)
BYTEORDER,an                     ;swap byte order (Bruker -> Zeno)

FOR i=0,511 DO k(i,*)=COMPLEX(an(i*2,*),an(i*2+1,*))

k=k-baseline                     ;baseline correction

kr=FLOAT(k)              ;real part of k space
ki=IMAGINARY(k)                  ;imaginary part of k space

FOR j=0,127 DO BEGIN             ;correction for qseq ADC mode

      kift=FFT(ki(*,j),1)              ;FT of a ki line
      lkift(*)=0.0
      lkift(0:255)=kift(0:255)
      lkift(768:1023)=kift(256:511) ;zero-padded expansion
      lki=FFT(lkift,-1)          ;FT back to larger size
      lki=SHIFT(lki,1)           ;shift to get sinc interp
      ki(*,j)=lki(INDGEN(512)*2)*2  ;interp values back to ki

END

k=COMPLEX(kr,ki)

WINDOW,0,XSIZE=512,YSIZE=128
TVSCL,ABS(k)                ;display signal magnitude image

WINDOW,1,XSIZE=512,YSIZE=128
p=ATAN(ki,kr)               ;k space phase angle

TVSCL,p

FOR i=0,127 DO BEGIN     ;recompute k space with new phase

      row=k(*,i)
      row=ABS(row)*COMPLEX(COS(p(*,i)),SIN(p(*,i)))
      k(*,i)=row
END

nk=k(0:511,*)      ;true k space image data

r=ABS(FFT(nk,1))           ;magnitude image
rf=SHIFT(r,256,64)         ;shift to center

f=rf(rshift:rshift+255,*)    ;get rid of read extension margins

f=ROTATE(f,4)              ;adjust orientation

b(image)=f          ;write reconstructed image
```

```
EXPAND,f,256,256,fx

WINDOW,2,XSIZE=256,YSIZE=256
TVSCL,fx          ;reconstructed image display

END

CLOSE,1,2

END
```

C.2 K-SPACE PHASE CORRECTION CODE

The "physdat.pro" program reads Bruker FID data in 2 byte integer format, and reconstructs images after performing a "k-space phase correction" as described in Chapter 4. A variation of the program, "physgr.pro", performs a k-space phase correction within each image group individually. In some cases, particularly if large motion is present, physgr.pro may give a better result than physdat.pro.

In May, 1997, an 8th order Butterworth filter was added to reduce Gibb's ringing in final reconstructed images.

```
;physdat.pro
;IDL FLASH image reconstruction program with physio correction
;by Brian Wowk, Jan. 1996

;Reconstructs 256 x 128 images (Read extension factor 2)
;from Bruker fid files

;Corrects for physiologic fluctuations using k space data only
;Creates phase variation data file
;Corrects for phase wrap errors

!ORDER=1

images=60               ;number of images in dataset
groupsize=6             ;number of images in each group

Print,'File contains: ',STRCOMPRESS(images, /REMOVE_ALL),' images and
has a groupsize of ', $
   STRCOMPRESS(groupsize, /REMOVE_ALL)

rshift=128              ;reduced FOV reco shift

k=COMPLEXARR(512,128)         ;k space (including navigator)
pcorr=FLTARR(128,images)      ;phase correction list
pcorra=FLTARR(128)            ;average phase correction

pv=FLTARR(128*images)         ;plot vector for k-space phase

kift =COMPLEXARR(512)         ;FT of single ki line
lkift=COMPLEXARR(1024)        ;zero-filled expansion of kift
lki  =FLTARR(1024)            ;sinc interpolated version of ki

an   =INTARR(1024,128)

fil  =FLTARR(128)       ;filter to remove Gibb's ringing
FOR i=0,63 DO BEGIN           ;8th order Butterworth
      fil(64+i)=1.0/(1.0 + (i/55.0)^16)
      fil(63-i)=fil(64+i)
END

pi=acos(-1)             ;pi
pi2=2*pi                ;2 pi
degrad=180.0/pi               ;radians to degrees conversion

OPENR,1,'fid'                 ;open fid (short integer)
a=ASSOC(1,INTARR(1024,128))
```

```
OPENW,2,'pdata/1/2dcorrf'      ;open reconstructed image file
b=ASSOC(2,FLTARR(128,256))

baseline=COMPLEX(0,0)

FOR image=0,images-1 DO BEGIN ;compute ADC baseline
an=a(image)
BYTEORDER,an                   ;swap byte order (Bruker -> Zeno)

FOR i=0,511 DO k(i,*)=COMPLEX(an(i*2,*),an(i*2+1,*))

baseline=baseline+TOTAL(k(1:40,40:79))/1600
END                           ;compute ADC baseline
                              ;from edge of k space

baseline=baseline/(images)

pcorr(*,*)=0.0
inum=0
FOR image=0,images-1 DO BEGIN ;get phase correction list

IF (image MOD groupsize) NE 0 THEN BEGIN
inum=inum+1
PRINT,'Getting phase list for image ',image
an=a(image)
BYTEORDER,an                   ;swap byte order (Bruker -> Zeno)

FOR i=0,511 DO k(i,*)=COMPLEX(an(i*2,*),an(i*2+1,*))

k=k-baseline                   ;baseline correction

kr=FLOAT(k)              ;real part of k space
ki=IMAGINARY(k)                ;imaginary part of k space

FOR j=0,127 DO BEGIN           ;correction for qseq ADC mode

      kift=FFT(ki(*,j),1)            ;FT of a ki line
      lkift(*)=0.0
      lkift(0:255)=kift(0:255)
      lkift(768:1023)=kift(256:511) ;zero-padded expansion
      lki=FFT(lkift,-1)        ;FT back to larger size
      lki=SHIFT(lki,1)         ;shift to get sinc interp
      ki(*,j)=lki(INDGEN(512)*2)*2  ;interp values back to ki

END

k=COMPLEX(kr,ki)
p=ATAN(ki,kr)            ;k space phase angle

;WINDOW,0,XSIZE=512,YSIZE=128
;tvscl,p

IF image EQ 1 THEN p1=p

pd=p-p1            ;difference from phase of first image
th=2.0             ;set maximum expected phase difference (radians)

;fix phase wraps
pd(*,*)=pd(*,*) + (pd(*,*) LE -th)*pi2 - (pd(*,*) GE th)*pi2
```

```
m=ABS(k)                    ;k-space magnitude (weight factor)
m=(ABS(pd(*,*)) LT th)*m      ;set to zero if phase diff too big

;WINDOW,1,XSIZE=512,YSIZE=128
;TVSCL,pd

FOR i=0,127 DO BEGIN
      n=0
      FOR j=0,511 DO BEGIN
            IF pd(j,i) GT -2.0 THEN BEGIN
                  pcorr(i,image)=pcorr(i,image)+pd(j,i)*m(j,i)
                  n=n+m(j,i)
            END
      END
      IF n GT 0 THEN pcorr(i,image)=pcorr(i,image)/n
;     print,n,pcorr(i,image)
END

END
END

FOR i=0,127 DO pcorra(i)=total(pcorr(i,*))/inum

FOR i=0,127 DO FOR j=0,images-1 DO pv(i+j*128)=pcorr(i,j)-pcorra(i)

OPENW,3,'phase.dat'
FOR i=1*128,images*128-1 DO printf,3,i-1*128,pv(i)
CLOSE,3

FOR image=0,images-1 DO BEGIN       ;count through images
print,'Reconstructing image',image

an=a(image)
BYTEORDER,an                  ;swap byte order (Bruker -> Zeno)

FOR i=0,511 DO k(i,*)=COMPLEX(an(i*2,*),an(i*2+1,*))

k=k-baseline                  ;baseline correction

kr=FLOAT(k)             ;real part of k space
ki=IMAGINARY(k)               ;imaginary part of k space

FOR j=0,127 DO BEGIN          ;correction for qseq ADC mode

      kift=FFT(ki(*,j),1)           ;FT of a ki line
      lkift(*)=0.0
      lkift(0:255)=kift(0:255)
      lkift(768:1023)=kift(256:511) ;zero-padded expansion
      lki=FFT(lkift,-1)       ;FT back to larger size
      lki=SHIFT(lki,1)        ;shift to get sinc interp
      ki(*,j)=lki(INDGEN(512)*2)*2  ;interp values back to ki

END

k=COMPLEX(kr,ki)

;WINDOW,0,XSIZE=512,YSIZE=128
;TVSCL,ABS(k)           ;display signal magnitude image

;WINDOW,1,XSIZE=512,YSIZE=128
p=ATAN(ki,kr)           ;k space phase angle
```

```
FOR j=0,511 DO BEGIN                ;phase correction
      p(j,*)=p(j,*)-(pcorr(*,image)-pcorra(*))
END

;TVSCL,p

FOR i=0,127 DO BEGIN    ;recompute k space with new phase

      row=k(*,i)
      row=ABS(row)*COMPLEX(COS(p(*,i)),SIN(p(*,i)))
      k(*,i)=row
END

nk=k(0:511,*)     ;k space image data

FOR i=0,511 DO nk(i,*)=nk(i,*)*fil(*)     ;apply ringing filter

r=ABS(FFT(nk,1))          ;magnitude image
rf=SHIFT(r,256,64)        ;shift to center

f=rf(rshift:rshift+255,*)   ;get rid of read extension margins

f=ROTATE(f,4)             ;adjust orientation

b(image)=f          ;write reconstructed image

;EXPAND,f,256,256,fx

;WINDOW,2,XSIZE=256,YSIZE=256
;TVSCL,fx          ;reconstructed image display

END

CLOSE,1,2

END
```

C.3 K-SPACE ORTHOGONALIZATION CODE

The "physkom.pro" program reads Bruker FID data in 2 byte integer format, and reconstructs images after performing a "k-space orthogonalization" correction as described in Chapter 4. A variation of the program, "physkomp.pro", performs a Gram-Schmidt orthogonalization on respiratory and cardiac physiology components independently.

```
;physkom.pro
;IDL FLASH image reconstruction program with physio correction
;by Brian Wowk, Jan. 1997

;Reconstructs 256 x 128 images (Read extension factor 2)
;from Bruker fid files

;Corrects for physiologic fluctuations using k space data only
;Creates phase variation data file
;Corrects for phase wrap errors

;Performs k-space phase variation orthogonalization
; on phase and magnitude data

!ORDER=1

images=42               ;number of images in dataset
groupsize=42                  ;number of images in each group

rshift=128              ;reduced FOV reco shift

k=COMPLEXARR(512,128)         ;k space (including navigator)
pcorr=FLTARR(128,images)      ;phase correction list
pcorra=FLTARR(128)            ;average phase correction

avpd=FLTARR(512,128)          ;average k-space phase var
prod=FLTARR(512,128)          ;inner product of k-space phase var
prodm=FLTARR(512,128)
avmag=FLTARR(512,128)

aref=FLTARR(128,images)       ;reference phase var vector
anorm=FLTARR(128)       ;normalization coefficients

pv=FLTARR(128*images)         ;plot vector for k-space phase

kift =COMPLEXARR(512)         ;FT of single ki line
lkift=COMPLEXARR(1024)        ;zero-filled expansion of kift
lki  =FLTARR(1024)            ;sinc interpolated version of ki

an   =INTARR(1024,128)

fil  =FLTARR(128)       ;filter to remove Gibb's ringing
FOR i=0,63 DO BEGIN           ;8th order Butterworth
      fil(64+i)=1.0/(1.0 + (i/55.0)^16)
      fil(63-i)=fil(64+i)
END

pi=acos(-1)             ;pi
pi2=2*pi                ;2 pi
degrad=180.0/pi               ;radians to degrees conversion
```

```
OPENR,1,'fid'                    ;open fid (short integer)
a=ASSOC(1,INTARR(1024,128))

OPENW,2,'pdata/1/2dkomf'         ;open reconstructed image file
b=ASSOC(2,FLTARR(128,256))

baseline=COMPLEX(0,0)

FOR image=0,images-1 DO BEGIN ;compute ADC baseline
an=a(image)
BYTEORDER,an                     ;swap byte order (Bruker -> Zeno)

FOR i=0,511 DO k(i,*)=COMPLEX(an(i*2,*),an(i*2+1,*))

baseline=baseline+TOTAL(k(1:40,40:79))/1600
END                              ;compute ADC baseline
                                 ;from edge of k space

baseline=baseline/(images)

avpd(*,*)=0.0
avmag(*,*)=0.0
pcorr(*,*)=0.0
inum=0
FOR image=0,images-1 DO BEGIN ;Pass ONE: get phase var and avpd

IF (image MOD groupsize) NE 0 THEN BEGIN
inum=inum+1
PRINT,'Getting phase list for image ',image
an=a(image)
BYTEORDER,an                     ;swap byte order (Bruker -> Zeno)

FOR i=0,511 DO k(i,*)=COMPLEX(an(i*2,*),an(i*2+1,*))

k=k-baseline                     ;baseline correction

kr=FLOAT(k)              ;real part of k space
ki=IMAGINARY(k)                  ;imaginary part of k space

FOR j=0,127 DO BEGIN             ;correction for qseq ADC mode

      kift=FFT(ki(*,j),1)              ;FT of a ki line
      lkift(*)=0.0
      lkift(0:255)=kift(0:255)
      lkift(768:1023)=kift(256:511) ;zero-padded expansion
      lki=FFT(lkift,-1)          ;FT back to larger size
      lki=SHIFT(lki,1)           ;shift to get sinc interp
      ki(*,j)=lki(INDGEN(512)*2)*2  ;interp values back to ki

END

k=COMPLEX(kr,ki)
p=ATAN(ki,kr)            ;k space phase angle

;WINDOW,0,XSIZE=512,YSIZE=128
;tvscl,p

IF image EQ 1 THEN p1=p

pd=p-p1             ;difference from phase of first image
th=3.0              ;set maximum expected phase difference (radians)
```

```
;fix phase wraps
pd(*,*)=pd(*,*) + (pd(*,*) LE -th)*pi2 - (pd(*,*) GE th)*pi2

m=ABS(k)                    ;k-space magnitude (weight factor)
avmag=avmag+m
m=(ABS(pd(*,*)) LT th)*m      ;set to zero if phase diff too big

;WINDOW,1,XSIZE=512,YSIZE=128
;TVSCL,pd

avpd=avpd+pd

FOR i=0,127 DO BEGIN
      n=0
      FOR j=0,511 DO BEGIN
            pcorr(i,image)=pcorr(i,image)+pd(j,i)*m(j,i)
            n=n+m(j,i)
      END
      IF n GT 0 THEN pcorr(i,image)=pcorr(i,image)/n
      print,n,pcorr(i,image)
END

END
END
avpd=avpd/inum
avmag=avmag/inum

FOR i=0,127 DO pcorra(i)=TOTAL(pcorr(i,*))/inum
FOR i=0,127 DO aref(i,*)=pcorr(i,*)-pcorra(i)   ;compute ref vector
FOR i=0,127 DO anorm(i)=TOTAL(aref(i,*)*aref(i,*))

FOR i=0,127 DO FOR j=0,images-1 DO pv(i+j*128)=pcorr(i,j)-pcorra(i)

OPENW,3,'phasetmp.dat'
FOR i=1*128,images*128-1 DO printf,3,i-1*128,pv(i)
CLOSE,3


prod(*,*)=0.0
inum=0
FOR image=0,images-1 DO BEGIN ;Pass TWO: get phase var and avpd

IF (image MOD groupsize) NE 0 THEN BEGIN
inum=inum+1
PRINT,'Getting phase list for image ',image
an=a(image)
BYTEORDER,an                  ;swap byte order (Bruker -> Zeno)

FOR i=0,511 DO k(i,*)=COMPLEX(an(i*2,*),an(i*2+1,*))

k=k-baseline                  ;baseline correction

kr=FLOAT(k)             ;real part of k space
ki=IMAGINARY(k)               ;imaginary part of k space

FOR j=0,127 DO BEGIN          ;correction for qseq ADC mode

      kift=FFT(ki(*,j),1)           ;FT of a ki line
      lkift(*)=0.0
      lkift(0:255)=kift(0:255)
```

```
      lkift(768:1023)=kift(256:511) ;zero-padded expansion
      lki=FFT(lkift,-1)       ;FT back to larger size
      lki=SHIFT(lki,1)        ;shift to get sinc interp
      ki(*,j)=lki(INDGEN(512)*2)*2  ;interp values back to ki

END

k=COMPLEX(kr,ki)
m=ABS(k)          ;k-space magnitude
p=ATAN(ki,kr)           ;k space phase angle

;WINDOW,0,XSIZE=512,YSIZE=128
;tvscl,p

IF image EQ 1 THEN p1=p

pd=p-p1           ;difference from phase of first image
th=3.0            ;set maximum expected phase difference (radians)

;fix phase wraps
pd(*,*)=pd(*,*) + (pd(*,*) LE -th)*pi2 - (pd(*,*) GE th)*pi2

;WINDOW,1,XSIZE=512,YSIZE=128

pd=pd-avpd
pd(*,*)=pd(*,*) + (pd(*,*) LE -th)*pi2 - (pd(*,*) GE th)*pi2

FOR i=0,127 DO prod(*,i)=prod(*,i)+aref(i,image)*pd(*,i)
FOR i=0,127 DO BEGIN
      prodm(*,i)=prodm(*,i)+aref(i,image)*(m(*,i)-avmag(*,i))
END

;TVSCL,pd

END
END


FOR image=0,images-1 DO BEGIN       ;Pass THREE: correct images
print,'Reconstructing image',image

an=a(image)
BYTEORDER,an                  ;swap byte order (Bruker -> Zeno)

FOR i=0,511 DO k(i,*)=COMPLEX(an(i*2,*),an(i*2+1,*))

k=k-baseline                  ;baseline correction

kr=FLOAT(k)             ;real part of k space
ki=IMAGINARY(k)               ;imaginary part of k space

FOR j=0,127 DO BEGIN          ;correction for qseq ADC mode

      kift=FFT(ki(*,j),1)           ;FT of a ki line
      lkift(*)=0.0
      lkift(0:255)=kift(0:255)
      lkift(768:1023)=kift(256:511) ;zero-padded expansion
      lki=FFT(lkift,-1)       ;FT back to larger size
      lki=SHIFT(lki,1)        ;shift to get sinc interp
      ki(*,j)=lki(INDGEN(512)*2)*2  ;interp values back to ki
```

```
END

k=COMPLEX(kr,ki)
m=ABS(k)

;WINDOW,0,XSIZE=512,YSIZE=128
;TVSCL,m                 ;display signal magnitude image

;WINDOW,1,XSIZE=512,YSIZE=128
p=ATAN(ki,kr)            ;k space phase angle

aref(*,image)=aref(*,image)/anorm(*)      ;normalize ref vector

FOR i=0,127 DO p(*,i)=p(*,i)-aref(i,image)*prod(*,i)
FOR i=0,127 DO m(*,i)=m(*,i)-aref(i,image)*prodm(*,i)

;TVSCL,p

FOR i=0,127 DO BEGIN     ;recompute k space with new phase

      row=COMPLEX(m(*,i),0)
      row=ABS(row)*COMPLEX(COS(p(*,i)),SIN(p(*,i)))
      k(*,i)=row
END

nk=k(0:511,*)      ;k space image data

FOR i=0,511 DO nk(i,*)=nk(i,*)*fil(*)      ;apply ringing filter

r=ABS(FFT(nk,1))         ;magnitude image
rf=SHIFT(r,256,64)       ;shift to center

f=rf(rshift:rshift+255,*)    ;get rid of read extension margins

f=ROTATE(f,4)            ;adjust orientation

b(image)=f         ;write reconstructed image

EXPAND,f,256,256,fx

;WINDOW,2,XSIZE=256,YSIZE=256
;TVSCL,fx          ;reconstructed image display

END

CLOSE,1,2

END
```

C.4 IMAGE REGISTRATION CODE

The "ufreg.pro" program performs Fourier domain image registration as described in Chapter 5.

```
;UFREG.PRO
;IDL Image Registration Program
;By Brian Wowk, Feb. 1995
;New general matrix size version, Apr. 1997

!ORDER=1                        ;Set image orientation

mx=128                                ;image matrix size
my=256

OPENR,1,'2dkom'                       ;Open old image file
OPENW,2,'test'                  ;Registered images
OPENW,3,'reg2'                        ;Registration results

old_images=ASSOC(1,FLTARR(mx,my))
new_images=ASSOC(2,FLTARR(mx,my))
a=fstat(1)                      ;file statistics

images=a.size/(FLOAT(mx) * FLOAT(my) * 4.0) ;total number of images

merit=fltarr(100)               ;figure of merit
angle=fltarr(100)               ;trial rotation angles
xshft=fltarr(100)               ;best x shift for rotation
yshft=fltarr(100)               ;best y shift for rotation

sbim=sobel(old_images(1)*255/max(old_images(1))) ;edge enhanced image

FOR regnum=0,images-1 DO BEGIN            ;register all images

xs=128                                ;image expansion scale
EXPAND,old_images(1),xs,xs,ref_image      ;registration reference image
ref_kernel=CONJ(FFT(ref_image,1))   ;Fourier correlation kernel
EXPAND,old_images(regnum),xs,xs,rhold     ;image to register
merit(*)=-1e30                  ;initialize merit array
dthnum=0

FOR dth=-10.0,+10.0,1.0 DO BEGIN          ;trial rotations
      dthnum=dthnum+1                     ;trial rotation count
      regim=ROT(rhold,360+dth,/INTERP)

      c=FFT(FFT(regim,1)*ref_kernel,-1)   ;Cross correlate in
                                    ;Fourier domain
      cmax=MAX(c,p)                       ;Find correlation maximum

      xshift=p MOD xs                     ;compute image shift
      IF xshift GT xs/2 THEN xshift=xshift-xs   ;check for 2's
complement
      yshift=p/xs
      IF yshift GT xs/2 THEN yshift=yshift-xs

      newim=ROT(regim,0,1,xs/2+xshift,xs/2+yshift)
      expand,newim,mx,my,scnew            ;reduce to original scale

      ss1=total((newim-ref_image)^2)            ;sum squared differences
```

```
      ss2=total(sbim*(scnew-old_images(1))^2)    ;edge-weighted sq. diff
                                    ;on original image scale
      merit(dthnum)=-ss2
      angle(dthnum)=dth
      xshft(dthnum)=xshift
      yshft(dthnum)=yshift


      print,dth,cmax,ss1,ss2,xshift,yshift

;     TVSCL,abs(newim - ref_image)
      END

      bestmerit=max(merit,p)
      print
      print,xs,angle(p),xshft(p),yshft(p),bestmerit
      print
      ang=angle(p)

xs=256                              ;image expansion scale
EXPAND,old_images(1),xs,xs,ref_image      ;registration reference image
ref_kernel=CONJ(FFT(ref_image,1))   ;Fourier correlation kernel
EXPAND,old_images(regnum),xs,xs,rhold     ;image to register
merit(*)=-1e30                      ;initialize merit array
dthnum=0

FOR dth=ang-0.5,ang+0.51,0.5 DO BEGIN          ;trial rotations
      dthnum=dthnum+1                     ;trial rotation count
      regim=ROT(rhold,360+dth,/INTERP)

      c=FFT(FFT(regim,1)*ref_kernel,-1)   ;Cross correlate in
                                    ;Fourier domain
      cmax=MAX(c,p)                       ;Find correlation maximum

      xshift=p MOD xs                     ;compute image shift
      IF xshift GT xs/2 THEN xshift=xshift-xs   ;check for 2's
complement
      yshift=p/xs
      IF yshift GT xs/2 THEN yshift=yshift-xs

      newim=ROT(regim,0,1,xs/2+xshift,xs/2+yshift)
      expand,newim,mx,my,scnew            ;reduce to original scale

      ss1=total((newim-ref_image)^2)            ;sum squared differences
      ss2=total(sbim*(scnew-old_images(1))^2)   ;edge-weighted sq. diff
                                    ;on original image scale
      merit(dthnum)=-ss2
      angle(dthnum)=dth
      xshft(dthnum)=xshift
      yshft(dthnum)=yshift


      print,dth,cmax,ss1,ss2,xshift,yshift

;     TVSCL,abs(newim - ref_image)
      END

      bestmerit=max(merit,p)
      print
      print,xs,angle(p),xshft(p),yshft(p),bestmerit
      print
```

```
      ang=angle(p)

xs=512                                  ;image expansion scale
EXPAND,old_images(1),xs,xs,ref_image      ;registration reference image
ref_kernel=CONJ(FFT(ref_image,1))    ;Fourier correlation kernel
EXPAND,old_images(regnum),xs,xs,rhold     ;image to register
merit(*)=-1e30                          ;initialize merit array
dthnum=0

FOR dth=ang-0.2,ang+0.21,0.2 DO BEGIN           ;trial rotations
      dthnum=dthnum+1                         ;trial rotation count
      regim=ROT(rhold,360+dth,/INTERP)

      c=FFT(FFT(regim,1)*ref_kernel,-1)    ;Cross correlate in
                                        ;Fourier domain
      cmax=MAX(c,p)                           ;Find correlation maximum

      xshift=p MOD xs                         ;compute image shift
      IF xshift GT xs/2 THEN xshift=xshift-xs   ;check for 2's
complement
      yshift=p/xs
      IF yshift GT xs/2 THEN yshift=yshift-xs

      newim=ROT(regim,0,1,xs/2+xshift,xs/2+yshift)
      expand,newim,mx,my,scnew            ;reduce to original scale

      ss1=total((newim-ref_image)^2)            ;sum squared differences
      ss2=total(sbim*(scnew-old_images(1))^2)   ;edge-weighted sq. diff
                                       ;on original image scale
      merit(dthnum)=cmax
      angle(dthnum)=dth
      xshft(dthnum)=xshift
      yshft(dthnum)=yshift


      print,dth,cmax,ss1,ss2,xshift,yshift

;     TVSCL,abs(newim - ref_image)
      END

      bestmerit=max(merit,p)
      print
      print,xs,angle(p),xshft(p),yshft(p),bestmerit
      print
      ang=angle(p)

xs=1024                                 ;image expansion scale
EXPAND,old_images(1),xs,xs,ref_image      ;registration reference image
ref_kernel=CONJ(FFT(ref_image,1))    ;Fourier correlation kernel
EXPAND,old_images(regnum),xs,xs,rhold     ;image to register
merit(*)=-1e30                          ;initialize merit array
bestmerit=-1e30
dthnum=0

FOR dth=ang-0.1,ang+0.11,0.1 DO BEGIN           ;trial rotations
      dthnum=dthnum+1                         ;trial rotation count
      regim=ROT(rhold,360+dth,/INTERP)

      c=FFT(FFT(regim,1)*ref_kernel,-1)    ;Cross correlate in
                                       ;Fourier domain
      cmax=MAX(c,p)                           ;Find correlation maximum
```

```
      xshift=p MOD xs                        ;compute image shift
      IF xshift GT xs/2 THEN xshift=xshift-xs   ;check for 2's
complement
      yshift=p/xs
      IF yshift GT xs/2 THEN yshift=yshift-xs

      newim=ROT(regim,0,1,xs/2+xshift,xs/2+yshift)
      expand,newim,mx,my,scnew               ;reduce to original scale

      ss1=total((newim-ref_image)^2)             ;sum squared differences
      ss2=total(sbim*(scnew-old_images(1))^2)    ;edge-weighted sq. diff
                                    ;on original image scale
      merit(dthnum)=cmax
      angle(dthnum)=dth
      xshft(dthnum)=xshift
      yshft(dthnum)=yshift

      IF merit(dthnum) GT bestmerit THEN BEGIN
            bestimage=scnew
            bestmerit=merit(dthnum)
            END


      print,dth,cmax,ss1,ss2,xshift,yshift

;     TVSCL,abs(newim - ref_image)                '
      END

      bestmerit=max(merit,p)
      print
      print,xs,angle(p),xshft(p),yshft(p),bestmerit
      print
      ang=angle(p)

      new_images(regnum)=bestimage
      ss2=total((bestimage-old_images(1))^2)
      printf,3,regnum,ang,xshft(p),yshft(p),ss2

END
CLOSE,1,2,3
END
```

C.5 EPI IMAGE RECONSTRUCTION CODE

The "repi.pro" program reconstructs EPI images from FID files acquired with the EPIB pulse program as described in Appendix A. An alternative version, "repiangle.pro", contains additional post-processing code for removal of image distortions.

```
;repi.pro
;IDL image reconstruction program
;by Brian Wowk, Dec. 1995

;EPI image reconstruction

!ORDER=1

images=1

k=COMPLEXARR(32,64)             ;image k space
w=COMPLEXARR(32,64)             ;k space weight
f=COMPLEXARR(8192)              ;fid (256 + 4096 + padded zeros)

g=FLTARR(4096)                  ;read gradient shape
px=FLTARR(4096,4)          ;interpolated k space coords
py=FLTARR(4096,4)
pw=FLTARR(4096,4)          ;interpolation weights

fift =COMPLEXARR(8192)          ;FT of fid
lfift=COMPLEXARR(16384)         ;zero-filled expansion of fift
lfi  =FLTARR(8192)              ;sinc interpolated version of fi

incr=1.0/56
FOR i=0,4096-256,256 DO BEGIN ;set read gradient shape
      g(i:i+8)=0
      FOR j=8,64 DO g(i+j)= (j-8)*incr
      g(i+64:i+72)=56*incr
      FOR j=72,128 DO g(i+j)= 56*incr - (j-72)*incr
      g(i+128:i+136)=0
      FOR j=136,192 DO g(i+j)= -(j-136)*incr
      g(i+192:i+200)=-56*incr
      FOR j=200,255 DO g(i+j)= -56*incr + (j-200)*incr
END
g=g+0.000    ;read gradient dc offset adjustment

sx=-0.5                   ;starting points on the k space matrix
sy=-0.5
FOR i=0,4095 DO BEGIN     ;compute k space interpolation
sy=sy+g(i)
sx=sx+32.0/4096

fx=sx-FLOOR(sx)
fy=sy-FLOOR(sy)

px(i,0)=FLOOR(sx) & py(i,0)=CEIL(sy)  & pw(i,0)=(1-fx)*  fy
px(i,1)=CEIL(sx)  & py(i,1)=CEIL(sy)  & pw(i,1)=  fx  *  fy
px(i,2)=CEIL(sx)  & py(i,2)=FLOOR(sy) & pw(i,2)=  fx  *(1-fy)
px(i,3)=FLOOR(sx) & py(i,3)=FLOOR(sy) & pw(i,3)=(1-fx)*(1-fy)

END

FOR i=0,4095 DO BEGIN     ;eliminate out-of-bounds coords
```

```
FOR j=0,3 DO BEGIN

IF px(i,j) LT 0 OR px(i,j) GE 32 OR py(i,j) LT 0 OR py(i,j) GE 64 $
THEN BEGIN
      px(i,j)=0
      py(i,j)=0
      pw(i,j)=0
END
END
END

w(*,*)=1.0
FOR i=0,4095 DO BEGIN   ;compute k space weight matrix
FOR j=0,3 DO BEGIN
w(px(i,j),py(i,j))=w(px(i,j),py(i,j))+pw(i,j)
END
END

;window,0,xsize=256,ysize=256
;tvscl,congrid(w,256,256)

OPENR,1,'fid.16b'       ;open fid
a=ASSOC(1,INTARR(8704))

OPENW,2,'pdata/1/2dseq'         ;reconstructed images
b=ASSOC(2,fltarr(32,64))

baseline=complex(0,0)
FOR image=0,images-1 DO BEGIN ;compute digitizer baseline
an=a(image)
BYTEORDER,an                  ;swap byte order (Bruker -> SGI)
FOR i=50,99 DO f(i)=COMPLEX(an(i*2),an(i*2+1))
baseline=baseline+total(f(50:99))/50  ;completely dephased signal
END
baseline=baseline/images

FOR image=0,0 DO BEGIN        ;reconstruct images
print,image

an=a(image)
BYTEORDER,an                  ;swap byte order (Bruker -> SGI)

f(*)=0.0
f(INDGEN(4352))=COMPLEX(an(INDGEN(4352)*2),an(INDGEN(4352)*2+1))

f=f-baseline                  ;baseline correction

fr=FLOAT(f)             ;real part of fid
fi=IMAGINARY(f)               ;imaginary part of fid

                        ;correction for qseq ADC mode
fift=FFT(fi(*),1)       ;FT of a fi line
lfift(*)=0.0
lfift(0:4095)=fift(0:4095)
lfift(12288:16383)=fift(4096:8191)  ;zero-padded expansion
lfi=FFT(lfift,-1)       ;FT back to larger size
lfi=SHIFT(lfi,1)        ;shift to get sinc interp
fi(*)=lfi(INDGEN(8192)*2)*2   ;interp values back to fi

f=COMPLEX(fr,fi)
```

```
rst=253.35  ;fid readout start
slp=1.000   ;read gradient slope factor

FOR i=0,4095 DO BEGIN
FOR j=0,3 DO BEGIN
k(px(i,j),py(i,j))=k(px(i,j),py(i,j))+INTERPOLATE(f,rst+i)*pw(i,j)
END
END

k=k/w

r=ABS(FFT(k,1))          ;magnitude image
r=SHIFT(r,16,32)  ;shift to center

rf=r
FOR i=0,63 DO BEGIN
FOR j=0,31 DO BEGIN
rf(j,i)=INTERPOLATE(r,(j+i*0.25+1+32) MOD 32,i)
END
END

WINDOW,0,XSIZE=256,YSIZE=256  ;display image
EXPAND,rf,64,64,fx
TVSCL,CONGRID(fx,256,256)

WINDOW,1,XSIZE=256,YSIZE=256  ;display k space magnitude
TVSCL,CONGRID(abs(k),256,256)

WINDOW,2,XSIZE=256,YSIZE=256  ;display k space phase
TVSCL,CONGRID(atan(IMAGINARY(k),FLOAT(k)),256,256)

b(image)=rf
END

CLOSE,1,2

END
```

Appendix D

GLOSSARY

Blipped EPI

An *EPI* method in which the *phase encode* gradient is briefly "blipped" on and then off between *readout gradient* alternations, thereby sweeping the MR signal in a rectilinear path through *k-space*.

BOLD fMRI

Blood-Oxygen-Level-Dependent functional Magnetic Resonance Imaging (fMRI). A fMRI method that detects brain activity by detecting local changes in blood oxygenation.

Centric Phase Ordering

A *phase encoding* method that sweeps *k-space* from the center-outward, rather than from top to bottom.

Diffusion-Weighted Imaging

An MRI technique in which strong gradients are turned on and then reversed before imaging, creating image contrast that is related to diffusion of water in tissue.

EPI

Echo-Planar Imaging. An MR imaging method in which *gradients* are rapidly switched to acquire an entire image after one RF excitation.

Ernst Angle

The *RF* spin flip angle that maximizes MR signal for a given *TR*. The Ernst angle is given by $\cos\theta = \exp(-TR/T1)$.

FLASH

Fast-Low-Angle-SHot. A common MR imaging method in which a low-flip-angle *RF* pulse and *gradient echo* is used to collect each line of *k-space*, producing an image in five to ten seconds.

Gradient

A linear variation in magnetic field strength imposed as part of the MR imaging process.

Gradient Echo

An MR signal that appears after *gradients* are manipulated to rephase signals after an *RF* excitation. If the echo time is long, the received signal will experience $T2^*$ decay.

Gradient Moment

The "balance" of a *gradient waveform* given by $\int tG(t)dt$.

Gradient Moment Nulling

The design of *gradient waveforms* such that the *gradient moment* is zero. *Spins* flowing at constant velocity will not suffer phase shifts if *gradient moments* are null. This design technique is also called "gradient motion rephasing" or "flow compensation."

Gradient Waveform

The strength of a *gradient* as a function of time.

k-Space

The Fourier domain representation of MR images that *gradients* cause the MR signal to trace during imaging.

Magnetization Prepared FLASH

A *FLASH* imaging method in which some manipulation (such as *diffusion weighting* or *T2** weighting) is performed on *spins* before rapid *FLASH* imaging. Also called "turbo FLASH".

Magnetization Transfer Contrast (MTC)

Contrast resulting from chemical exchange and cross relaxation of immobile protons that are excited by off-resonance *RF* pulses. For example, protons in macromolecules will have a very short *T2* and very broad frequency sensitivity. Unlike water protons, these protons can be excited by off-resonance RF energy. If after time *<T1* the protons become incorporated into mobile water molecules by chemical exchange, they will participate in the MR imaging process, and produce image darkening related to the abundance of macromolecules. MTC effects occur

whenever off-resonance *RF* pulses are used (such as to excite slabs outside an imaging slice) during imaging of biological material.

Navigator Echo

An MR signal collected to determine signal phase prior to imposition of imaging *gradients*.

Perfusion Imaging

Imaging methods, such as Flow-sensitive Alternating Inversion Recovery (FAIR), that are designed to measure local blood perfusion (measured in milliliters per gram of tissue per second). Perfusion imaging is a quantitative alternative to *BOLD fMRI* for detecting brain function.

Phase Encode Gradient

By convention, the *gradient* that sweeps *k-space* at the slowest rate during MR imaging.

RARE

Rapid Acquisition with Relaxation Enhancement. A fast imaging method based on repeated 180° *RF* pulses to produce T2 contrast. Also called "fast spin echo" or FSE.

Readout Gradient

The *gradient* that sweeps *k-space* at the fastest rate during MR imaging. Also called the "frequency encode" gradient.

RF

Radiofrequency magnetic induction fields applied during MR experiments, typically in the form of a pulse, to tip *spin* magnetization away from alignment with the main magnetic field.

SAR

Specific Absorption Rate. The rate of *RF* energy deposition in tissue during MR imaging, typically expressed in Watts/kg.

Saturation

The loss of longitudinal magnetization during repeated RF pulses.

Spin Echo

An MR signal that appears after a 180° *RF* pulse is applied to rephase signals after an *RF* excitation. If the echo time (*TE*) is long, the received signal will experience *T2* decay.

Spins

Nuclei that are observed in an MR experiment. Most often refers to protons in the hydrogen atoms of water molecules.

Spoiler Gradient

A *gradient* applied with the intention of dephasing transverse magnetization, leaving only the longitudinal component.

T1

The time constant for recovery of longitudinal magnetization after an *RF* pulse. T1 relaxation (also called spin-lattice relaxation) is driven by dynamic magnetic field variations on the molecular scale produced by neighboring dipoles. Specifically, field variations near the resonant frequency drive T1 relaxation.

T2

The time constant for decay of transverse magnetization after an *RF* pulse. T2 relaxation (also called spin-spin relaxation) is driven by dephasing caused by dynamic magnetic field variations on the molecular scale. T2 relaxation occurs between *RF* excitation and formation of a *spin echo*.

T2*

The time constant for decay of transverse magnetization after an *RF* pulse due to dephasing caused by both dynamic magnetic field variation (T2 relaxation) plus static magnetic field variation. T2* relaxation occurs between *RF* excitation and formation of a *gradient echo*.

TR

Repetition time. The time interval between repeated *RF* pulses.

TE

Echo time. The time between *RF* excitation and production of a *spin echo* or *gradient echo*.